Politecnico di Torino

DIMEAS - DIPARTIMENTO DI INGEGNERIA MECCANICA E AEROSPAZIALE
Master of Science in Biomedical Engineering

Master's Degree Thesis

Remote control of an implantable nanofluidic device for drug delivery

Supervisors
Prof. Danilo Demarchi
Ph.D. Paolo Motto Ros
M.Sc. Antonia Silvestri

Candidate
Elena Marisa Morena
ID number: 265748

March 2021

Abstract

Chronic pathologies affect a large part of the adult population and often cause hospitalization, reduced quality of life, and even death. Therefore, treating these pathologies is a critical issue that is further complicated by problems related to traditional drug administration methods and patients adherence. The need to overcome these limits is leading to the development of innovative devices for controlled drug release; however, although research is making great strides, a fully implantable device, that allows for fine control of drug dosage after implantation, is still an unmet clinical need.

In this context, nanofluidic membranes are up-and-coming devices. They enable a controlled release without any mechanical component due to their nanometric channels, which allow a concentration-independent drug flow. Furthermore, by applying a voltage to the channel walls through electrodes and, thus, modifying their surface charge, it is possible to modulate the release when necessary. This thesis aims to design a printed circuit board (PCB) for the fine bipolar control of a silicon nanofluidic membrane; moreover, the monitoring of the patient's physiological state is made possible by including a temperature sensor. The final device is remotely controllable via Bluetooth Low Energy for temperature data exchange and voltage modulation, allowing the medician to become aware of an eventual unhealthy condition and decide if and how to release the drug accordingly. Since the final device is meant to be fully implantable, the designed system must take up as little space as possible and promote long battery life.

First, the components have been chosen based on their dimensions and manageability, and then simulations have been performed on LTspice to evaluate the designed system. After programming the microcontroller to drive the voltage and receive temperature data from the sensor, the Bluetooth communication has been set, thus enabling the final user to interact with the device through a dedicated interface. Then, the system's proper functioning has been experimentally verified, and, finally, through electrochemical tests, the device has been interfaced directly with the membrane, which responded positively. The designed system has proven to enable a fine control of the drug release, providing a promising strategy for tunable drug delivery.

Contents

List of Figures

List of Tables

Introduction

According to the World Health Organization (WHO) [1], in 2019 the chronic or non-communicable diseases made up seven of the world's top 10 causes of death and, altogether, accounted for 74 % of deaths globally. Chronic pathologies often lead to hospitalization, disability, and, in any case, reduce the quality of life [2]. Further, since they have a protracted course, they require continuous therapeutic management. Traditional administration methods have many limitations: they often require multiple doses and this can be a problem especially when the drug has poor bioavailability, moreover, they augment the risk of resistance and side effects, and, eventually, patient adherence is crucial [3]. In view of this, new implantable sustained-release platforms have been developed and are still widely researched. Drug delivery systems can be divided into two categories: passive and active devices. The passive ones have the advantage of being small-sized but, differently from the active devices, cannot provide the control of the release kinetics to the patient or the physician. Active systems generally consist of actuators, micro-reservoirs, various electronic components, batteries, and antennas for communication with the external environment. It is fundamental for an implantable active device to be as less invasive as possible, therefore, resorting to the microfabrication techniques, it is possible to obtain miniaturized complex devices. Electromechanical systems exploit features at the nanoscale and microscale; they have great potential as they can merge structural, mechanical, and electrical features in order to achieve better performances, thus leading to a dosing control after implantation aimed at a very personalized therapy [4]. Indeed, most common diseases such as diabetes, hypertension, neurodegenerative conditions and rheumatoid arthritis are determined by circadian biological cycles [5, 6], which means that it is very important to release the suitable quantity of drugs in the right site at the right time [7]. Another interesting aspect is that, some local characteristics of the tissue, such as pH, concentrations of proteins and enzymes and temperature, could be used as markers of a pathological state [8]. Consequently, many drug delivery stimuli-sensitive systems have been investigated. [9]

Advanced technologies enabling a personalized therapy could avoid the income of undesirable problems of resistance, tolerability, and side effects associated with the *one-size-fits-all* blanket treatments [10]. An effective system should entail zero-order release kinetics, tunable dose, wireless communication, a release stoppage when not needed and, last but not least, compact size and dimensions. Nanochannel membranes seem to be very promising systems, since they enable a constant rate of drug release and, by tailoring their size and surface chemistry it is possible to obtain the desired long-term sustain of therapeutics [11].

The nanochannel Delivery System (nDS) is a nanofluidic membrane developed by Grattoni et al. [12], which is able to sustained drug release. It is characterized by dense arrays of identical and parallel nanochannels in a design that promotes both high channel density and physical robustness. By accompanying the nDS membrane by electrodes it is possible to obtain a programmable dose modulation by applying an external low-intensity electric field. In fact, because of the nanometric dimensions, the analytes' flow exhibits a great dependency on the surface charge which can be modified throughout the application of a small potential. Therefore, the device has been equipped with a PCB (Printed Circuit Board), composed of a microcontroller, through which it is possible to produce the desired voltage to connect to the membrane electrodes, and radiofrequency oscillators, which allow the exchange of data with the external environment. The membrane can be dynamically controlled via Bluetooth low energy communication and, in this aspect, some studies have already been published, showing good performance and easily controllable dosing [13–15]. The device, in its present appearance, can only apply either 0, 1.5 or 3 V, thus, to reach a finer control, the need for a small-sized circuit able to apply different analog voltages with a higher resolution is evident. Moreover, the device lack of any sensor control of the local physiological state, that would allow to know from the outside the local state at that moment and consequently decide if a new release is necessary.

In this context, the present work is aimed at the development of a PCB that enables the control of the drug release via Bluetooth Low Energy through a small, low-power circuit, able to modify the voltage applied to the nanochannel membrane with a resolution of at least 250 mV. This voltage is meant to be both negative and positive in order to achieve a finer controlled release. This is made possible by the use of the Texas Instruments microcontroller CC2640R2F which is equipped with a 2.4-GHz RF transceiver compatible with Bluetooth Low Energy 5.1.
It is well known how some pathologies, such as inflammation or irritation, lead to an increase of local temperature, due to chemical processes and modified perfusion [16, 17]. By monitoring the temperature, it is possible to use this information to decide whether a modulation of the drug release rate is needed. Therefore, it has been decided to equip the device with a temperature sensor that communicates with the microcontroller, which then transmits the temperature data through BLE, in order to deliver the drug at the proper times, thus ensuring maximum effectiveness of the drug itself. First, the components have been chosen and it has been decided how to set up the system, then, through some simulations, the potential of the device has been proven. The microcontroller, has been, thus, programmed, in order to enable the generation of the analog signal and the control of the temperature sensor via BLE. Finally, the PCB has been designed by using a software package for printed circuit boards in view of its printing to allow for further testing.

Chapter 1

State of the art

1.1 Implantable drug delivery systems

The drugs are most commonly administrated orally, which method, although practical and not invasive, has many limitations. Indeed, many pharmaceuticals have a better effect when delivered to the bloodstream continuously instead of ingested intermittently [18]. Oral delivery generally provides a high level of the drug in the blood immediately, that right after starts disappearing at a rate depending on the drug and the patient. This rate is usually expressed in terms of *half life*, which is a pharmacokinetic parameter defined as the time required for the drug concentration to decrease to half its peak level (see Figure 1.1).

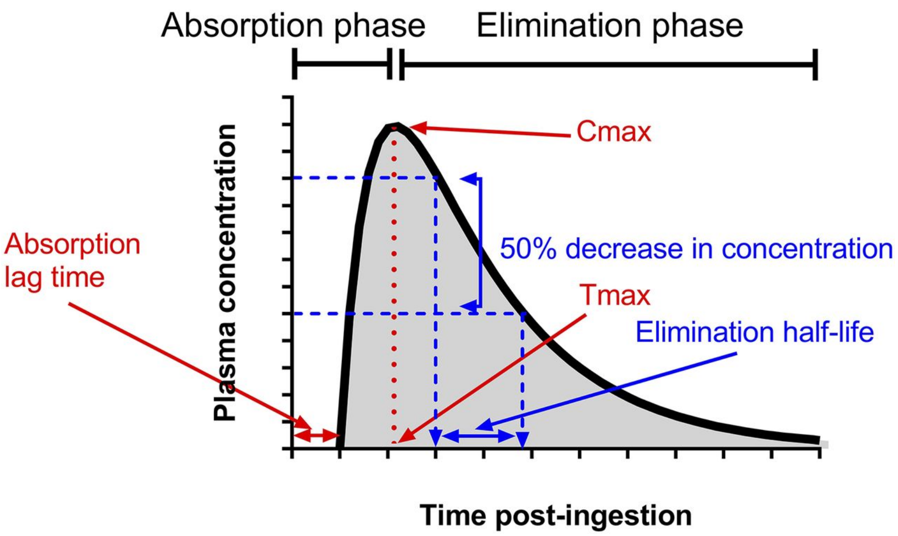

Figure 1.1: Plasma concentration of a drug as a function of time. After the ingestion, there is a pealk in which the concentration reach its maximum, then, it rapidly decrease based on it half-life. [19]

For an oral administration, the concentration trend is a peak-and-valley pattern, which means that first a concentration peak is reached, thus leading to a dramatic increase that for some drugs and individuals could even be toxic, then, with a rate depending on its half-life, the pharmaceutical falls under the minimum effective concentration. Moreover, since many drugs could be inactivated in the gastrointestinal tract, they can only be administrated intravenously and, if they also have a short half-life, frequent injections are required. Another crucial aspect is patient adherence, which is not negligible because forgetfulness and misunderstandings in the communication with medicians are extremely common. [20] Developing implantable drug delivery systems that enable effective delivery with lower drug concentration makes possible to overcome the pointed-out limits. Moreover, the side-effects and the problems related to patient compliance are minimized, and the first-pass metabolism is avoided with the consequent increase of drug bioavailability. As implantable systems, they require invasive surgery; however, it is widely counterbalanced by the advantages if it is needed only once. [21]

With the growth of the need for new administration methods, in recent years, have been developed several implantable drug delivery technologies, such as reservoir-based polymer systems, pumps (osmotic, peristaltic, or infusion), and electromechanical systems, which are able to maintain a sustained release for a duration of several months or, sometimes even a year [4]. Reservoir-based polymer systems, among the developed devices, are the ones that received the most FDA approval and have been longer on the market; they generally are small-sized, easy to insert and remove, and they are able of site-specific drug release [22]. Pumps can have different working mechanisms: the osmotic pumps are smaller, and they are suggested when a systemic or site-specific effect is required [23]; peristaltic and infusion pumps can be used, instead, to treat chronic diseases as they are equipped with more extensive drug reservoir and refill feature [24]. In general, they lack the possibility of dosing control after implantation, except for the peristaltic pumps, which are active devices that need a battery and enable zero-order release [25]. Their most significant limitation is their size, which would require invasive surgery. On their side, electromechanical systems exploit features at the nanoscale and microscale; they have great potential as they can merge fluidic and electronic components to achieve better performance and even an electronically controllable release, which would lead to very personalized therapy. Even though most of them are not yet FDA approved, this type of device shows great potential, as they are very versatile and small-sized systems that could allow a dosing control after implantation. [26].

1.2 Wireless communication for drug delivery systems

Some externally controllable devices, based on the employment of a tunable permeability membrane, have already been researched [27–29], but they usually require cumbersome external equipment along with an external stimulus (i.e. near-infrared light and electromagnetic fields) which should be active throughout the duration of the release. Some devices can be electrically controlled, thus permitting them to overcome these limitations by using low-energy radio-frequency (RF) communication. Radiofrequency waves have begun to be used in implantable systems in the last decades, in which, the knowledge on the interaction of electromagnetic waves and the human body got deeper [30, 31]. Although radio-frequency communication is an integral part of many current drug delivery devices, the medical requirements related to dosing are still an unmet need [32].

1.2.1 Bluetooth Low Energy (BLE)

Bluetooth Low Energy (BLE) is an emerging low-power wireless technology developed by the Bluetooth Special Interest Group (SIG) [33]. It operates in the same range as classic Bluetooth (2.4 GHz) but, differently from it, defines 40 radiofrequency channels with 2MHz channel spacing, some of which are used as advertising channels for device discovery and connection. In contrast, the others are aimed at the bidirectional communication between connected devices.

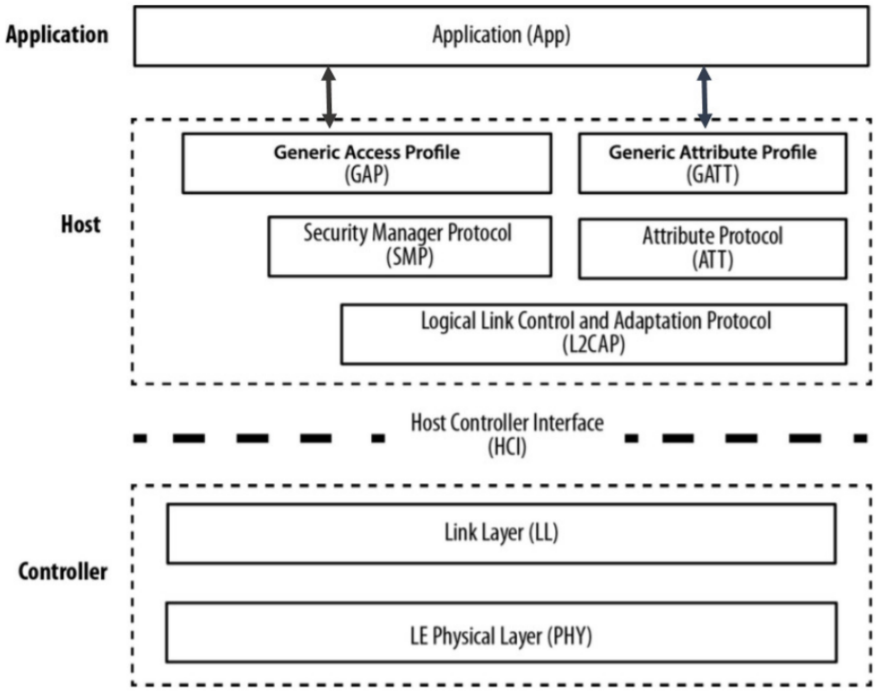

Figure 1.2: BLE protocol stack. It is possible to distinguish two main parts, the host and the controller, whereas the applications are built on top of the host.

Like in classic Bluetooth, the BLE protocol stack consists of two main parts: the Controller and the Host (as shown in Figure 1.2), which communicate with each other through a standardized interface provided by the HCI layer. The Generic Access Profile (GAP) controls the RF state of the device (standby, advertising, scanning, initiating, connected): when a device is in the advertising state, it transmits data without connecting; the central device, or rather, a BLE device which can initiate a connection, will respond to the advertiser (or peripheral device) request to connect. Then, they both enter the connected state as either master or slave. The Generic Attribute Profile (GATT) layer defines the communication between the two devices that connect: data is transferred and stored as characteristics which have some attributes as the value and the type of data storage, permissions, and handling identifiers. These characteristics are collected in Services, which, in turn, are collected in a Profile. Typically a smartphone sends a request to the GATT service to access the GATT Server characteristics followed by their discovery and, thus, access the preset operations.

BLE has already been implemented in different fields such as healthcare, wellness, and fitness [34, 35]. This technology is very attractive since it consumes extremely little energy, and by tuning its parameters, it is possible to meet application requirements in terms of energy consumption, latency, and throughput [36]. It has already been implemented in implantable sensors [37, 38] as it enables the connection with a device like a mobile phone or computer. Some research groups have also explored its application in drug delivery systems with promising results [14, 39].

1.3 Nanochannel membranes for drug delivery

Nanotechnologies are still at the beginning phase of their development. They rely on the exploitation of nanoscience methods to create and use materials, devices, and molecular-sized systems, thus leading to plenty of new opportunities. Indeed, the matter properties and behavior at the nanoscale are profoundly different from those at the macroscale [40]. In the last few decades, the researchers' focus has moved towards silicon-based chips for the medical field and, particularly, micro and nano-electromechanical system technologies (BioMEMS and BioNEMS) [26].

In this context, the implementation of new nanochannel membranes has been explored as filtering systems for charged analytes. When channels, which enable the flux of a charged solution, have minimal dimensions, their size gets comparable to diffusing analytes. This makes the wall-to-molecule interaction crucial in the molecular release that switches into a concentration-independent zero-order behavior [41]. The same would apply to drug molecules, which can be either positive or negative, thus enabling a continuous release of the drug and maximizing its efficiency. Indeed, the drug dose could be kept in the optimal therapeutic window, which is a great advantage compared to the traditional administration methods, which are more likely to produce side effects (see Figure 1.3).

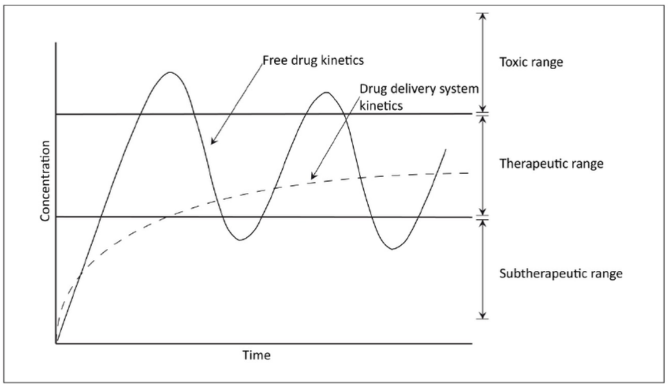

Figure 1.3: Difference in the concentration profile between conventional administration systems (solid line) and drug-delivery (dashed line) devices. A repeatedly-dosed free drug would get out of the therapeutic range, producing a toxic effect or being totally ineffective. A dug delivery device would allow a sustained release, causing the drug to remain effective for longer. [42]

These membranes are very versatile systems as, by tightly tailoring the number, the width, and the length of the nanochannels according to the size and molecular properties of the therapeutic agent considered, it is possible to change the release rate [43, 44]. Moreover, interfering with the surface charge through the application of a voltage it is possible to modify their selectivity. These membranes can then be assembled into a drug reservoir, which should be biocompatible, usually comprised of polyethyl-ether-ketone (PEEK) or titanium [40, 45]. For all these reasons, various research groups developed this nanochannel approach by using many different materials, including silicon, alumina, carbon, polydimethylsiloxane, and many more [4]. In recent years, the development of new precision silicon fabrication techniques [46, 47] enabled great control over the monodispersed nanochannel dimensions and surface roughness. This lead to an increase in silicon device proposals since their fabrication requires precision, accuracy, and reliability. A significant advantage of this structure is that it requires no pumping mechanisms or valves, as it relies on the diffusion between an inner reservoir and the outside so that they are not subject to fatigue stresses. Some nanoporous membranes have been proposed in drug delivery, for example, the titanium oxide NanoPortal Membrane [48] as well as NANOPOR technology [49], which both only enable zero-order passive release without the possibility of dosage control after implantation. Some anodic aluminum oxide (AAO) nanoporous membranes have been tested to evaluate the possibility of a dosing control through electrostatic gating [50], however, AAO seems to be not very suitable for this application as polydispersity limits the achievement of a fine control [51].

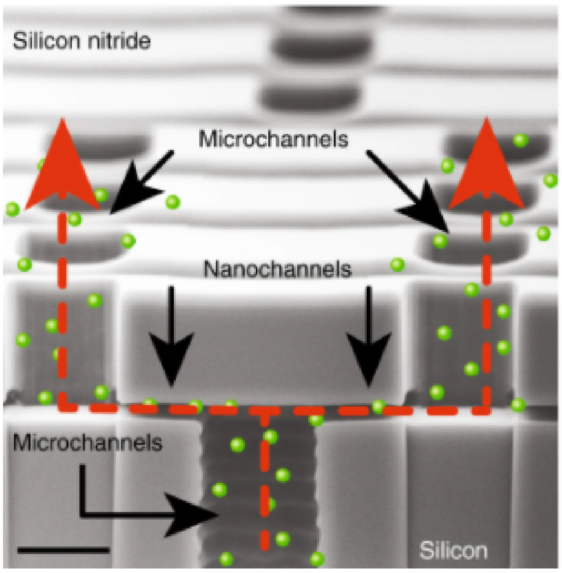

Figure 1.4: SEM cross-section of a nanochannel membrane. It shows graphically the path followed by a charged molecule flowing inside the nano and the microchannels of the structure. The presence of the nanochannel grants a sustained release.[11]

The membrane developed by Grattoni et al. [12] is characterized by dense arrays nanochannels uniform and parallel, built with sub-nanometer size tolerances, obtained using standard silicon manufacturing techniques and SOI (silicon on insulator) substrates. These nanochannels are placed horizontally, orthogonal to inlet and outlet microchannels running to either membrane surface (see Figure 1.4). This design promotes both high channel density and physical robustness [41].

The silicon carbide (SiC)-coating works as insulator for the electrode ensuring low leakage currents, thus entailing an energy loss reduction; moreover, SiC provides biocompatibility, and chemical inertness [52, 53]. Subsequent testing on the developed membrane have proved the possibility of gating control with successful results[13–15].

1.3.1 Zero-order release

The filtration capabilities of filters constituted by monodispersed arrays of nanochannels fabricated in silicon wafers have been demonstrated during the 1990s [54, 55]. As previously mentioned, the membrane exploits nanoscale phenomena to passively control the constant release of drugs, in particular, if the channel walls are charged, the oppositely charged ions accumulate at the surface to maintain local electroneutrality which makes up the electrical double layer (EDL) [56, 57]. The extension of the EDL, called Debye length, depends on the ionic strength and the surface charge. The Debye length (λ) is a significant parameter to understand how nanochannels can lead to a concentration-independent flux. Indeed, if it is much smaller than the nanochannels' height (h), the analyte will flow as in the bulk electrolyte solution, proportionally to the ionic strength. When $\frac{h}{\lambda} < 1$ or $\frac{h}{\lambda} \simeq 1$, instead, there is a plateau in conductance [58]. More specifically, if the ionic strength is lowered under a certain limit, the analyte flux gets constant and concentration-independent (see Figure 1.5). Through electrochemical impedance spectroscopy measurements, it is possible to evaluate EDL conductance [57].

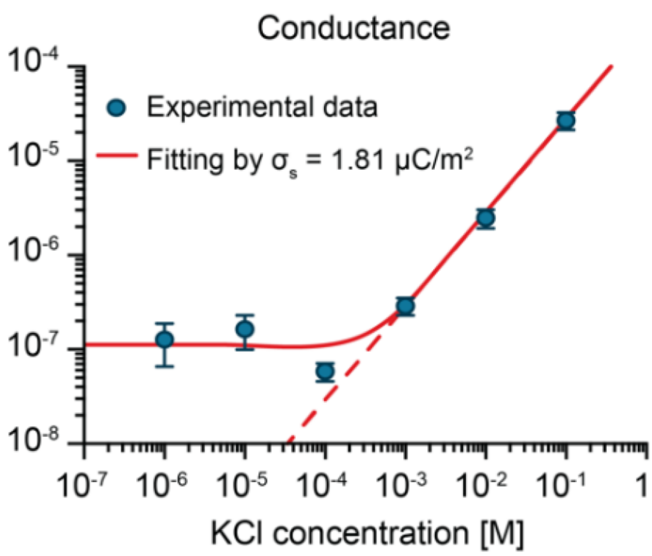

Figure 1.5: The graph shows the measurements of the transmembrane conductance made by Di Trani et al. [13] on their nanochannel membrane. It shows the influence of the ionic strength in the conductance of a nanochannel and compares it to a flow at the macroscale. At higher concentrations, the behavior at the nanoscale can be assimilated to the bulky one and increases linearly with the concentration. As the concentration gets lower, at the nanoscale, the dependence of the flux on it disappears [13]

1.3.2 Electronic control of analyte flow through nanochannels

As already mentioned, at the nanoscale, molecular diffusion exhibits unique behaviors. When the surface has its own characteristic charge, due to the exposition of some chemical groups depending on the material at issue, the charged species redistribute, so that the electrostatic neutrality is maintained. It can be easily derived that the surface charge has a significant effect on the overall concentration of charged molecules in the channel and, for fixed solution properties, it is the parameter that matters the most.[14]

Therefore, by controlling the surface charge with the application of a potential between the membrane electrode and the electrolyte solution, it is possible to modify the nanochannel charge-selectivity [58–60]. More specifically, considering, for instance, a negatively charged surface, when no voltage is applied, the flow of negative molecules depends on the interactions between the ions and the nanochannel walls, which determine a certain EDL width; with the application of a negative voltage an overpotential is produced, more counter-ions feel the charge attraction, thus increasing the interaction layer and minimizing the available space for ions flow. Therefore, the co-ions diffusion is significantly decreased or even completely impeded (see Figure 1.6).

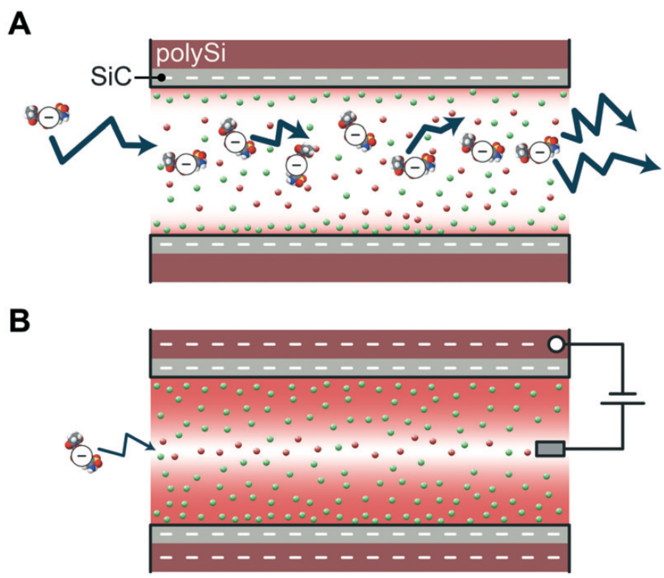

Figure 1.6: Analyte flow with and without the application of a small potential. In both figures, the surface, as well as the analytes that we want to control, are negatively charged. In A) the negative charge molecules can flow through the channel, in the center of the canal. In B) it is shown how, after the application of a potential, the negative charge of the surfaces increases, thus generating a bigger layer of counter-ions, which interrupts the flow of negative ions through the channel. [15]

Di Trani et al. [13] have deeply investigated the behavior of the SiC-covered nanochannel membrane by comparing it with SiO_2 which is commonly used as gate dielectric material. SiO_2, as well as SiC, exhibits negative-charged silanol groups on their surface at the physiological pH [61]. The study proved the SiC membrane to act as expected, moreover, as it has a much smaller amount of charges on its surface ($1.81\frac{\mu C}{m^2}$ [13]) with respect to Silicon di-oxide ($1 - 100\frac{mC}{m^2}$ [58]), it exhibited better performance in electrostatic gating control. The system has been tested with different types of electrodes and nanochannel dimensions, by controlling the diffusion of analytes such as methotrexate [13, 14] and DNA salt [15]. In 2019, the same research group demonstrated how, applying negative and positive small potentials, it was possible to interfere with the methotrexate release in vitro. [14] In particular, the results showed a decrease of the release rate for a -1.5V potential and an increase for +1.5V; moreover, it is also pointed out how, by applying a 0V potential, the release returned to a zero-order concentration driven diffusion. These tests were performed by using a custom device designed and developed to perform the electrical characterization of the nanomembranes, investigate the ionic conductivity as a function of concentration, and measure the transmembrane I-V characteristic [62]. It comprises two PVC bodies with a macro cuvette and a drug reservoir. The membrane holder is housed between the two bodies. In [14] different electrical DC potentials have been applied alternating active and passive phases.

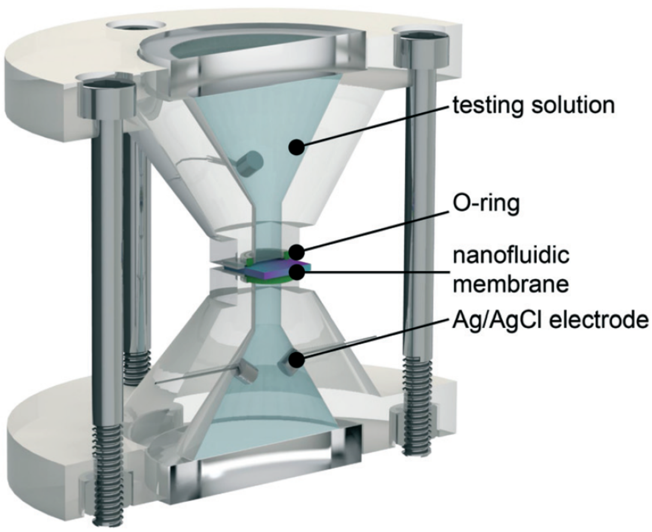

Figure 1.7: Custom device for nanochannel membranes testing. The nanofluidic membrane is locked between the two reservoirs containing the testing solution and the electrodes enable the application of an external potential. [15]

1.3.3 Electrical model

To a first approximation, the membrane can be modelized as a resistor and a capacitor in parallel. The capacitor models the electrical double layer (C_{EDL}), whereas the resistor is meant to consider the current that can flow across the interface upon application of a potential (R_{ct}). To make it more detailed, it is possible to add a further resistance (R_0), which would take into account the liquid's electrolyte resistance and the Warburg impedance, which represents all the slow diffusion processes.

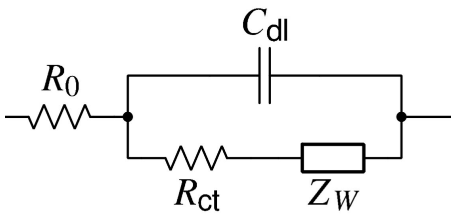

Figure 1.8: Electrical model of the nanofluidic membrane

Electrical Double Layer (EDL)

The electrical double layer (EDL) is generated because of the surface group dissociation of the solid in contact with a solvent, which produces surface charges. Because of the electrostatic attractions, the oppositely charged ions (counter-ions) naturally accumulate at the surface in order to maintain electroneutrality.

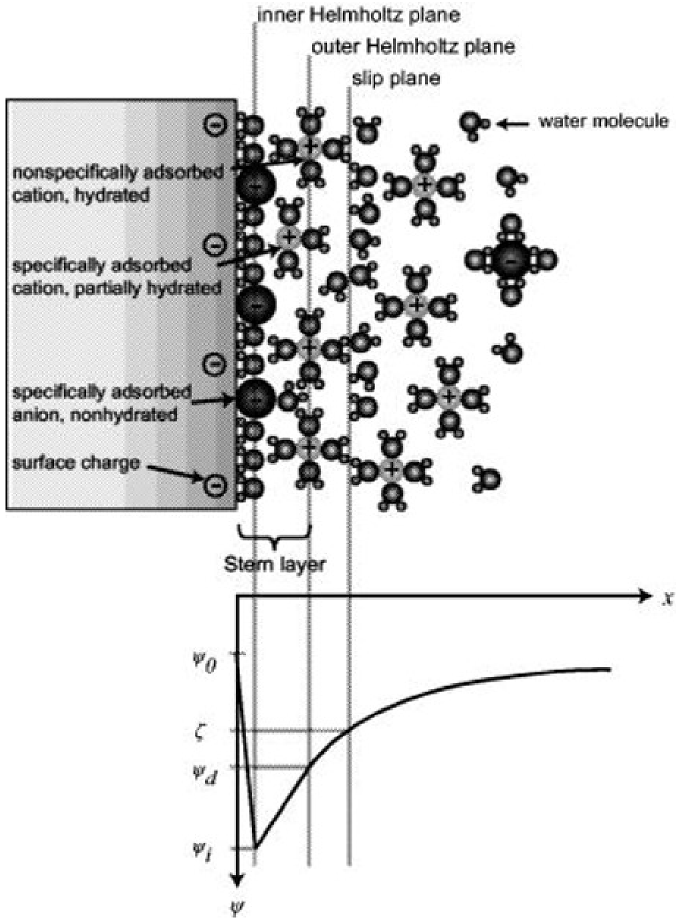

Figure 1.9: Here, the three-layer diagram based on the Grahame model is represented. The solid is supposed to have a negative surface potential (ψ_0) and in the graph, the behavior of the potential in function of the position is shown. At first, there is a linear increase, then, moving away from the surface, it decreases exponentially [63]

The EDL was firstly represented with the model of Helmholtz with a single capacitor, then, Gouy and Chapman considered a higher-extended layer of uniformly distributed charges. [64] Putting them together, Stern, introduced the Stern layer which is characterized by a greater drop of potential and a second diffuse layer further from the wall according to the Gouy-Chapman theory. The latest and the more relevant developed model is the Grahame triple-layer model [65], which identifies three main layers: the inner Helmoltz layer in which the ions are non-hydrated and adsorbed to the surface, the outer Helmholtz plane, which is made up of the adsorbed ions' centers in a non-specific manner, eventually, the outermost and third layer is the diffuse layer, which involves free moving hydratated ions (see Figure 1.9)

Overall, the EDL region can be modeled with a double layer capacitance (C_{EDL}), which is the results of a series of capacitors, where the Stern layer gives the main contribution.

Warburg impedance

To model the semi-infinite linear diffusion, or rather, the unrestricted diffusion in one dimension only bounded by a large planar electrode on one side, the most common circuit element is the Warburg impedance. Unlike the other components that make up the circuit model, the Warburg impedance does not have a simple equivalent circuit, but its effect can only be approximated.

As it is an impedance, it is characterised by magnitude and phase and can be defined as a complex number :

$$Z_w = \frac{A_w}{\sqrt{j\omega}} \tag{1.1}$$

Where A_w is the Warburg coefficient, $\omega = 2\pi f$ and j is the imaginary unit.

Its magnitude takes higher values for lower frequencies and its phase is constant and is equal to 45°, which means that it has a slope of $10\frac{dB}{dec}$. It would be well represented by a linear uniformly distributed RC structure, characterized by a total resistance and a total capacitance [66]. Many different equivalent circuits for this type of structure have been developed in order to allow efficient computer simulation [67]. Usually, these equivalent circuits are formed by a few lumped elements, such as resistances, capacitances, and inductances. The most immediate representation of the distributed structure is the ladder circuit, which involves only equal capacitors and resistors (as shown in figure 1.10); however, to obtain acceptable results, a huge number of RC sections are needed, making this structure unsuitable for practical purposes.

To overcome this limit, many different equivalent circuits have been studied both with equal and un-equal elements [66] and, among them, the approach developed by Valsa et al. [68] revealed to be very handy as it permits to reach good performance with a low number of branches. The structure implemented is the one represented in Figure 1.11.

The paper presents a fast, easy method that with a few steps, starting from the frequency band, the phase ϕ (that is equal to 45° for the Warburg impedance) and the amplitude of the oscillations admitted around ϕ, returns the values of all the resistances and capacitors composing the network.

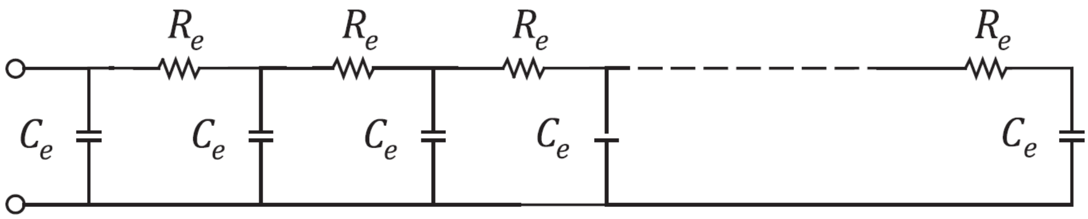

Figure 1.10: Ladder circuit used to model electrochemical impedance. The total resistance and total capacitance of the structure are split into a large number of equal resistances and capacitances. However, this type of structure needs a huge number of branches to obtain an adequate model [66].

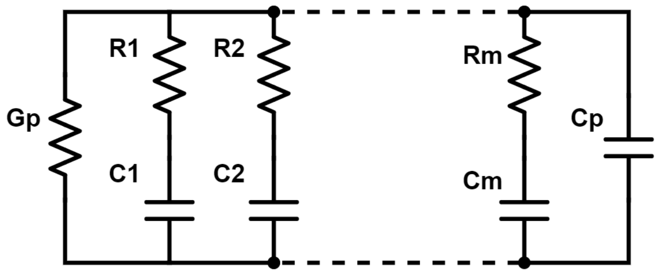

Figure 1.11: Lumped circuit for the modelization of the Warburg impedance developed by Valsa et al. [68] It is made of as many branches as required from the working frequency range and the phase oscillations. The structure can achieve good performance with a limited number of sections

1.4 Digital to analog conversion

Digital to analog conversion is frequently required in a digital system that needs to be interfaced with an analog signal or circuit. It is widely used in electronics for various applications such as industrial automation, data acquisition, digital audio and video and many more. They are supposed to associate uniquely binary information to a voltage, a charge, or either a current, which are included in a precise range. A binary number constituted of N-bit is given as an input to the converter and, to each value, will correspond a proportional analog output. Since an N-bit word represents one of 2^N possible states, an N-bit DAC can have only 2^N possible analog outputs.

1.4.1 Figures of merit

A DAC (Digital-to-analogue converter) is characterized by some specification which allows the users to choose the right converter circuit for the application of interest. The following are some of the principal characteristics and performance parameters that usually need to be considered when characterizing a DAC.

- **Resolution** : defined as the smallest change in voltage obtainable as output of the converter, it is strictly related to the number of bits (N) and the full scale output range (V_{FS}).

$$Resolution = \frac{V_{FS}}{2^N - 1} \tag{1.2}$$

- **Full scale range** : it is the difference between the maximum and the minimum analog output values that the DAC may provide. They are supposed to match with codes 0 and 2^N.
- **LSB** : the least significant bit (LSB) is defined as the smallest output that can be unabiguously distinguished over the entire range of the converter.
- **Monotonicity** : a DAC is monotonic when its analog output increases for an increase in digital input with an error smaller than $\pm(\frac{1}{2})LSB$.
- **Static Performance**
  - **Differential nonlinearity (DNL)** : the DNL specifies the deviation of the actual step size from the ideal width and is computed as the difference between two successive analog outputs. It is a meaningful parameter that should be considered also to ensure DAC monotonicity because it could be compromised when the DNL is greater than 1 LSB. [69]

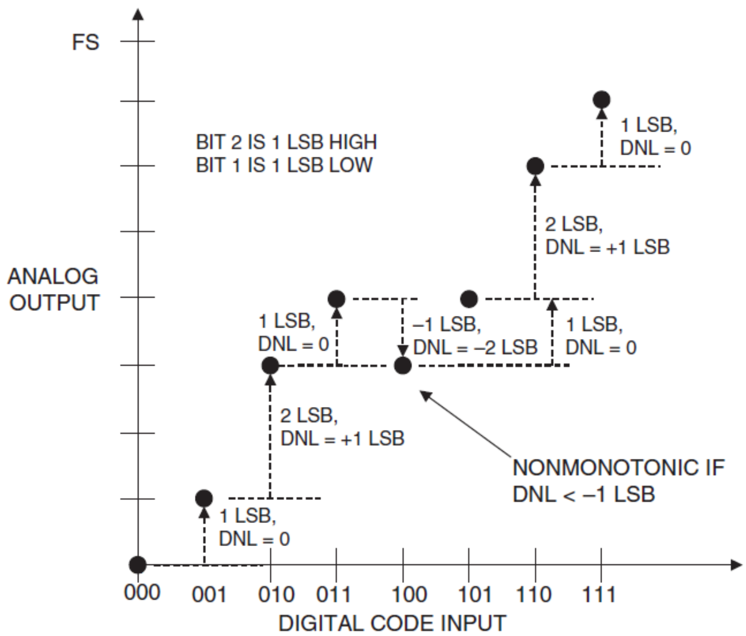

Figure 1.12: The graph shows what DNL is and how it affects the monotonicity and linearity of the DAC. Indeed, we would expect to see a linear behavior with a proportional relationship between the code input and the analog output. The DNL gives an indication of how much each point deviates from the linear behavior. [69]

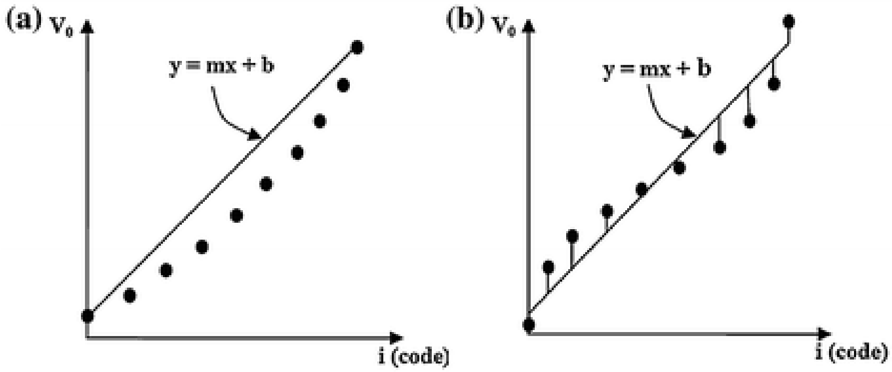

Figure 1.13: To evaluate gain and offset, a line interpolating the practical data has to be drawn. This can be made in two different ways: a) Endpoint method: data are interpolated connecting the extreme values; b) Best Fit method: data are interpolated to minimize the mean squared error from line to sample [70]

- **Gain and offset error** : These two parameters can be evaluated in different ways based on which DAC transfer curve is used as reference (see Figure 1.13). Once the transfer line of the DAC at issue is defined, the offset and gain can be defined as the values by which the output are, respectively, multiplied and added in the deviation from the ideal curve. The gain error can be expressed as a percentage (Equation 1.3), whereas the offset error both in Volts or LSBs.

$$GainError = \left(\frac{G_{actual}}{G_{ideal}} - 1\right) \cdot 100\% \tag{1.3}$$

- **Frequency domain performance**

  - **Spourius-free dynamic range(SFDR)** : ratio of the output signal amplitude to the highest spurious component of the frequency spectrum. It indicates of how much the usable dynamic range is, before spurious noise interferes. This definition is not unique as it can whether include the harmonics or not [71].

$$SFDR_{dB} = 20 \cdot \log_{10} \frac{\text{Amplitude of Fundamental (RMS)}}{\text{Amplitude of Largest Spurious (RMS)}} \tag{1.4}$$

  - **Signal-to-noise ratio (SNR)** : ratio between the power of the signal and the total noise produced by the circuit in the entire Nyquist range. The signal-to-noise and distortion ratio (SNDR) is similar to the SNR but it also accounts for the distortion terms.

$$SNR_{dB} = 20 \cdot \log_{10} \frac{\text{Amplitude of Fundamental (RMS)}}{\text{Amplitude of Noise (RMS)}} \tag{1.5}$$

  - **Total harmonic distorsion (THD)** : The harmonic distortion characterizes the ratio of the sum of the harmonics to the fundamental signal and represents the difference between an ideal sine wave expected and its reconstruction.

$$THD_{dB} = 20 \cdot \log_{10} \frac{\text{Amplitude of Hamonics + Noise (RMS)}}{\text{Amplitude of Fundamental(RMS)}} \quad (1.6)$$

– **Equivalent number of bits (ENOB)** : the ENOB gives an indication of how well the DAC approaches to an ideal DAC. In other words, it defines how many bits an ideal DAC would require to obtain the measured SINAD. Most of the references define ENOB through the SINAD [69], by using the formula 1.7, which can be used with a sinusoidal signal. 1.76 is related to the quantization error of an ideal DAC, whereas 6.08 is necessary to convert decibels to bits (as SINAD is expressed in dB, while ENOB should express a value in bits).

$$ENOB = \frac{SINAD - 1.76}{6.02} \quad (1.7)$$

However, if it is not intended to directly relate ENOB to the SINAD, another way to calculate it may be the one showed in Equation 1.8 [72], in which N is the number of bits of the DAC.

$$ENOB = N - log_2 \frac{\text{rms noise}}{\text{ideal rms quantization noise}} \quad (1.8)$$

For different application, such as PWM as a DAC, other expressions have been evaluated [73].

1.4.2 DAC circuits

Over the years, many different types of DAC architectures have been proposed, including successive approximation, pipelined, and delta-sigma architectures [74]. When designing a circuit, it is very important to find a good balance between resolution, power consumption and operation speed, in such a way that it matches the final application.

The simplest possible structure for a DAC is the string resistor ladder, which consists of $2^{N_{bit}}$ equal resistors in series that work as voltage dividers and as many switches. Different outputs can be obtained by closing just one of the switches at a time. However, the number of components increase along with the resolution, thus making it an impracticable solution for many applications. One of the most common structure is the R-2R resistor ladder network, which involves a cascaded structure of resistor values R and 2R as shown in Figure 1.14. Each arm is switched between V$_{REF}$ and ground, V$_{out}$ is taken from the output of the network and, depending on switches configuration, it can assume a value comprised between 0V and $V_{REF} - \frac{V_{REF}}{2^{N_{bit}}}$. Although this second option requires less components with respect to the first one (only $2N_{bit}$, instead of $2^{N_{bit}}$), this solution still includes a great number of pieces as the resolution increases.

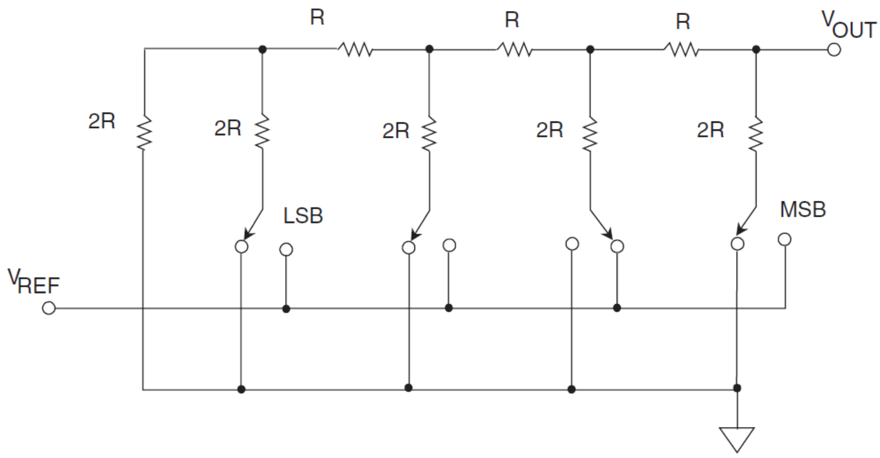

Figure 1.14: R-2R resistor ladder [69]

PCB design requires the use of tiny components. Many integrated circuits, based on the CMOS technology, can reach very small sizes, even footprint areas smaller than $0.5mm^2$ [75–77] but they are not commercially available yet. In commerce, instead, it is possible to find SMD (surface mount device) DAC with serial input (i.e. communication I^2C or SPI interface) that can reach dimensions of 4 or 5 mm^2, as it can be noticed on the websites of the main electronic components producers [78, 79]. Nevertheless, it has to be considered that when a converter is not buffered, its output impedance would be too high thus leading to great V_{out} errors for any load. In this case an additional external operational amplifier is required.

As DAC are widely used in audio application, new circuits have been developed in order to grant always better performance. An example are the class D amplifiers, which revealed to have significant advantages in many applications since, with respect to other solutions, are low power and produce less heat, and permit to save circuit board space and cost [80]. However, one of their major drawback is the need for an external LC filter, which increases the solution's cost and board space required, besides the possible introduction of distortions due to filter components nonlinearities. [81] Recently, filterless operation of class-D have been deeply investigated [82–84]. In filterless architectures, a modulation scheme allows to avoid the use of a cumbersome filter, thus connecting the amplifier directly to the load, which provides filtering. However, this can only be applied when the load is inductive at the switching frequency, otherwise, the device would be unstable [85]. Indeed, even in audio applications, it works only with a highly inductive voice coil and it is not implemented when it drives a tweeter or piezoelectric speaker.

PWM-based DAC

Pulse Width Modulation (PWM) consists of changing the duty cycle of a fixed frequency square wave that is given as an input to an analog low-pass filter, through which, the high-frequency components can be removed (see Figure 1.15) As it is a robust, simple and low-cost solution, it is widely used in different applications, such as power conversion, motor control, and field transmitters [73]. However, it is quite difficult to achieve high resolution in a wide bandwidth, so that, when higher accuracy is needed, a stand-alone DAC is preferred.

When a microcontroller is included in the project, the PWM signal can be generated without adding any other component and the low-pass filter is only required on the board. Even considering a second order active filter that includes an operational amplifier (OP-AMP), this circuit could likely lead to the minimal sized solution. Indeed, OP-AMPs are commercially available in very small sizes with a surface areas even smaller than $1mm^2$. Moreover, as mentioned before, some integrated DAC would require an OP-AMP as well; therefore, this solution is potentially advantageous.

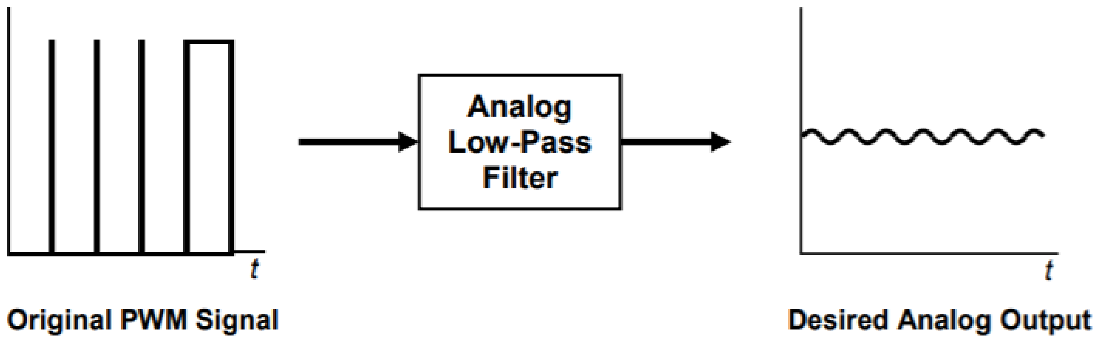

Figure 1.15: Schematic rapresentation of the working principle of a PWM DAC[86]

The PWM DAC performances, however, are strictly related to the low pass filter, so that its choice and sizing are crucial to obtain a good performance device. An ideal low pass filter would allow to completely reject higher frequencies, however, this cannot be obtained with actual parts and undesired frequency components will be only attenuated by a factor that decreases with the increasing of the frequency. The main limits of this application are the finite resolution which depends on the frequency of the signal generated, and the peak-to-peak ripple produced by unfiltered harmonics. A solution for this is to increase the stop-band roll-off, which means that higher-order filters may be useful.

Usually, active filters are more performing rather than passive filters [87]. Although they require active components so that the design is more complex, they avoid the impedance loading issue as they isolate the load resistance and the rest of the circuit. [88] Since an OP-AMP (Operational Amplifier) is used, it is very important for it to have a very high gain-bandwidth product as it represents the upper frequency that the OP-AMP can handle and it should be at least 5 or 10 times greater than the highest expected input frequency.

Chapter 2

Hardware Design

The present work aims at the development of a printed circuit board for the regulation of the voltage to apply to a nanochannel membrane for drug delivery to enable dosage control. The research group of the Houston Methodist Hospital Research Institute and Politecnico di Torino developed an implantable drug delivery system based on a silicon nanochannel membrane [12], named nDS2. This device embeds a Bluetooth Low Energy wireless microcontroller that allows modifying the drug release rate after implantation and has successfully been tested both in vitro and in vivo in non-human primate exhibiting good performances [14, 15] . In the validated version, the microcontroller in use is the CC2541 by Texas instruments [89], and the battery is a commercially available discoidal CR2016 (VARTA) which supplies a 3V potential. Later, it has been decided to replace the microcontroller with the CC2640R2F by Texas Instruments and to change the board shape that was initially circular to a more elongated version, however, the rest remained unchanged and is explained in the paper by Di Trani et al. [14]. Beyond the microcontroller, the PCB is composed of two external oscillators and a voltage regulator that enables the modulation of the potential applied to the membrane, which can assume only values equal to 0 V, $\pm 1.5V$ and 3 V. Anyhow, this device has room to improve since it has low resolution and lacks any sensing system to monitor the patient's health state. The idea is to substitute the current voltage modulation system with a small low-power circuit that allows a finer dosage control. Moreover, it has been decided to equip the device with a temperature sensor, which should have minimal sizes and a resolution high enough to perceive relatively small variations.

2.1 Bluetooth Low Energy Microcontroller

The CC2640R2F [90] device is a microcontroller that enables Bluetooth low energy applications. It belongs to the "SimpleLink™ ultra-low power" CC26xx family of 2.4GHz RF devices. This family of microcontrollers by Texas Instruments is considered one of the most efficient in terms of energy saving, thus providing a good battery lifetime of an eventual device. The CC2640R2F microcontroller contains a 32-bit processor that runs at 48 MHz, with 128 kB Flash and 275 kB ROM. There are two RC oscillators on-chip (32 kHz and 48 MHz) and two external crystals connected across 4 different input and output pins of the microcontroller, which oscillates at 24 MHz and 32.768 kHz [91]. Even though it has less Flash memory than CC2541 of the previous version, it has many more features and peripherals and, most of all, is available in a smaller package. Moreover, it has embedded a battery monitor that can be automatically enabled at boot and monitors the VDDS supply voltage and the temperature. It has many peripherals, as 12-bit ADC, I^2C interface, and Sensor controller, and it is available on the market in different sizes. The microcontroller mounted on the PCB at issue, has an area of $16mm^2$ and 32 pins (VQFN package).

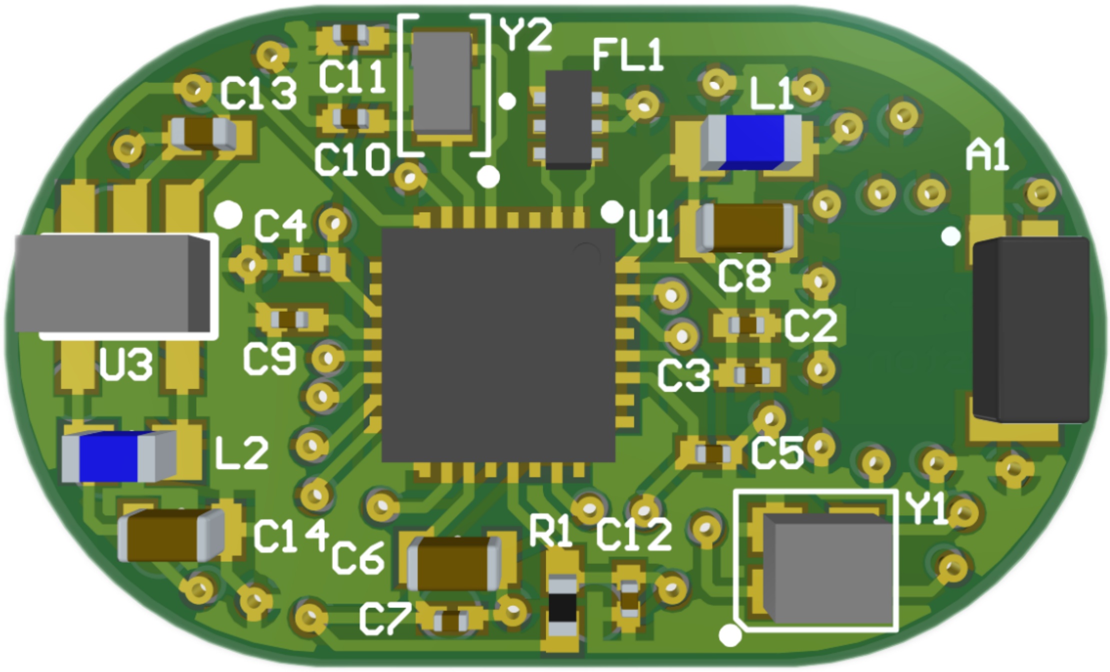

Figure 2.1: Current PCB configuration. U1 is the microcontroller;U3 is the voltage regulator, Y1 and Y2 are the two oscillators and FL1 and A1 compose the RF signal path.

The CC2640R2F microcontroller has three power rails: VDDS (PIN27), VDDR (PIN28), and DCOUPL (PIN12). VDDS is the main power source, it is supplied externally, at 3V in this application, and requires a decoupling circuit which is composed of 4 capacitors (C_4, C_5, C_6 and C_7 in Figure 2.1). The other rails require conditioning circuits as well, involving capacitors and inductors, whose values and connection directions are explained in the microcontroller's datasheet.

The two oscillators (Y1 and Y2 in Figure 2.1) are connected to the dedicated PINs (shown in Figure 2.2) following the layout indications. The 24 MHz oscillator is needed as clock for the RF blocks, whereas, in power-down mode, it is turned off and the other 32-kHz crystal oscillator is used.

A1 in Figure 2.1 is the antenna. On the microcontroller's datasheet it is said that a 50 Ω antenna is required. On the board it is placed a W3008 ceramic chip antenna along with a balun, which is the FL1 in Figure 2.1 made for this family of microcontrollers to convert between a balanced signal and an unbalanced signal.

Joint Test Action Group (JTAG) port is an IEEE standard used to test interconnections of the PCB and obtain manufacturing information on the components.

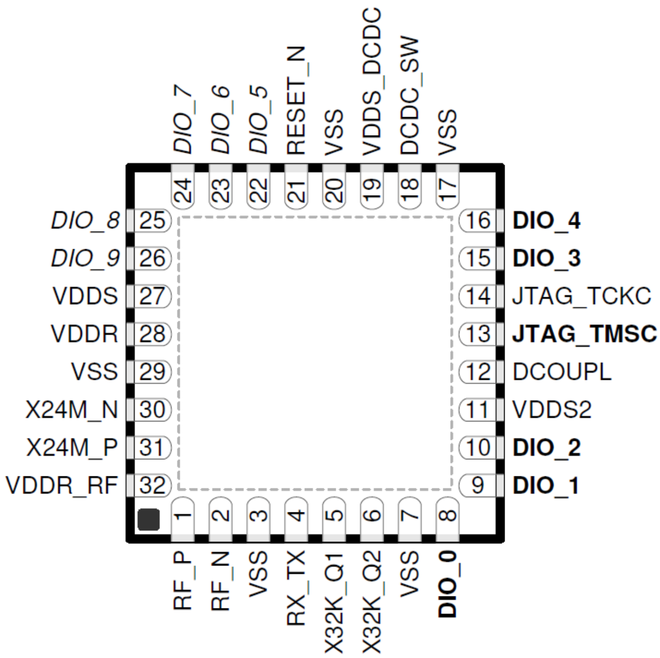

Figure 2.2: 32-pin VQFN package of the microcontroller CC2640R2F.

This solution includes some dedicated PINs which can block the normal functioning of the other PINs and start the debug mode. These four PINs, accessible from a connector reserved for testing, are the following:

- TCK (Test Clock) : clock PIN used for loading test mode and test data to synchronize the serial transmission.
- TMS (Test Mode Select) : the signal flowing through this PIN suspends the normal functioning of the integrated circuit and reports it to recognize the test working mode.
- TDI (Test Data In) : input pin for data.
- TDO (Test Data Out) : pin for reading the output signal data.

The RESET circuit is, eventually, connected to the RST PIN and includes a pull-up resistor and a by-pass capacitor. The output is then connected to a PAD that can be reached from the outside thus allowing the manual RESET.

2.2 Nanofluidic membrane voltage-based control

The circuit for the voltage modulation to apply to the nanochannel membrane, implemented on the current board, made use of a step-down DC-DC converter by Texas Instruments [92]. Its input was a general-purpose input-output (GPIO) pin of the microcontroller (P1), and its output was connected to one of the two electrodes included in the membrane walls, enabling the modification of the surface charge and, thus, drug modulation. The other electrode, instead, was directly connected to another GPIO (P2) which was set ON or OFF depending on whether it was required a 3V or a 0V output. The output of P1 and P2 could be programmed based on the voltage needed according to Table 2.1.

P1 (1.5 V)	P1 (1.5 V)	Applied potential
OFF	OFF	0 V
ON	OFF	-1.5 V
OFF	ON	3 V
ON	ON	1.5 V

Table 2.1: Table with the applicable voltage from the validated device.

However, as at its current state, the system can provide only 0, ±1.5, and 3 V, it is needed a way to introduce the possibility of switching potential with a major resolution. This objective could be reached by using a digital to analog converter, and, as both positive and negative voltages can lead to a modulation of the release, by introducing a full-bridge circuit terminals could be swapped, changing potential polarity when needed.

In its entirety, the circuit should require the minimum space possible on the PCB; otherwise, it would be impossible to let all the components in since the oscillators and the antenna occupy a significant region of the board. The current PCB has an area of 20mm x 12mm and contains 22 components, 4 of which are used to produce the potential with the voltage regulator system and, therefore, are the ones to be replaced.

2.2.1 Control architecture

Stand-alone DAC

First, it has been looked for a commercially available small-size DAC integrated circuit, and the two most relevant devices found are the ones in Table 2.3.

	Manufacturer	Area	Interface	$I_{DD, MAX}$
DAC5311	Texas Instruments	2 mm × 1.25 mm	Three-wire serial interface	150 μA
MCP4706	Microchip Technology	2 mm × 2 mm	I^2C	400 μA

Figure 2.3: Table of the most relevant commercially available integrated DAC.

Each solution requires two by-pass capacitors as suggested on their datasheets; moreover, whenever the I^2C interface is implemented, two more pull-up resistors have to be considered. Passive components can be minimal thanks to the surface mount technology, which is able to produce them with an area of $0.08mm^2$. However, it is not easy to find a PCB assembly factory that mounts this type of components. Considering this aspect, the smallest possible size components are 0201 SMD ($0.6mm \times 0.3mm$), whose area is about 0.18 mm^2. The smallest DAC in Table 2.3 requires 2 more passive components, thus occupying about $2.86mm^2$ of the available surface. Another important factor that should be taken into account is that a solution of this type would require 2 or 3 driving pins from the microcontroller, which could be complex to handle as the CC2640R2F device has only 10 GPIO and a connection line from one side of the board to the other may be unwieldy.

PWM-based DAC

Pulse width modulation (PWM) is a method which, through the use of a digital signal, tuning the ON and OFF intervals of the period, is able to modulate the average value of the output voltage: the higher the duty cycle percentage, the higher the total power supplied to the load.

By generating a PWM signal from a PIN of the microcontroller and passing it through a low-pass filter, which filters out all the undesired high frequencies, it is possible to obtain an output continuous analog voltage. In this case, the size occupied on the board depends only on the low-pass filter, which means that the choice of the type of filter and its components is crucial, thus limiting the feasible configurations. Aiming at the design of a second order low-pass filter, the two existing topologies have been considered:

- **Multiple feedback (MFB) filter**, mainly used when a high quality factor (Q) and high gain are needed
- **Sallen-Key filter**, one of the most common configuration for PWM applications.

The multiple feedback filter has an inverting configuration and places heavy constraints on the active element [93]. The Sallen-Key filter, on its part, requires two resistors, two capacitors, and a voltage follower and shows the least dependence of filter performance on the OP-AMP characteristics [94]. Moreover, it could be designed so that the two resistors are equal without the need to be particularly tightly matched so that component tolerance is not that important. The main drawback of the Sallen-Key filter lies in the direct path from the input network to the OP-AMP output, which implies that, for large frequencies, the output voltage from the OP-AMP is still very low, but the capacitor path creates an output signal at the finite output resistance of the OP-AMP. However, considering the listed aspects altogether, the Sallen-Key filter has been decided to be the right solution as it is effortless to implement, grants good performance, and is commonly used for this type of application.

Active filters require an OP-AMP (operational amplifier), which, in this case, should be carefully chosen to be small and low power. The smallest possible dimensions of the OP-AMPs available on the market are around $1mm^2$, and they always require a by-pass capacitor. A Sallen-Key circuit includes 4 passive components (two capacitors and two resistors) that, assuming to use 0201 SMD components, would occupy $0.72mm^2$.
Overall, this solution needs at least $2mm^2$ but only one pin of the microcontroller to be driven.

2.2.2 Circuit design

Considering the area occupied by both solutions, their power consumption, and the organization of connections and space management on the board, it has been decided to implement the solution based on the PWM signal. The idea is to generate the square wave from a microcontroller's pin; more specifically, PIN8 has been chosen since it is the one used previously to generate the voltage regulator's input signal. This choice has been made in view of keeping parallelism with the previous circuit, thus facilitating the pre-existing PCB modification. PIN8 corresponds to the microcontroller's DIO_0, which can be used to generate the PWM signal since the device CC2640R2F permits mapping all digital peripheral functions freely to any I/O pins.

Generation of the PWM signal

The microcontroller CC2640R2F includes four general-purpose timer modules, each of which can be configured to operate as a single 32-bit timer, dual 16-bit timers, or a PWM module. However, such a high resolution is not necessary for this application; indeed, the modulation is also limited from the membrane channel's size that, in this case, would not respond to such sharp voltage steps. Therefore, an 8-bit resolution is entirely sufficient, allowing for 256 different applicable duty cycles (0%, 0.39%, 0.78%, ...), which entail voltage steps of 11.77 mV.

The PWM signal generated should have the highest possible frequency in order to make the filter design simpler. The microcontroller has an on-chip oscillator at 48 MHz, which means that the minimum obtainable period is equal to 21 ns. After few calculations shown in Equation 2.1, the resulted working frequency is 187.5 kHz and the working period is $T = \frac{1}{187.5kHz} \simeq 5.3\mu s$.

$$\begin{aligned} &f = 48MHz \\ &T_{OSC} \simeq 21ns \\ &f_{MIN} = \frac{1}{(2^{16}) \cdot T_{OSC}} \simeq 732Hz \\ &f_{8bit} = \frac{1}{(2^{8}) \cdot T_{OSC}} \simeq 187.5Hz \end{aligned} \tag{2.1}$$

Low-pass filter design

The Sallen-Key filter includes an active component and 4 passive components. The OP-AMP should be carefully chosen in order to grant satisfactory performance while passive components determine the filter's cut-off frequency. Different design methods are possible [88]; however, as a unity gain is needed and the overshoot can be avoided, the most straightforward procedure assumes $R_1 = R_2$ and $C_1 = C_2$.

An OP-AMP that fits well this application should be able to work at 3V, require the smallest possible surface area, and grant minimal power consumption. Moreover, a rail-to-rail OP-AMP is preferred, which means that it is able to work very close to the extremes of the operating range.

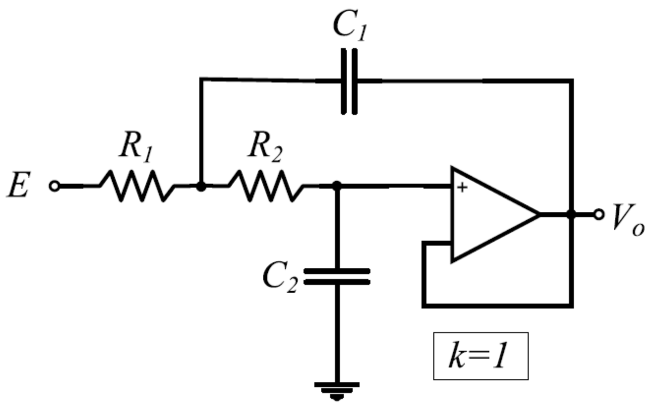

Figure 2.4: Sallen-key Filter

In Table 2.5 are listed some selected OP-AMP from different manufacturers that respect all these requirements.

	Manufacturer	Area	Power consumption	GBW
OPA330	Texas Instruments	0.80 mm × 1.2 mm	35 µA @ 3 V	350 kHz
TLV9061	Texas Instruments	0.80 mm × 0.80 mm	800 µA @ 3 V	10 MHz
TLV9051	Texas Instruments	0.80 mm × 0.80 mm	475 µA @ 3 V	5 MHz
TLV9001	Texas Instruments	0.80 mm × 0.80 mm	85 µA @ 3 V	1 MHz
AD8605	Analog Devices	0.90 mm × 1.29 mm	1500 µA @ 3 V	10 MHz
AD8505	Analog Devices	0.90 mm × 1.39 mm	25.5 µA @ 5 V	95 kHz
ADA4505-1	Analog Devices	0.90 mm × 1.39 mm	15 µA @ 3 V	50 kHz
MAX44290	Maxim Integrated	0.84 mm × 1.24 mm	1200 µA @ 3.3 V	15 MHz
MAX44265	Maxim Integrated	0.97 mm × 1.37 mm	5 µA @ 5.5 V	200 kHz
TSV630	STM	1.20 mm × 1.30 mm	66 µA @ 3.3 V	880 kHz
ISL28194	Renesas	1.60mm × 1.60 mm	0.500 µA @ 3 V	8 kHz

Figure 2.5: Table of the most relevant commercially available integrated OPAMP

The TLV9001 by Texas Instruments is the smallest sized solution; however, it is not the most performant concerning power consumption. On the contrary, the MAX44265 by Maxim has a greater surface area and a low GBW but also low power consumption.

All these solutions could work finely; at any rate, it has been looked for the best compromise among size, power consumption, and gain-bandwidth product by choosing the OPA330 by Texas Instruments (whose schematic is shown in figure 2.6. It is available in the smallest size with a DSBGA5 package, which requires a relatively small area, and, at the same time, allows to have much smaller power

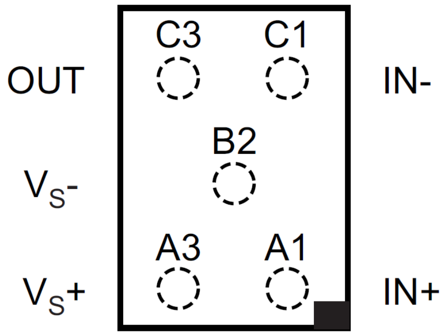

Figure 2.6: OPA330. DSBGA pin description.

consumption for a higher GBW with respect to other possible choices.

Some aspects should be considered to size a Sallen-Key filter: the circuit's gain, the quality factor, and the cut-off frequency. Moreover, in order to keep the size of the filter as small as possible, the passive components should be chosen of the 0201 SMD type, which does not provide all the possible capacitance values. The great majority of the SMD capacitors are ceramic and, choosing the class 1 type, lower electrical losses and higher accuracy and stability in voltage and temperature can be granted.

$$\omega_0 = \sqrt{\frac{1}{R_1 R_2 C_1 C_2}} \qquad\qquad Q = \frac{\sqrt{\frac{1}{R_1 R_2 C_1 C_2}}}{\frac{1}{R_1 C_1} + \frac{1}{R_2 C_1} + \frac{1-k}{R_2 C_2}} \tag{2.2}$$

Where $\omega_0 = 2\pi f_{cutoff}$, k is the gain and Q is the quality factor, which quantifies the overshoot of the Bode diagram at the cut-off frequency. By using a unity gain, assuming a simple design with $R_1 = R_2$ and $C_1 = C_2$, the equations in 2.2, become:

$$\omega_0 = \frac{1}{R \cdot C} \qquad\qquad Q = 0.5 \tag{2.3}$$

Having $Q = 0.5$ means that the magnitude of the Bode diagram is halved at the cut-off frequency. In other terms, since we expect to find a $0dB$ attenuation before the cut-off frequency, at that point, the magnitude should be $-6dB$.

Considering all the commercially available capacitors and resistors, different sizing options have been evaluated as a function of frequency, as shown in Figure 2.7. Resistors are easier to find with different sizes, so the possibilities are restricted from the capacitors' choice. As the resistor value increases, the cut-off frequency decreases by the same magnitude. Lower values would lead to greater current consumption and higher transmission of signals at high frequencies as shown in Figure 2.8; whereas, for high resistors values, the amount of current available to the circuit would increase the settling time employed to charge and discharge the capacitors. Even though in our application, the settling time is not a critical parameter, it is better to have a capacitance not lower than 100pF, as it would be too susceptible to parasitic capacitance; moreover, the thermal noise due to the resistors would grow with the square root of its value (Equation 2.4).

Fc = 100 Hz				
C	Package size	R (kΩ)	FC,max	FC,min
220 pF	0.6x0.3 mm^2	7500	98	95
330 pF	0.6x0.3 mm^2	4700	105	101
470 pF	0.6x0.3 mm^2	3300	105	101
560 pF	0.6x0.3 mm^2	2700	107	103
1000 pF	0.6x0.3 mm^2	2400	100	96

(a)

Fc = 1 kHz				
C	Package size	R (kΩ)	FC,max	FC,min
220 pF	0.6x0.3 mm^2	750	984	946
330 pF	0.6x0.3 mm^2	470	1047	1006
470 pF	0.6x0.3 mm^2	330	1047	1006
560 pF	0.6x0.3 mm^2	270	1074	1032
1000 pF	0.6x0.3 mm^2	160	1015	975

(b)

Fc = 10 kHz				
C	Package size	R (kΩ)	FC,max	FC,min
220 pF	0.6x0.3 mm^2	75	9842	9456
330 pF	0.6x0.3 mm^2	47	10470	10059
470 pF	0.6x0.3 mm^2	33	10470	10059
560 pF	0.6x0.3 mm^2	27	10740	10319
1000 pF	0.6x0.3 mm^2	24	9950	9560

(c)

Figure 2.7: Tables with the different possible resistors and capacitors sizing for different cut-off frequencies of the low-pass filter.

$$v_n = \sqrt{4k_BTR\Delta f} \tag{2.4}$$

Where v_n is the voltage due to thermal noise of the resistor, k_B is the Boltzmann's constant, T is the working temperature, R is the resistor's value, and Δf is the frequency bandwidth. The cut-off frequency should be at least a couple of orders of magnitude lower than the working frequency. Paying attention to fit the gain-bandwidth product of the OPA330, 100 Hz may be more appropriate since 3 order of magnitudes lower. Considering all these aspects pointed out, the configuration chosen is:

$$R = R_1 = R_2 = 3.3M\Omega \qquad C = C_1 = C_2 = 470pF \tag{2.5}$$

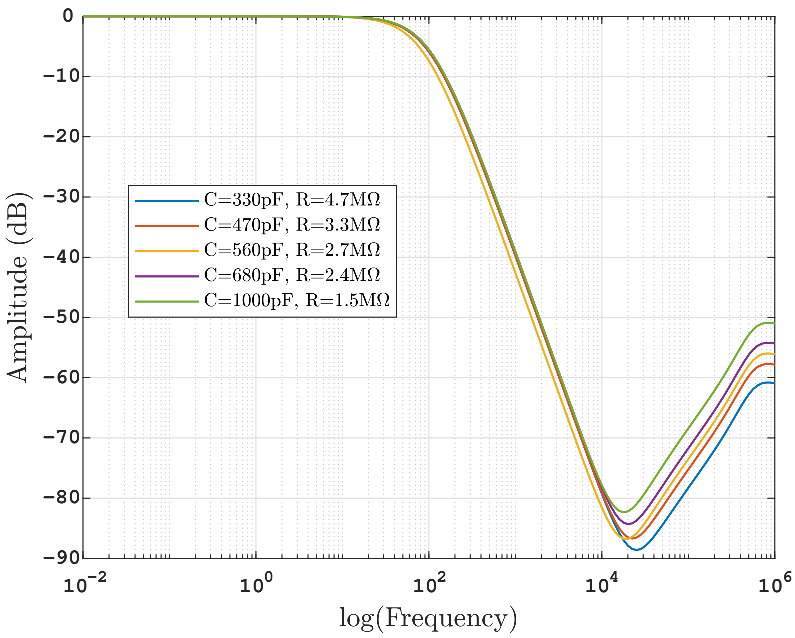

Figure 2.8: Dependency of the frequency response of the filter on the choice of components. The higher the resistors, the greater the increase in amplitude at higher frequencies. This is due to the direct connection between the input network and the output of the OPAMP.

2.2.3 Full-bridge circuit

Aiming at the design of a circuit that is able to produce as output both positive and negative voltages, the swapping of terminals could be a viable path. A full-bridge (or H-bridge), shown in Figure 2.9, is a circuit that, given an input voltage, enables the control of output voltage polarity by varying the conduction instants of the switches. This solution, borrowed from robotics and motor control, could work finely in this application as it is simple and effective.

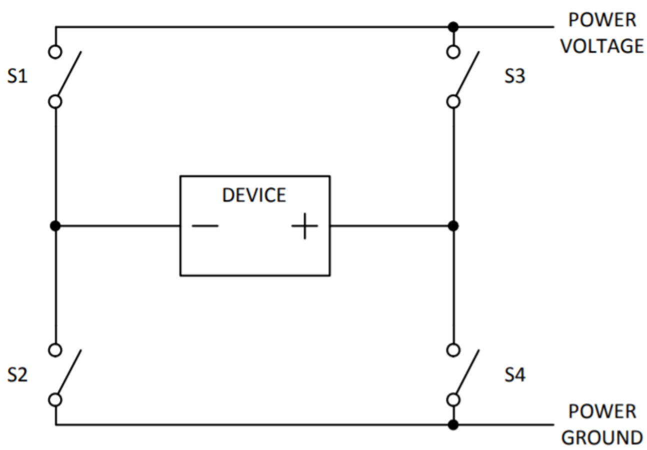

Figure 2.9: Full-bridge scheme

This circuit could be implemented using 4 different MOSFET switches, but each should be driven from a microcontroller's pin, which is unwieldy and not practical. Considering the low powers involved, an easier and handier solution could be the use of an integrated circuit, given that several can be found on the market.

	Manufacturer	Size	Power consumption	BW
ADG854	Analog Devices	1.3 × 1.6 mm	0.05 µA @ 3 V	100 MHz
DG2735	Vishay	1.4 × 1.8 mm	1 µA @ 3 V	120 MHz
FSA2268	ON Semiconductor	1.4 × 1.8 mm	0.5 µA @ 3 V	50 MHz
FSA2269	ON Semiconductor	1.2 × 1.6 mm	0.5 µA @ 3 V	50 MHz
NX3L2267GU	NXP	1.4 × 1.8 mm	0.2 µA @ 3 V	60 MHz
TMUX154	Texas Instruments	1.4 × 1.8 mm	1 µA @ 4.3 V	900 MHz
TMUX1136	Texas Instruments	2.5 × 1 mm	1 µA @ 5 V	220 MHz
TS3A24159	Texas Instruments	1.36 × 1.85 mm	1 µA @ 3 V	23 MHz
TS522366	Texas Instruments	1.2 × 1.6 mm	12 µA @ 3 V	32 MHz

Figure 2.10: Table of the most relevant commercially available integrated SPDT analog switches.

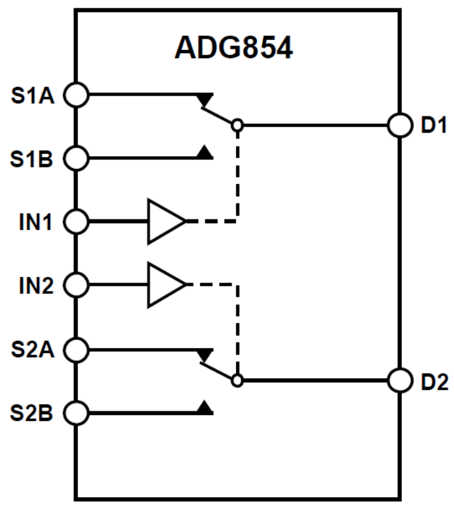

Figure 2.11: Functional block diagram of the ADG854 analog switch. D1 and D2 are connected to the electrodes, IN1 and IN2 are driven from the microcontroller, and all the S pins are connected to either ground or the output of the PWM DAC.

The same criteria as those used in choosing the other components' should be followed, including the small surface area, the low-power requirements, and the commercial

availability. An analog switch with a configuration 2 x SPDT (single pole double throw) could fit this application well. Indeed, it requires only 2 microcontroller pins, and it consumes a minimal amount of power, as can be noticed in Table 2.10 that lists the most suitable devices.
FSA2269 by ON Semiconductor is the smallest sized solution, however, as it has a very complex package, the ADG854 is preferred, which is still tiny and low power and has a good bandwidth. The integrated circuit needs to be driven by two microcontroller pins. Two GPIO pins (pin 25 and 26) have been chosen based on their position on the PCB board since any of them could work for this application.

2.3 Temperature sensor

A temperature sensor would enable the continuous monitoring of the area of implantation. Indeed, some pathologies, such as inflammation or irritation, lead to a local temperature increase; therefore, the inclusion of the sensor could provide an additional tool to the medician to decide how to modulate the drug release.

Exploiting the BLE features, when the sensor measures a precise temperature, it could send the data through the connection to the microcontroller, which, once received them, can communicate with another device, thus enabling the therapist or the patient himself to be aware of the current temperature level.

The desired temperature sensor should be available on the market and low power; it should save space on the board and, at the same time, it should be easy to manage in terms of the connection with the microcontroller. The great majority of board mount temperature sensors use a 2-wire interface, which means that two microcontroller pins are required to drive them.

The TMP117 by Texas Instruments [95] occupies a minimal surface area ($1.53mm \times 1.00mm$) and has good accuracy, also granting low power consumption (see Table 2.2). Smaller components may be found [96], but with a much worse accuracy and higher power dissipation. Moreover, the TMP117 has many features

Local sensor accuracy	$\pm 0{,}1°C$
Operating temperature range	$-55°C$ to $150°C$
Supply Voltage	1.8 V - 5.5 V
Interface type	I^2C
Temperature resolution	16 bits
Shutdown current @ 25°C	0.5 μA

Table 2.2: Characteristics of the temperature sensor TMP117 by Texas Instruments.

that could be useful, such as the Alert mode, which enables to trigger an interrupt any time the temperature goes out from a specific range or a conversion is completed, and the one-shot working mode, which permits saving power by starting a temperature data conversion only when is needed. For the alert mode implementation, it is necessary to connect the alert pin to a GPIO of the microcontroller. Therefore three connection lines are needed, each of which requires a resistor of $5k\Omega$, beside the device's by-pass capacitor that should be placed between the power line and ground. All these passive components have been chosen of the SMD 0201 type to save space, and the capacitors will be ceramic of class 2, which are commonly used for by-pass applications. The microcontroller pins chosen to manage the I^2C interface are PIN9 and PIN10 (DIO_1 and DIO_2), whereas the alert PIN is connected to a GPIO (PIN24 or DIO_7) programmed as input. ADD0 sets the address of the sensor and is usually connected to ground.

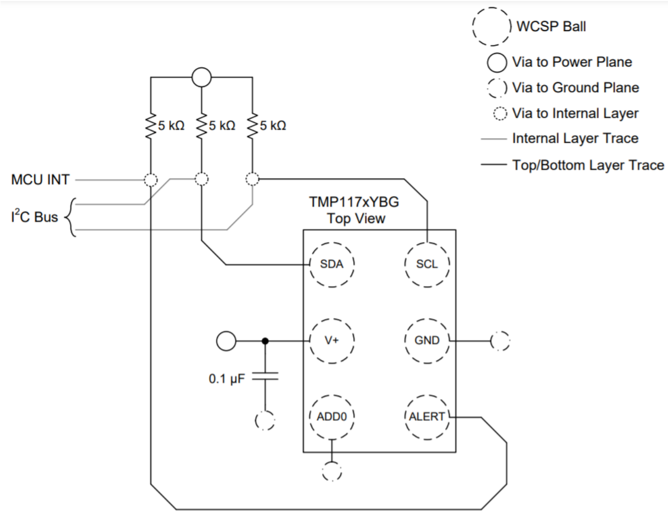

Figure 2.12: Suggested layout for the sensor TMP117.

2.4 PCB design

The printed circuit board needs to be updated to introduce the designed modification. For this purpose, the tool Altium Designer, which consists of a software package used for PCB and electronic design, has been used. It allows managing both the schematic and the 3D PCB design giving the user the possibility to either import pre-existing models for the selected components or create it custom, starting from the physical components' known characteristics. The project can then be used by the PCB assembler to print the board as desired, as long as all the rules have been respected. In fact, each house has its own rules that allow obtaining a good result by using the equipment it has available, placing some limits to the design. Altium Designer is equipped with a design rule check tool, through which it is possible to evaluate whether the rules have been followed or not.

Each component added to the circuit is characterized by a schematic symbol and a footprint needed for the board's 2D reconstruction. Moreover, although not fundamental, a 3D body is useful because it also allows the final 3D result evaluation. When the PCB is designed, its dimensions and shape need to be defined, then the number of layers and consequently the position and the connections among the components.

2.4.1 Schematic

The schematic circuit represents each component as a block, and each PIN is named based on its function. The resistors and capacitors models have been taken directly from the manufacturer's website as well as the active components. From PIN24, as previously mentioned, the PWM signal is generated, and then it is given as input to the low pass Sallen-Key filter including the OPA330 and then to the analog switch. The temperature sensor's layout follows the guidelines written on the datasheet, and it is driven from IOID_4 and IOID_5, which are used respectively as SCL and SDA lines for the I^{2}C interface. The other subcircuits are set up for the oscillators management and the decoupling of the supply voltage.

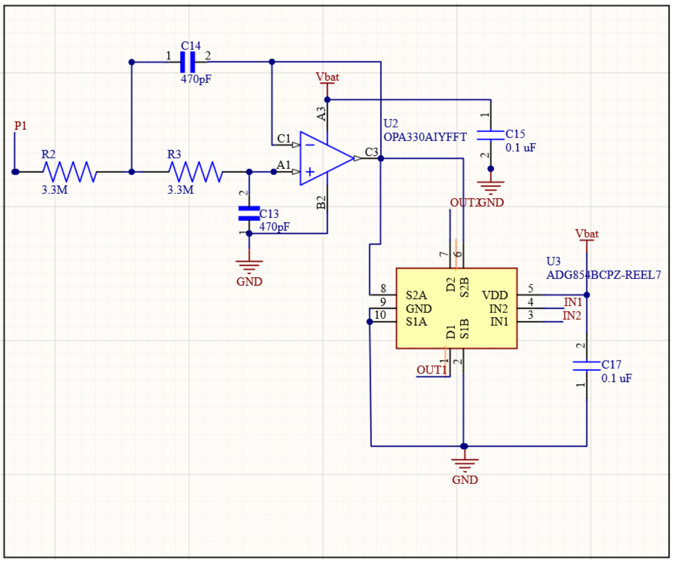

Figure 2.13: Schematic of the circuit for the voltage regulation.

In Figure 2.13 is shown the final circuit for the voltage regulation. P1 corresponds to PIN8 of the microcontroller from which the digital signal with different duty cycles is generated; C_{13}, C_{14}, R_2 and R_3 are the passive components of the low-pass Sallen-Key filter, whereas the other two capacitors (C_{15} and C_{17} are the by-pass capacitors for the OP-AMP and the analog switch respectively. The microcontroller controls the switches through PIN25 and PIN26 and, on the circuit, they are labeled with the names IN1 and IN2. The two outputs of the analog switch are OUT1 and OUT2 and are directly connected to 2 PADs reachable from the outside and connected to the membrane's electrodes. The OPA330 by Texas Instruments is, as explained above, the active component chosen for this application. More specifically, as can be noticed by the name written on the schematic, it is the OPA330AIYFFT, which is the version with the smallest dimensions with its DSBGA-5 package $(1 \times 1.293 mm^2)$.

The temperature sensor is controlled by the microcontroller through PIN9 and PIN10, labeled respectively as SDA and SCL to be associated with their role with ease. In the schematic in Figure 2.14 there are three connections to the microcontroller, which are connected to the supply voltage through a pull-up resistor.

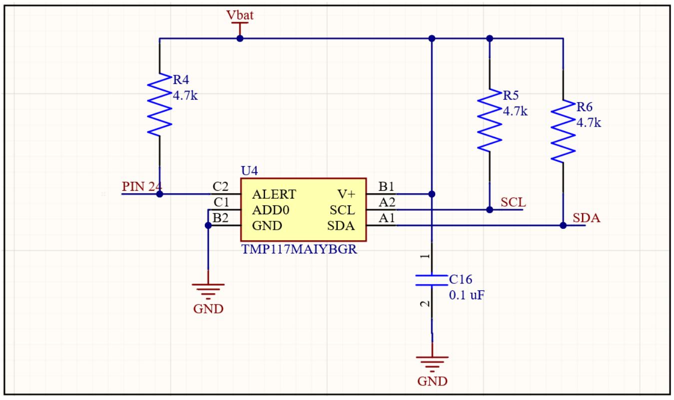

Figure 2.14: Schematic for the temperature sensor.

C_{16} is the by-pass capacitor, whereas ADD0, the address PIN, determines the sensor's address and allows up to four devices to be addressed on a single bus. The temperature sensor TMP117 by Texas Instruments is available in different packages. Since the smallest possible sizes are required, the minimal package has been chosen, which is the DSBGA-6 ($1.53 \times 1mm^2$).

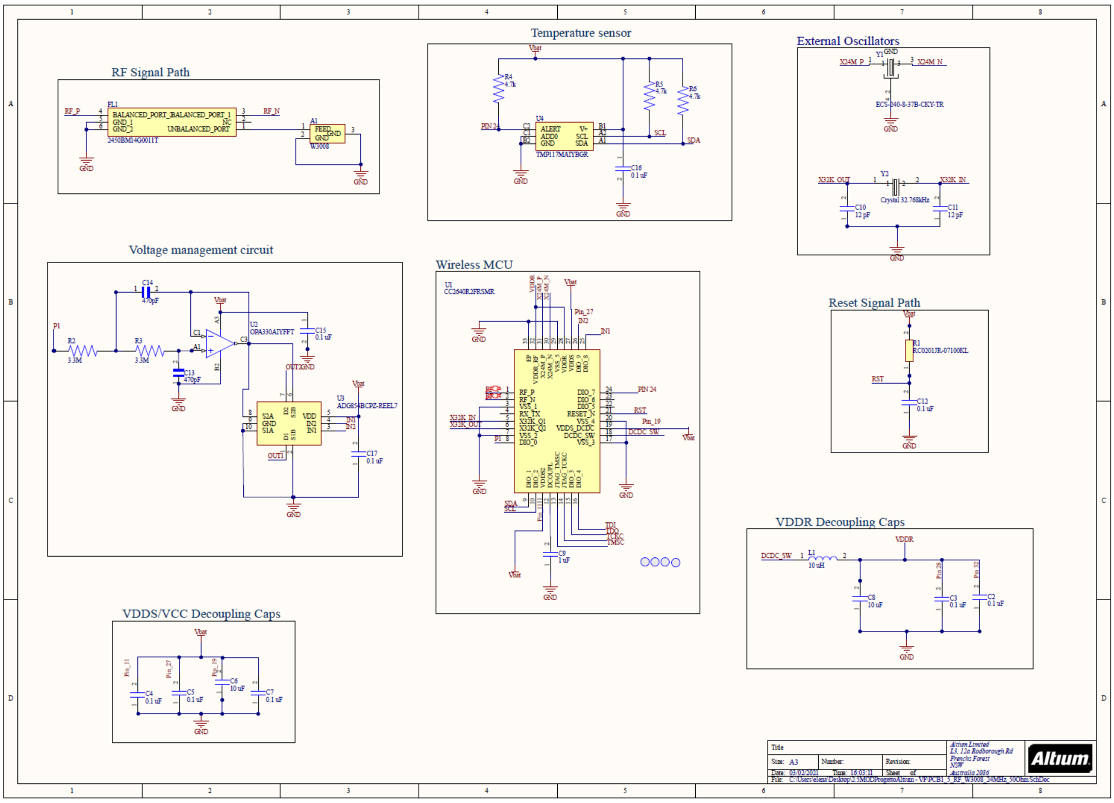

Figure 2.15: Complete device schematic.

In Figure 2.15 the complete schematic is shown and, at its center, the CC2640R2F microcontroller by Texas Instruments with the 32-PINs package is placed. The RF signal path includes the antenna (W3008), which works at 2.4 GHz for Bluetooth communication. It has a compact size ($3.2 \times 1.6mm^2$), and it is connected to a balun which is $1.6 \times 0.8mm^2$. The reset path is connected to the RST PIN, which does not have an internal pull-up, so that it has to be added externally; moreover, it should be reachable from the outside and, thus, RST is connected to a PAD. The two external oscillators are placed as suggested in the layout presented in the microcontroller's datasheet, and two decoupling circuits are needed for the VDDR and VDDS supplies. The passive components have been chosen to be as small-sized as possible; however, the inductor has quite bulky dimensions, which cannot be avoided.

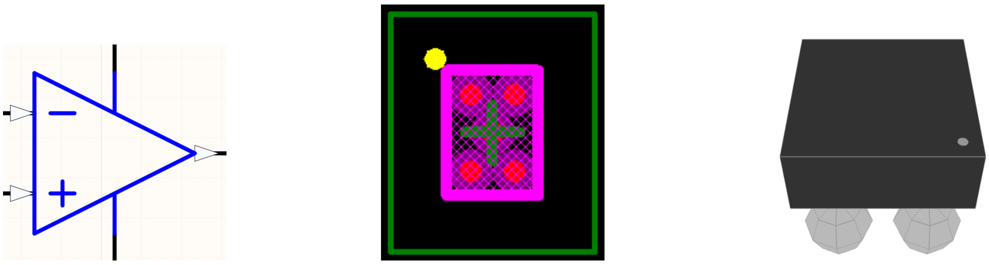

Figure 2.16: Schematic symbol, footprint and 3D body of the OPA330.

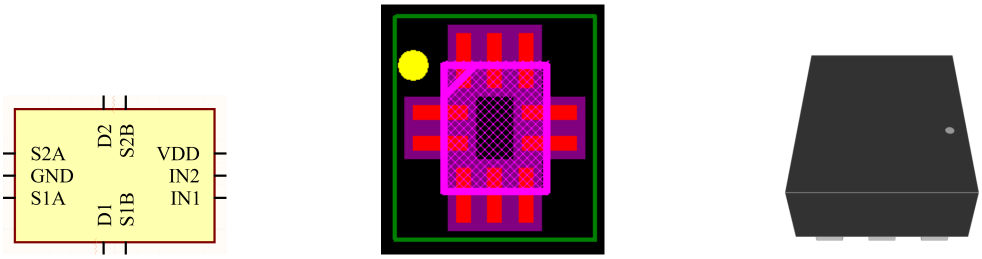

Figure 2.17: Schematic symbol, footprint and 3D body of the analog switch.

2.4.2 PCB

Once the circuit has been set, it is possible to organize the 3D printed board by placing the footprints where desired and tracing the connection paths. The board's right side is mostly dedicated to the antenna and the oscillators, whereas the left side includes the voltage control and the temperature sensor.

The antenna has been placed following the layout suggestions on its datasheet: it is surrounded by ground holes, and its connection to the balun is a 50Ω feed line. The by-pass capacitors have been placed as close as possible to the device, and the majority are 0201 SMD capacitors that belong to the X7R or X5R series. The inductor, as predictable, occupies a greater surface area of $1.6 \times 0.8mm^2$. For what concerns the temperature sensor, the suggested layout is to place it as isolated as possible except for the by-pass capacitor that should be situated nearby to the supply and ground pins. However, the surface area is not enough to grant the ideal layout solution, so that, whereas the capacitor has been placed as close as possible to the sensor pins, for the isolation of the sensor it was necessary to resort to use connection holes in order to create space between the heat sources, as the resistors, and the sensor itself. The four output PINs (TDI, TDO, TCK, and TMS) on the left side of the board are debug/test ports and are provided by the Joint Test Action Group (JTAG) port to test interconnections of the PCB and obtain information on the components. The RESET pin has a PAD reachable from the outside as well as the battery connection to supply the board. OUT1 and OUT2 are available for the connection to the membrane's electrodes, and their output is the applicable voltage that is controlled through the microcontroller, which changes its output based on the signal incoming from the BLE.

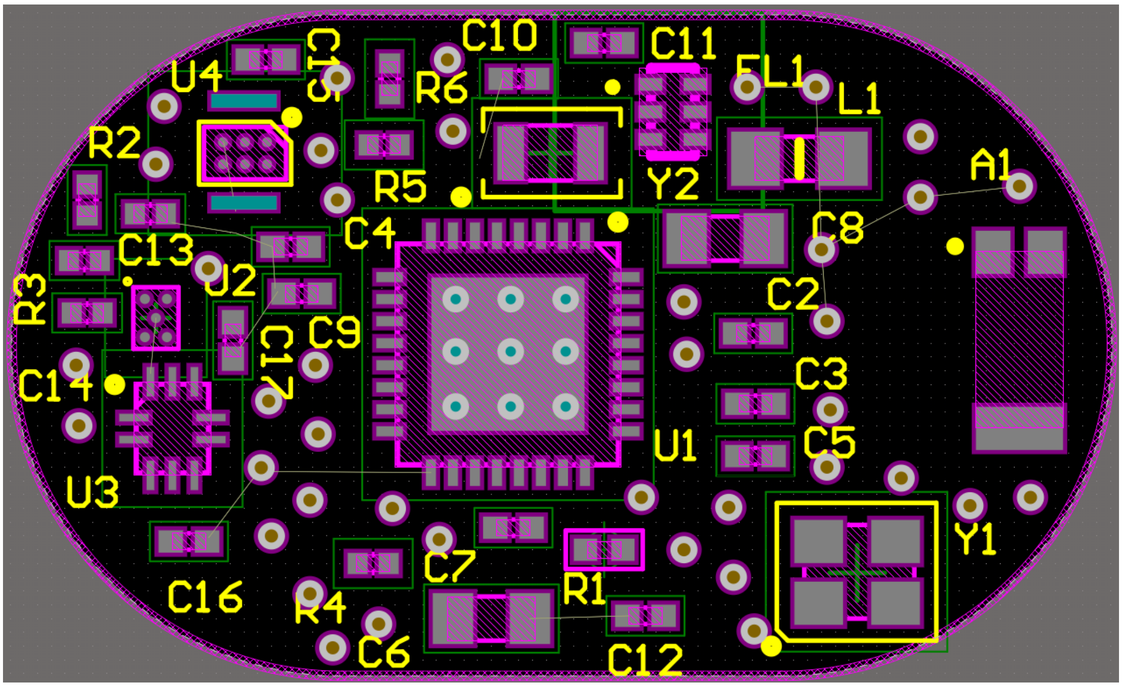

Figure 2.18: 2D picture of the PCB. The top, the bottom layers are not shown, to highlight the components and VIAs placing.

In Figure 2.18 the components placing is highlighted. The bottom and the top layer of the board are hidden in order to allow a straight visibility of the components' and VIAs organization. The mechanical layer is the definition of the appearance of the entire PCB board and contains some information on the dimensions, assembly instruction and so on. There are usually different mechanical layers and not all of them are shown in the figure above, only the ones containing components and vias size information. The minimum distance between two object has been kept at 0.254 mm and it has been ensured that the by-pass capacitors have been placed as close as possible to the respective device.

The top and the bottom layers are the circuit layers used to mount components and traces. In Figure 2.19 it can be noticed which are the connections laying on one layer or the other. The blue (bottom layer) connections provide the PADs which can be reached from the outside, the top red layer, on the contrary, includes all the components and most of the wires. The copper depositions have a variable dimension, however, their width is always greater than 1.532 mm which is the minimum accepted by the PCB assembler. Once all the components were linked to each other, the top and the bottom layer have been polygon poured, thus creating a deposited layer of copper, which made some connection easier and allowed for further

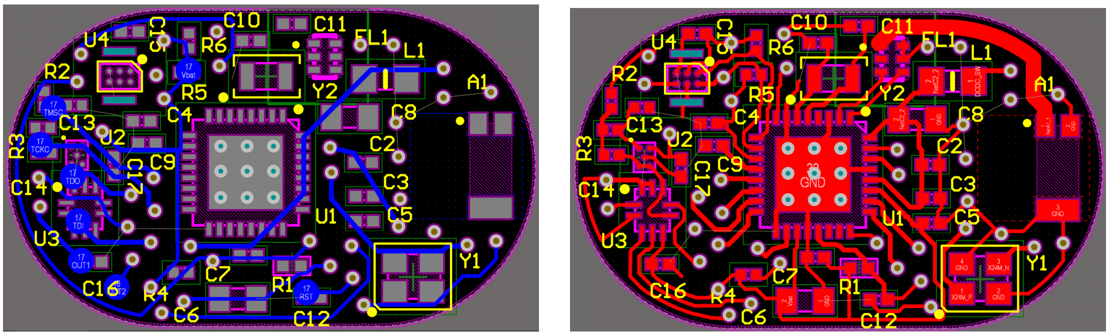

Figure 2.19: Two 2D rapresentation of the board. In (a) the bottom layer is shown, whereas it has been hidden in (b) to point out, instead, the red layer.

protection. The purple regions mainly make up the solder mask layer, whereas the yellow silkscreen layer is used to place the text information as components' names or other references needed to locate each element.

To ensure to develop a printable circuit, on the website of the PCB assembly house [97], some references such as the minimum hole size, minimum connection lines width, and clearance constraints have been considered and used to perform the *Design Rule Check*. The Design Rule Validation report is shown in Figure 2.20 and shows which rules have been checked and confirms that no errors have been found.

Warnings	**Count**
Total	**0**

Rule Violations	**Count**
Clearance Constraint (Gap=0.152mm) (All),(All)	0
Short-Circuit Constraint (Allowed=No) (All),(All)	0
Un-Routed Net Constraint ((All))	0
Modified Polygon (Allow modified: No), (Allow shelved: No)	0
Width Constraint (Min=0.152mm) (Max=0.7mm) (Preferred=0.2mm) (All)	0
Power Plane Connect Rule(Relief Connect)(Expansion=0.254mm) (Conductor Width=0.203mm) (Air Gap=0.254mm) (Entries=4) (All)	0
Hole Size Constraint (Min=0.203mm) (Max=2.54mm) (All)	0
Hole To Hole Clearance (Gap=0.254mm) (All),(All)	0
Minimum Solder Mask Sliver (Gap=0.254mm) (HasFootprint('No Footprint')),(All)	0
Silk to Silk (Clearance=0.15mm) (All),(All)	0
Net Antennae (Tolerance=0mm) (InNet('No Net'))	0
Height Constraint (Min=0mm) (Max=25.4mm) (Prefered=12.7mm) (All)	0
Total	**0**

Figure 2.20: Rule validation report drafted by Altium Designer based on the inserted manufacturer rules.

At the moment, the PCB has not been printed yet; however, the project has been designed properly and is ready for future printing and, eventually, further testing in vitro and in vivo.

Chapter 3

Numerical simulation results

3.1 SPICE setup

LTspice XVII has been used in this thesis to simulate the circuit that has been designed as described in the second chapter. This tool commonly used to check the integrity of circuit designs and to predict circuit behavior without limiting the number of nodes or elements that are part of it. The first circuital simulator was developed in the 70s and was delivered in an open-source format, then, from that, other commercial simulators have been developed. LTSpice is a free-access SPICE simulator devised by Linear Technology Corporation (LTC) and is the most widely distributed and used SPICE program in the industry. Its first version was released in 1999, whereas its last version, which is also the one in use, is LTspice XVII released in 2016. It has many models in the device library when installed, however, it also allows a user to define their own device model, or use third-party models. It allows implementing continuous analysis, as well as transit analysis for linear and non-linear circuits. It also enables sinusoidal regime analysis but, in this case, for non-linear circuits, the results are reliable only for small signals.

By using LTspice tool, it has been possible to evaluate whether the designed circuit could work in practice. The passive components could be easily placed since they only need to be sized, whereas the OP-AMP has been added to the library as it is a third-party device: the OPA330, indeed, is an operational amplifier by Texas Instruments, which includes 5 pins, two of which are used for the supply and the others are the input and output pins. The components have been placed in the schematic in the Sallen-Key configuration and a voltage generator has been added to simulate the PWM signal. Firstly, the circuit has been simulated and its performance evaluated. Then, the model of the membrane has been placed at the circuit output in order to verify the influence of the load.

3.2 PWM-based DAC

The schematic in Figure 3.1 has been simulated. V1 is needed to emulate the PWM signal, whereas V2 is the supply voltage of the OPAMP. The value of the passive components is the one chosen in the previous chapter.

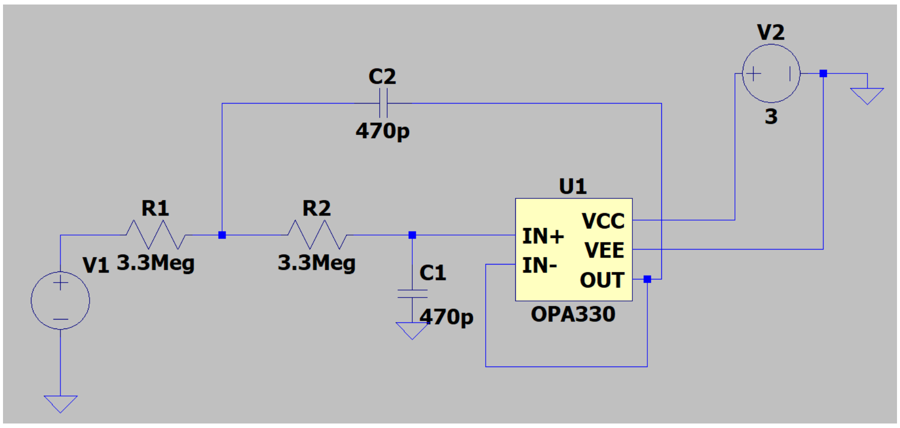

Figure 3.1: Circuit simulated without loads. V1 is the PWM signal, V2 is the supply voltage and U1 is the OP-AMP.

3.2.1 Frequency domain simulation

The simulation in the frequency domain has been performed by applying a small signal oscillating around a DC value of 1 V. In Figure 3.2, the Bode diagram of the circuit is rapresented and it shows the expected characteristics, that is to say a cut-off frequency of 100 Hz and, since it is a second order filter, a decay of 40 $\frac{dB}{dec}$. This means that from 1kHz to 10kHz it undergoes a decrease of 100 V. During the design of the filter, a quality factor Q equal to 0.5 was obtained and, consistently, a magnitude of $-6dB$ is witnessed at the cut-off frequency in the diagram. Actually, this is noticeable at a frequency sightly higher than 100Hz as the size of the passive components does not lead to that exact frequency, but a bit larger ($f_{cutoff} = \frac{2}{2\pi RC} \simeq 102Hz$). The phase acts as expected as well, in fact, at low frequencies it is 0 due to $gain(k) > 0$ so that there is not a polarity modification and, at f_{cutoff}, it is equal to $N_{poles} \cdot 45°$. At higher frequencies it becomes 180° as is normally the case for a low-pass filter, however, due to the increase in magnitude, it does not remain constant. The undesired increase is due to the direct connection between the input network and the output of the OP-AMP as pointed out in the previous chapter. At any rate, there is still a good attenuation, whose influence will be better evaluated further on with the calculation of the noise parameters on the Fourier Transform.

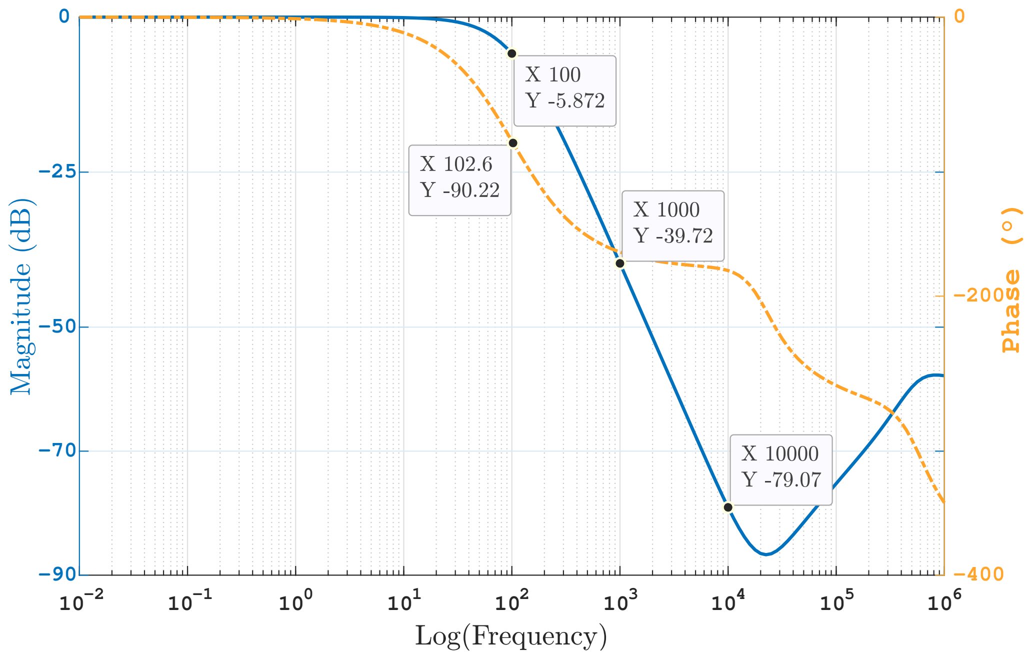

Figure 3.2: Bode diagram of the simulated circuit without load. The blue line is the magnitude in dB, whereas the orange one rapresents the phase.

3.2.2 Time domain simulation

To generate the PWM signal from the voltage generator, it has been set a square wave between 0 and 3 V with a period of $\frac{1}{24MHz} \cdot (2^{N_{bit}})$, which, given that it has been chosen an 8-bit resolution, is $\simeq 5.3\mu s$. Different duty cycles have been obtained modifying T$_{on}$, which indicates the duration of the 3V portion in the entire period. Knowing that in practice it will assume only discrete values, T$_{on}$ has been modified considering steps of $\frac{T_{period}}{2^{N_{bit}-1}}$. In Figure 3.3 the resulting input signals are shown for different duty cycles.

The output signal of the filter is supposed to assume a constant value proportional to the duty cycle of the PWM signal. As it can be noticed in Figure 3.4, the output analog voltage is consistent with the duty cycle imposed.

As predictable, the active and passive components introduce a delay which brings up a time for rising and falling, when the output changes, of about 10 ms as can be noticed in Figure 3.5.

During the simulations, however, when the input has a duty cycle of 0% or 100%, the extremes of the range cannot be reached and some bits get lost. In Figure 3.6 the output for values very close to the range boundaries is shown. As it can be noticed, there is a plateau with the subsequent waste of 3 LSBs at each extreme. This is not a problem since the applied potential does not need to be that precise at the upper limit, whereas, if exactly 0V are needed, this can be easily obtained by imposing both the inputs of the analog switch at 0.

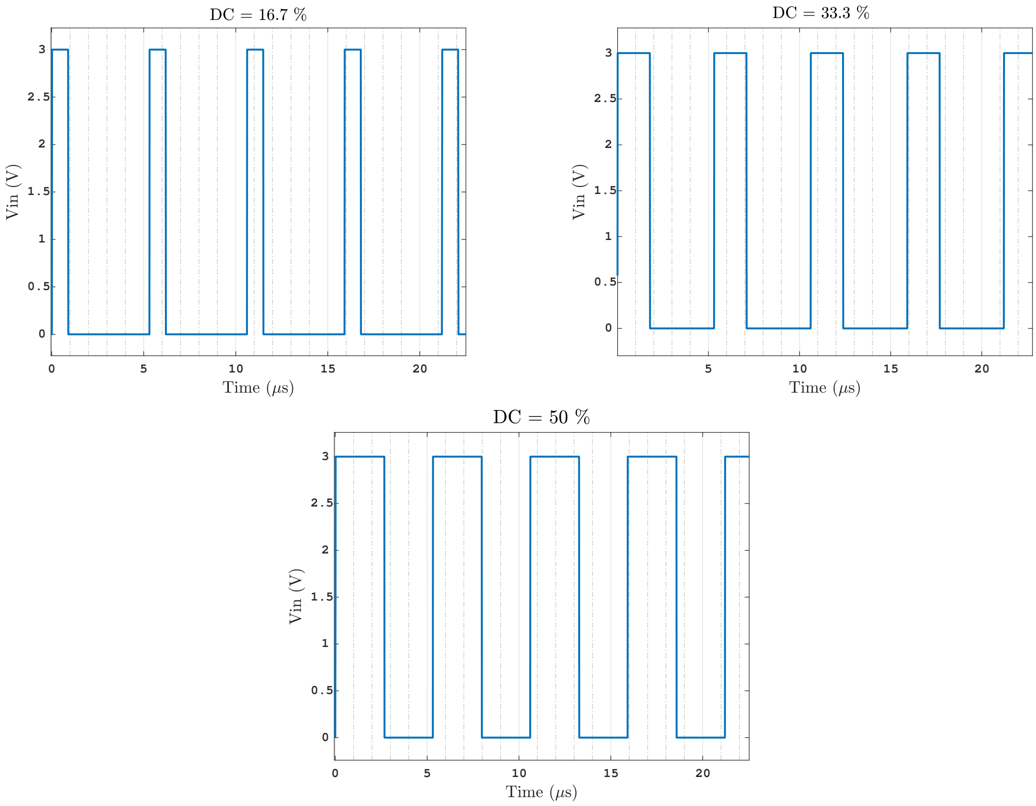

Figure 3.3: PWM signal simulated through the voltage generator with a square wave with different duty cycles.

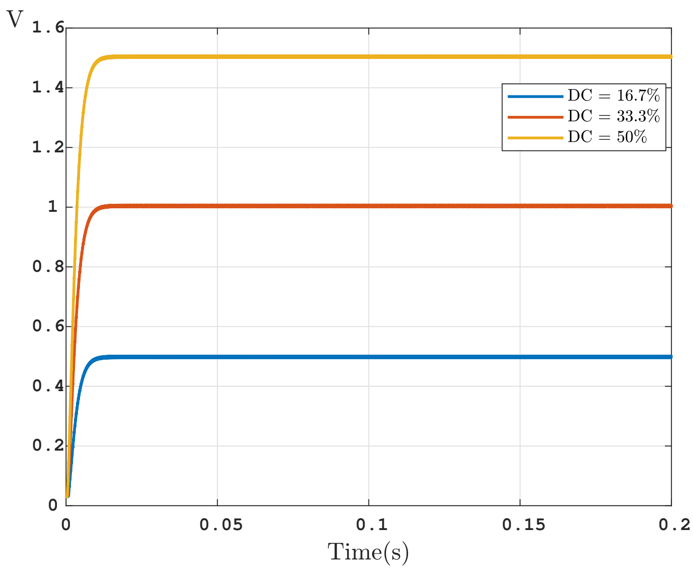

Figure 3.4: Output of the filter at different duty cycles of the input signal.

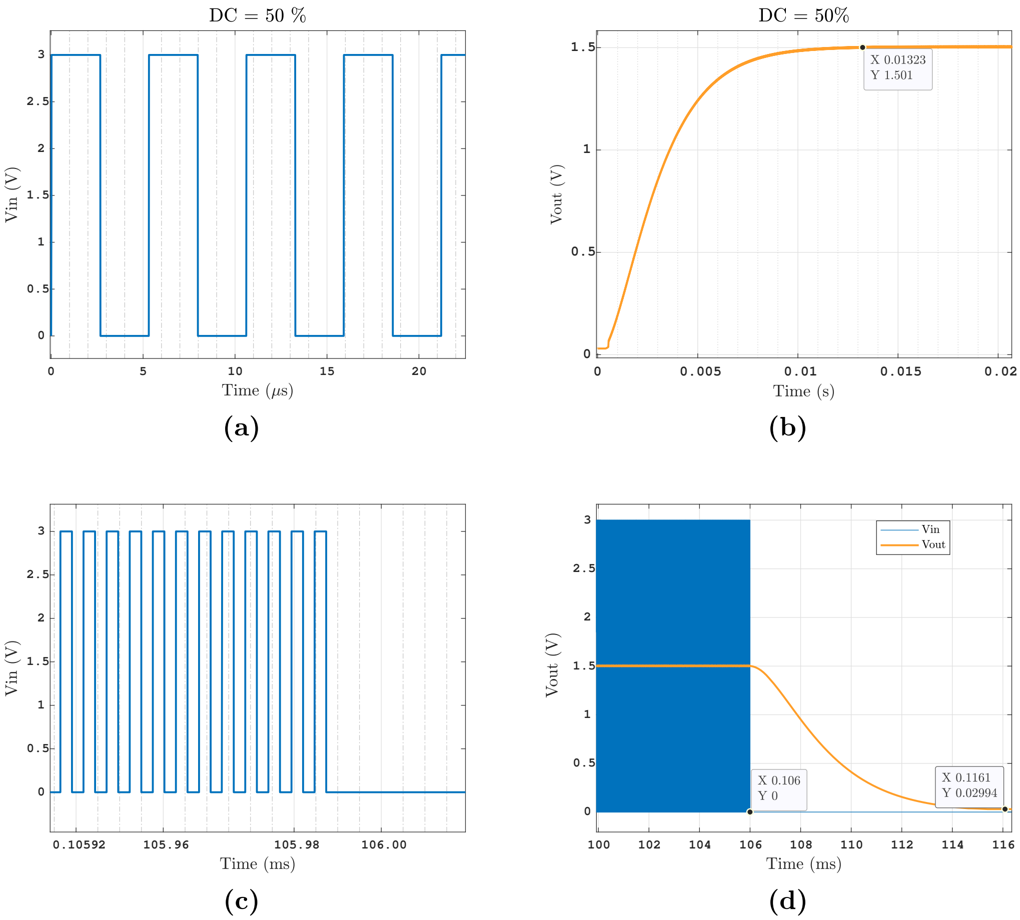

Figure 3.5: In these figures are rapresented the rising edges of the output signal ((b) and (d)) when an input signal is applied ((a) and (c)). In both cases it takes about 10 ms to reach their maximum (b) or their minimum (d).

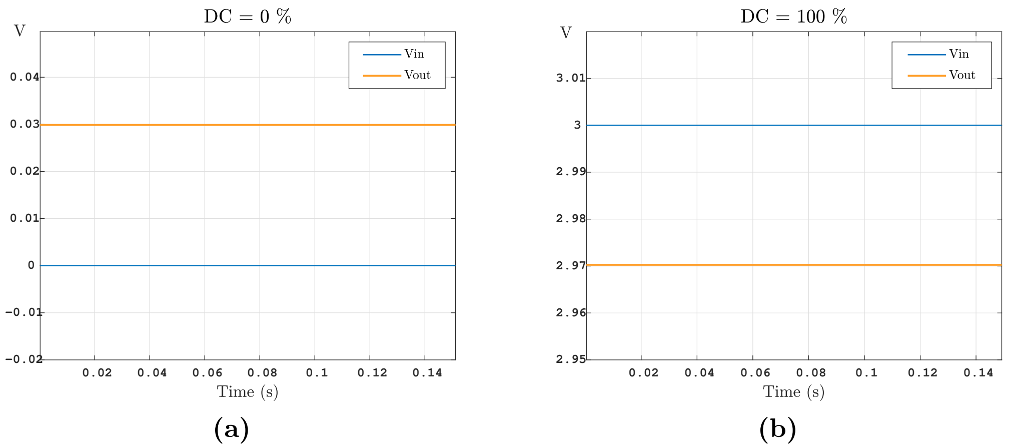

Figure 3.6: Output voltage with an input signal with a duty cycle of either 0% (a) and 100% (b). In both cases the voltage deviates from the expected value.

3.2.3 DAC static performance

Dealing with a digital to analog converter, there are some parameters that is possible to evaluate in order to understand if it works in an acceptable way. By implementing some simulations in the time-domain, the linear characteristic of the DAC has been evaluated and compared to an ideal DAC. In particular, for each duty cycle value, a simulation of 400 ms has been performed. In order to exclude the 10ms transition, the second half of the simulation has been considered and the mean value has been taken.

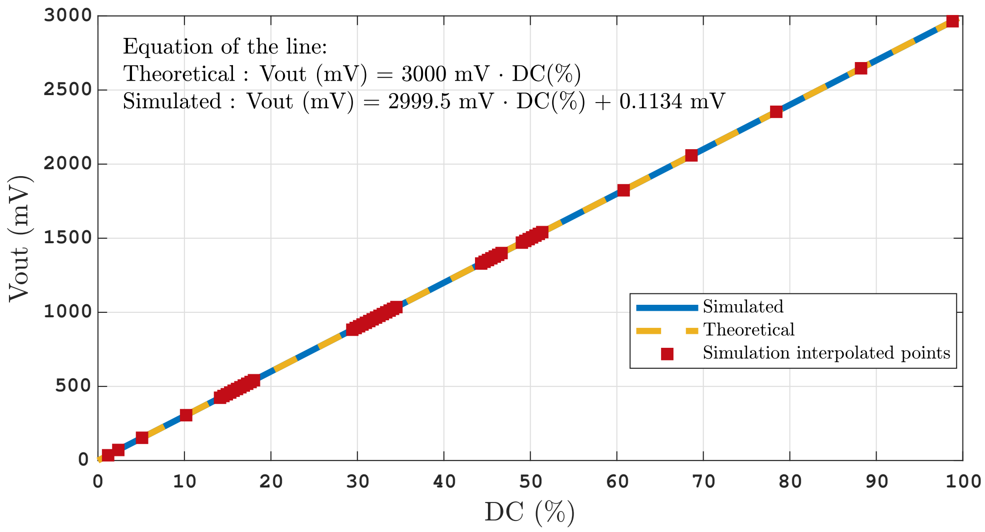

Figure 3.7: Transfer function of the DAC designed. The orange line is the reference theoretical behaviour, whereas the blue one has been derived interpolating the red points with the least-squares method and excluding the extreme values.

The characteristic is shown in Figure 3.7. The theoretical and simulated line are almost completely superimposed. The interpolation of the simulated line has been performed by minimizing the least-square error and for values ranging from 35 mV to 2964 mV to exclude the undesired effects at values very close to the range boundaries. The least significant bit (LSB) corresponds to a voltage of $\simeq 11.7mV$, this means that variations smaller than this value cannot be detected. The resulted gain and offset error are:

$$\text{Gain Error} = 0.017\% \qquad\qquad \text{Offset Error} = 0.1134mV$$

Both are small enough to be neglected, as the offset error is 100 times smaller than the least significant bit; moreover, the deviation of the points from the interpolated line is almost nil (indeed, R^2=1).

The differential non linearity (DNL) quantifies the deviation of each point from the transfer characteristic function. This measure can be used to evaluate both monotonicity and linearity of the DAC. It has been evaluated for some successive points in regions of the range that have been considered with more attention as they are the same that will be applied to the membrane model.

DC (%)	Vout (mV)	(Vout (i)-Vout(i-1)) (mV)	DNL (mV)	DNL (LSB)
15.69	470.860	-	-	-
16.08	482.575	11.715	-0.050	-0.004
16.47	494.196	11.621	-0.144	-0.012
16.86	506.045	11.849	0.084	0.007
17.25	517.858	11.812	0.047	0.004
17.65	529.692	11.834	0.069	0.006
18.04	541.386	11.694	-0.070	-0.006
32.16	964.510	-	-	-
32.55	976.276	11.766	0.001	0.000
32.94	988.071	11.795	0.031	0.003
33.33	999.892	11.821	0.057	0.005
33.73	1011.679	11.787	-0.022	-0.002
34.12	1023.455	11.776	-0.011	-0.001
34.51	1035.195	11.741	-0.024	-0.002
49.02	1470.387	-	-	-
49.41	1482.117	11.730	-0.035	-0.003
49.80	1493.904	11.787	0.022	0.002
50.20	1505.686	11.782	0.018	0.001
50.59	1517.461	11.775	0.010	0.001
50.98	1529.194	11.733	-0.032	-0.003
51.37	1540.978	11.784	0.019	0.002

Table 3.1: DNL calculated in different regions of the range and, more specifically, nearby the voltage values that will be simulated with the load. The obtained values are all minimal, of about or even less than the 1% of the LSB.

In Table 3.1 the results are shown: the DNL values are minimal compared to the least significant bit, so that they do not have any relevant impact on the output voltage.

Frequency domain performance

The main frequency domain parameters have been evaluated on the Fourier transform of the output voltage. A simulation has been performed in time with an input signal with a 50% DC and for a duration of 2s. The first half has been not considered, in order to take a signal well distant from the transient and the data has been exported from LTspice to elaborate them in MATLAB and the transform has been calculated using the function *fft()*. Since LTspice usually provides an unevenly sampled output, the signal has been interpolated choosing a sampling frequency through some tests that led to finding a value that did not entail aliasing problems, then the transformation has been easily computed. In Figure 3.8, the Fourier transform is shown. It has a first high peak at about 188 kHz which is the frequency of the input signal and, then, at all the subsequent harmonics (377 kHz, 564 kHz,...). At 0 Hz it assumes the expected value ($\simeq 1.5V$), whereas at all the other frequencies undergoes a significant reduction as it can be noticed by the comparison of the magnitude at fundamental and harmonics frequencies between the input and the output signal (see Figure 3.9).

The Fourier transform allowed for further performance analysis through the calculation of the signal to noise ratio (SNR) and the spurious free dynamic range

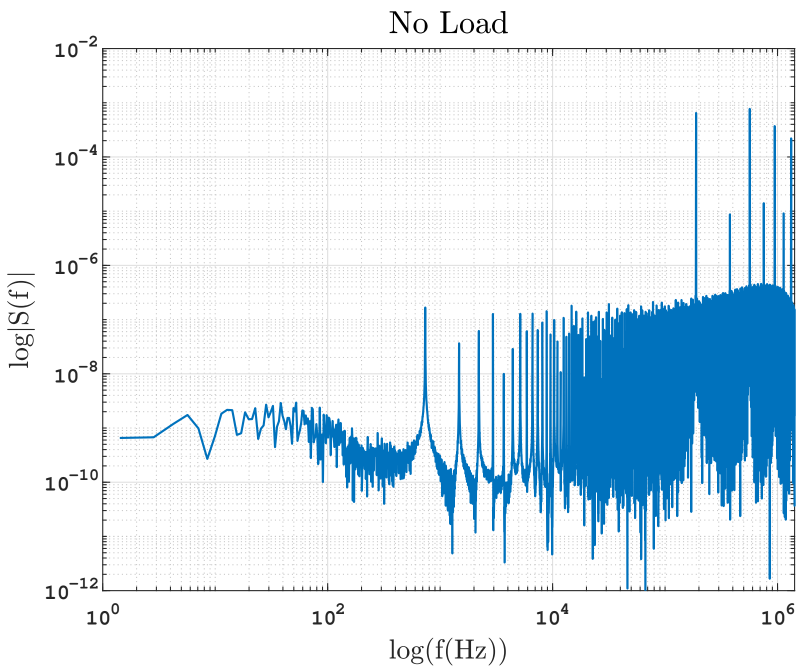

Figure 3.8: Fourier Transform of the output of the designed DAC with an input PWM signal with a 50% DC.

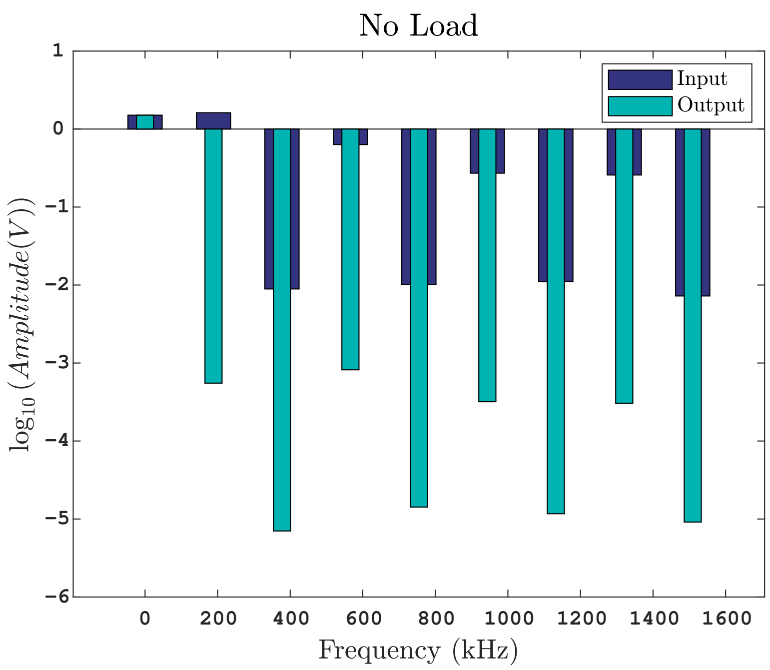

Figure 3.9: Comparison between the harmonics and fundamental components between the input and the output signal. As it can be noticed, at 0 Hz there is not a significant difference, whereas for higher frequency the harmonics are widely reduced.

(SFDR). Some other parameters associated to distortion that are usually evaluated could not be used for this application since the output is a 0Hz signal. The Signal to Noise ratio (SNR) has been evaluated as the output continuous signal over the root-mean square value of all the other frequency components, and it's value is 112.05 dB, which is largely acceptable for a 8-bit DAC, so that the signal of interest is sufficiently higher in magnitude than the noise which is related mainly to the input signal harmonics. However, this is an ideal result, since in the simulations many practical aspects are not considered. The spurious free dynamic range (SFDR) enstabilish how much magnitude is available free of noise, it takes the highest spourious peak and compares it with the signal itself. In the simulation, the highest peak resulted the second harmonics and the ratio with the 0Hz magnitude gives a $\simeq$ 68.49 dB SFDR, that is in line with the values that can be found in some datasheets.

3.3 Membrane model and circuit simulation

After making sure that the digital-to-analog converter works as expected during the simulations, the membrane model has been added to predict its influence on the DAC performance, in order to verify if good behavior can be expected in the experimental phase. The membrane has been modeled as well explained in the literature, through a resistor in series with an RC parallel. The component values were previously measured on the nanochannel silicon membrane developed by the research group of the Houston Methodist Research Institute and have been published in a paper by Di Trani et al. (2020) [13]. Fitting electrochemical impedance spectroscopy measurements, they quantified the double layer capacitance (C_{dl}), the resistors that modelize the charge transfer and the electrolytic solution (R_{ct} and R_a) and also the Warburg coefficient (W). These measurements were performed on both SiO_2 and SiC membranes, thus allowing a comparison between the material that is usually employed for electrostatic gating and the biocompatible one of which the membrane at issue is made. Since the electrochemical characteristics of the membrane have a dependency on the voltage applied, the measurements have been performed under specific applied tensions: 0 V, $\pm$0.5 V, $\pm$1 V and $\pm$1.5 V and, for each of them, three measurements have been performed. For these analysis the median of the three values has been taken into account to implement the circuits to simulate the membrane load.

Although the values for the two materials are of a comparable order of magnitude, some differences can be detected particularly in the double layer capacitances, which is probably the result of a different material porosity given the dependency of the electrical double layer capacitance on the surface area [98]. Moreover, also a difference in the charge transfer resistors is emerged both in terms of values and trend with the variation of the applied tension. This phenomenon has been explained as the result of the different surface charge between the two materials: the higher quantity of available SiO^- sites probably leads to an increase in electron exchange.

V_{GS} (V)	Ra (kΩ)	Rct (kΩ)	Cdl (pF)	W (μ)
0	5.084	665	756.9	2.78
0	5.047	659	756	2.66
0	5.007	668.3	807.7	44.8
0.5	5.051	875.4	769.8	3.43
0.5	3.396	724.7	915.8	3.347
0.5	8.373	766.1	863.9	3.412
1	5.099	823	750.6	14.17
1	3.41	702.5	864.2	13
1	3.375	758.6	849.8	11
1.5	5.072	490.1	708.6	37.94
1.5	3.368	453.1	798.4	35.8
1.5	3.376	507.4	789.2	30.48
-0.5	5.053	760.1	784.8	6.48
-0.5	3.391	715.3	959.6	5.128
-0.5	3.359	856.4	862	4.487
-1	4.948	444.8	783.3	29.66
-1	3.377	461	934	23.11
-1	3.363	541.9	871.5	16.48
-1.5	4.907	289.7	782.5	42.43
-1.5	3.355	330.4	889.2	29.4
-1.5	3.371	348.2	900.1	23.46

Table 3.2: Component values of the SiC membrane model. For each component and for each voltage, the median value is highlighted in red.

V_{GS} (V)	Ra (kΩ)	Rct (kΩ)	Cdl (pF)	W (μ)
0	10.22	85.53	172.9	2.68
0	10.8	249.9	176.4	2.489
0	9.724	10^{-6}	2375	0.05683
0.5	10.63	329	178.7	2.12
0.5	8.202	114.3	202.9	26.24
0.5	2.119	4.475	0.2697	2.501
1	10.75	273.5	257.9	7.267
1	8.153	240.1	211.3	7.261
1	3.696	4.093	0.6406	3.289
1.5	10.66	280.7	180.4	23.01
1.5	4.747	665	1.228	6.347
1.5	4.886	5.089	1.368	6.728
-0.5	11.16	138.8	244.1	17.22
-0.5	8.295	148.9	225.3	10.62
-0.5	4.381	4.489	0.9984	4.798
-1	10.93	86.64	191.6	61.14
-1	8.202	114.3	202.9	26.24
-1	8.25	92.56	212.4	34.59
-1.5	10.8	68.5	208.2	34.29
-1.5	8.178	68.39	198.3	32.83
-1.5	8.391	87.32	217.4	217.4

Table 3.3: Component values of the SiO_2 membrane model. For each component and for each voltage, the median value is highlighted in red.

3.3.1 Warburg element lumped model

The Warburg element is an impedance used to simulate the slow diffusive processes of an electrochemical cell. It is defined as a constant phase element (CPE) as it has a constant phase at 45° and, thus, a magnitude that decreases linearly with the increase of frequency as shown in Figure 3.10.

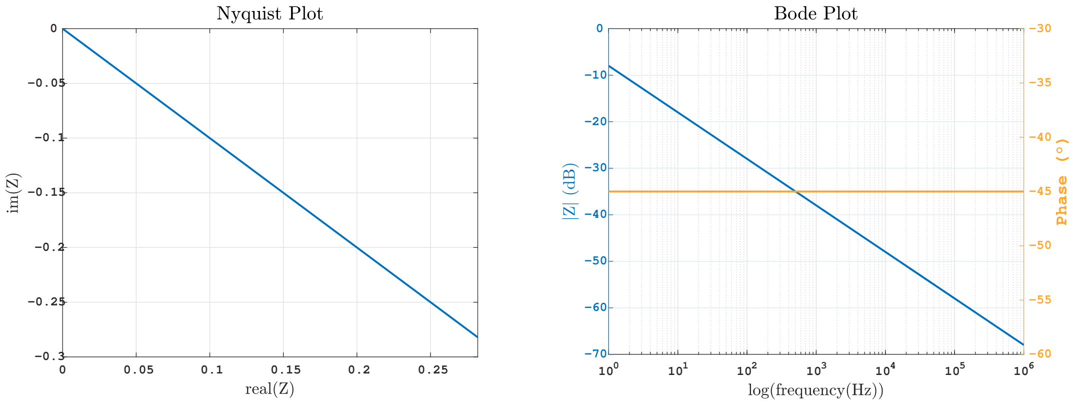

(a) (b)

Figure 3.10: Warburg impedance's Nyquist plot (a) and Bode plot (b) for a coefficient equal to 1.

The electrical model used for the constant-phase element in this thesis was proposed by Valsa et al. [68], who developed an RC lumped circuit defining the number of branches and of components based on some initial parameters. The frequency range is the interval in which the phase is needed to remain constant, while the choice of the first resistor and/or capacitor should be made based on the known Warburg coefficient.

A frequency band from 1 Hz to 1 MHz was considered along with a small oscillation around the constant phase value. The number of branches increases with the decrease of the phase oscillations and with the increase of the extent of the frequency band. A MATLAB script has enabled a fast evaluation of all these parameters and of the resulting model, thus leading to a good compromise among the frequency range, the number of branches, and the oscillations around the constant phase value. As an example, the scheme realized for a 1.5 V applied voltage at the Silicon-Carbide membrane is shown in Figure 3.11. The value of the Warburg coefficient is equal to $35.8\mu\Omega(s^{-\frac{1}{2}})$ as listed in the Table 3.2.

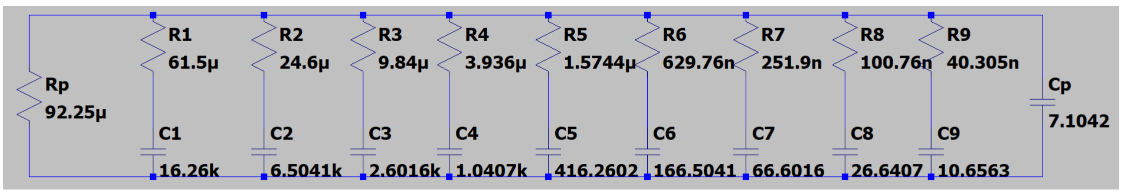

Figure 3.11: Schematic of the Warburg impedance with a coefficient equal to $35.8\mu\Omega(s^{-\frac{1}{2}})$

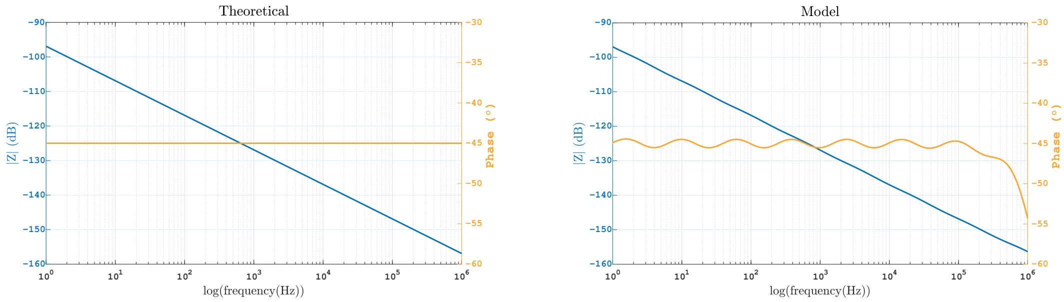

Figure 3.12: Comparison between the Bode diagram of the ideal Warburg impedance and the one obtained with the model. The magnitude coincide almost perfectly, whereas the phase has some small oscillations around the desired value (45)

Once the models for each potential have been set, further simulations on LTspice allowed a comparison with the ideal result. In Figure 3.12, the model's Bode diagram is compared to the theoretical desired one and, as it can be noticed, they are similar. This allowed for further analysis with the new model. It should be noticed that this element has a much lower impedance with respect to the other components, this means that it could probably be neglected without leading to a relevant change in the simulation results. However, for the sake of completeness, the model has been used as it is, without any approximation.

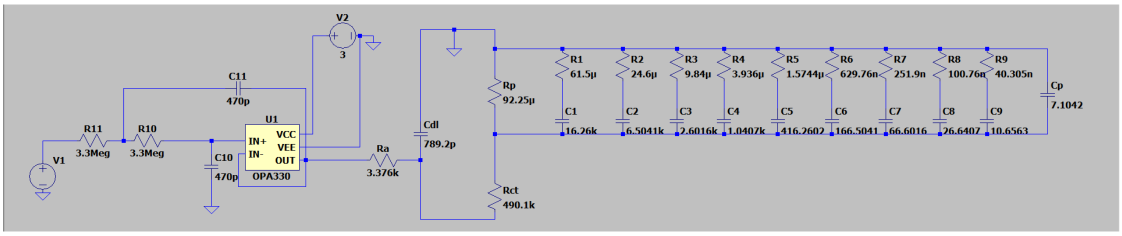

Figure 3.13: Simulated circuit for SiC membrane at an applied voltage of +1.5V.

3.3.2 Frequency domain simulation

The simulation has been performed in the frequency domain between 0.01 Hz and 1 MHz for a small oscillating signal around the DC value that corresponded to each voltage applied. Phase and magnitude are shown in Figure 3.14 for both the materials and different applied voltages. At low frequencies, there is not any detectable difference, whereas, at higher frequencies, the increase of the Bode response shows a slight dependency on the resistance R_{ct} that, although assumes generally comparable values, some minimal differences can be detected. This fact is, again, a consequence of the direct path between the circuit network output and input. For example, it can be noticed that the SiO_2 membrane charge-transfer resistance, when a 1.5V or 1V potential is applied, assumes the utmost values causing a higher increase in magnitude with respect to the others. However, the difference is minimal, thus it does not affect significantly the performance.

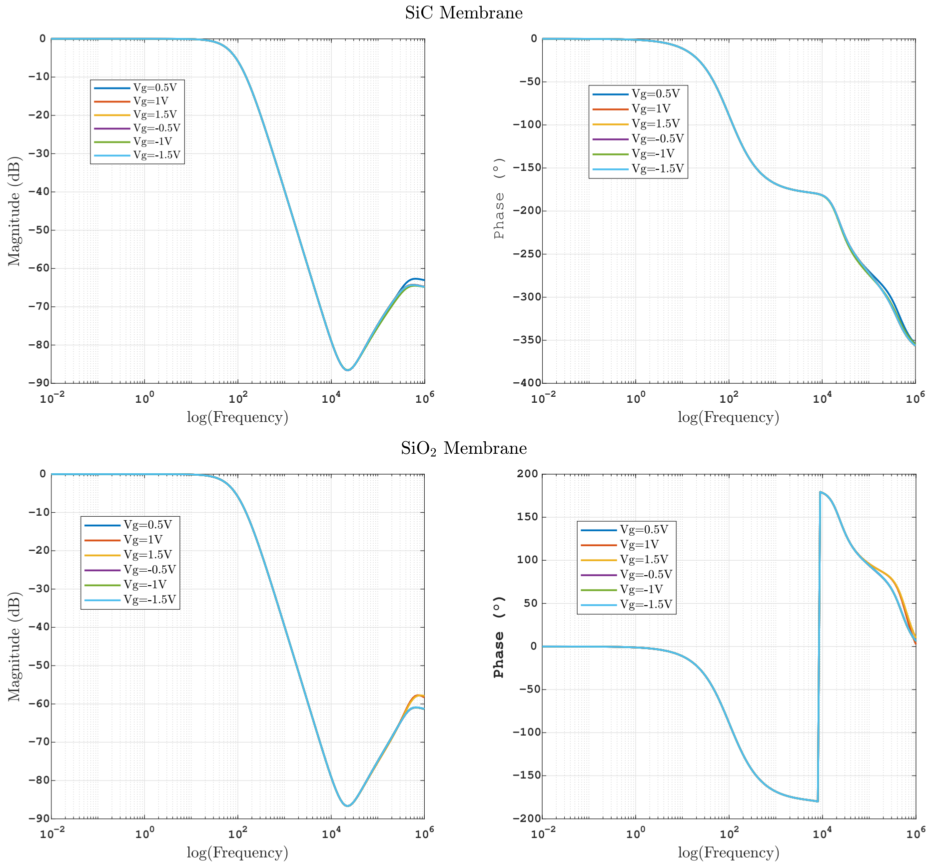

Figure 3.14: Bode diagrams at different applied voltages for SiC (a) and SiO_2 (b) membranes.

For what concerns the phase behavior, it is not notably influenced by the membrane models, and they act in the same way as the simulations without any load.

3.3.3 Time domain simulation

For the transient analysis, the input signal has been set in the same way as in the previous case (see Figure 3.3). In Figure 3.15 it can be seen the behavior of both membranes that is coherent with the one expected. When a 50% DC input signal is applied, the output, after a rising edge of about 10ms, is equal to 1.5V; at a 33% DC, it becomes 1V; whereas, at 17%, it is equivalent to 0.5V and the same for negative potentials. The same voltage is generated for both positive and negative tensions at the same duty cycle and the difference between the schemes lies in the models' components values.

In the time domain, by taking a deeper look at the output signals, it is possible to notice a slight difference between the two membranes as SiO_2 presents higher oscillations around the average value. This phenomenon is probably associated with the capacitor's size since probably a higher capacitance entails a more significant transient that manifests itself in terms of smaller oscillations. To analyze this aspect, applied voltages equal to -0.5V and 1.5V have been considered and are shown

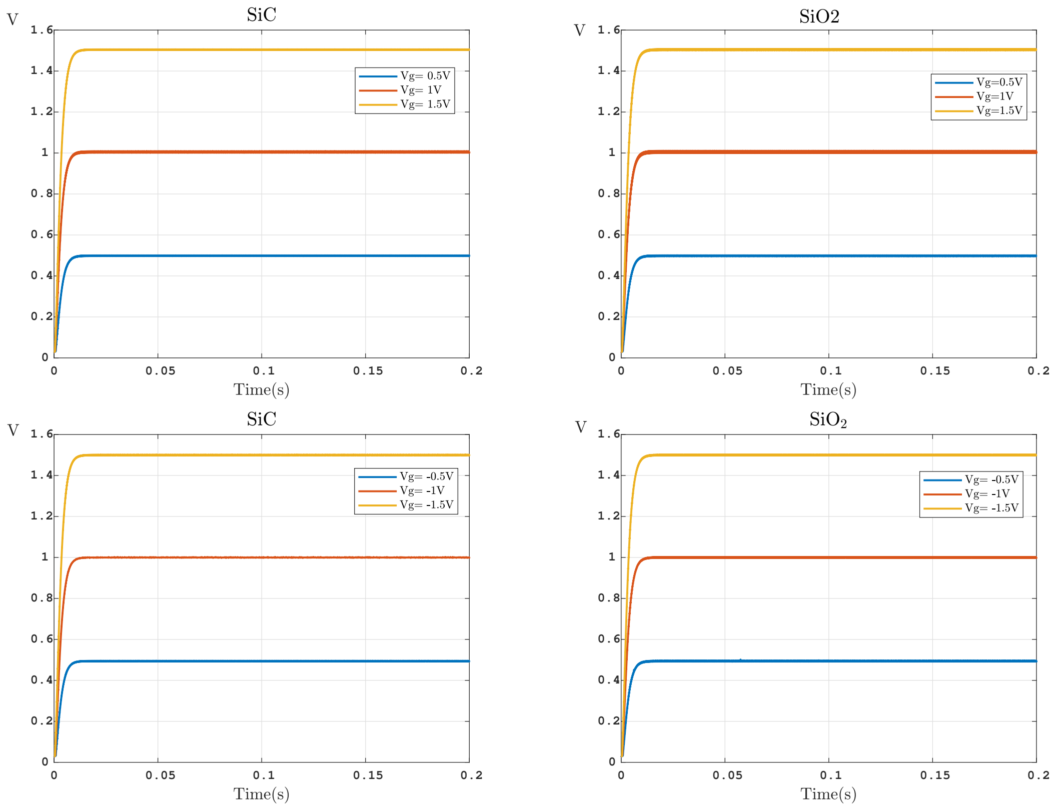

Figure 3.15: Output voltages corresponding to different input applied with duty cycles equal to 16.7%, 33.3%, 50%. The model of the membrane depends on the potential. The graphs show a behaviour coherent with the PWM signal duty cycle.

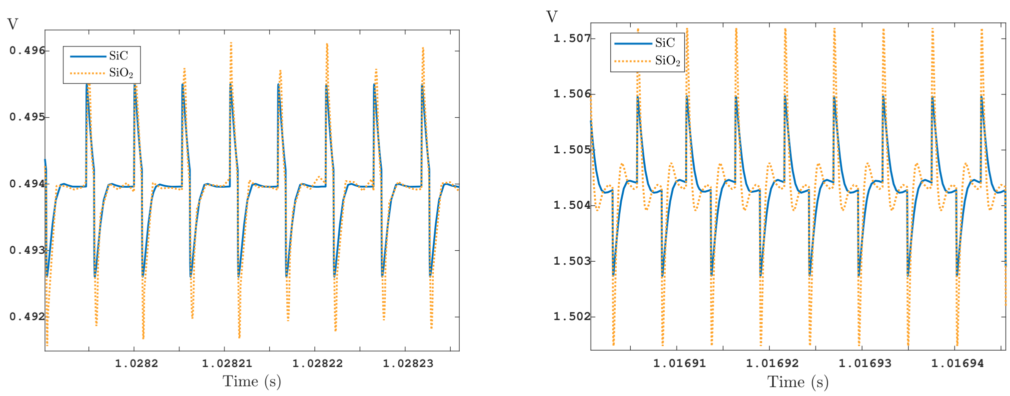

(a) (b)

Figure 3.16: Comparison of the oscillations for SiC and SiO_2 membranes at different voltages. (a) shows the fluctuations at 0.5V and (b) at 1.5V. The figure highlights the dependency from the value of the capacitance. Concerning the LSB, however, the oscillations are all negligible.

in Figure 3.16. Their models, indeed, have either the least different capacitances or the most marked gap. The maximum oscillations at -0.5V are 5 mV and 2.9 mV for respectively SiO_2 and SiC, whereas, at 1.5V they become 5.7 mV and 3.2 mV. The higher C_{EDL}, the smaller the oscillations. However, they are negligible since they are less than half of the least significant bit.

3.3.4 Comparison of performance with different membranes

Some paragraphs earlier, the Fourier transform of the converter without the membrane has been evaluated. Following an ilk process, the same has been done for SiC and SiO_2 membranes, thus allowing the comparison with each other and the no-load case. Therefore, the transforms have been computed for a simulation with the PWM signal working at a 50% duty cycle and it is shown in Figure 3.17.

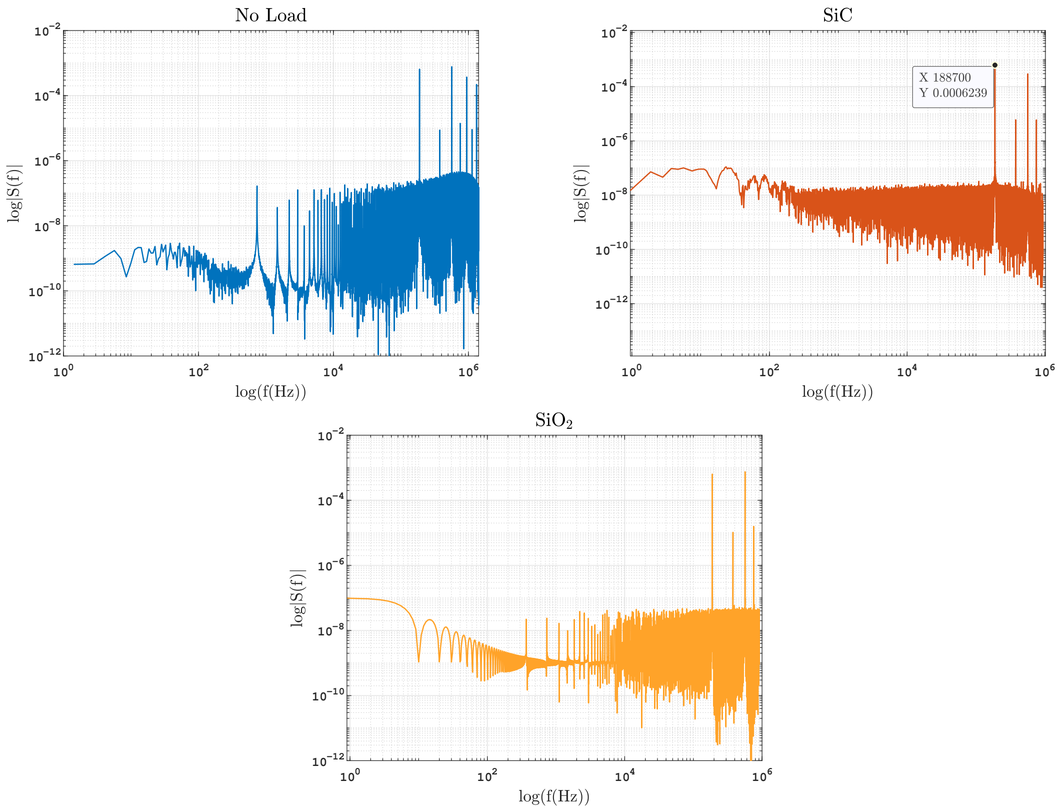

Figure 3.17: Comparison of the Fourier Transform of the output voltage without load and with SiC and SiO_2 membranes. They all show the same behaviour with a first peak at the input frequency and the following at the successive harmonics.

The three Fourier transforms show assimilable characteristics: the first peaks are all localized at 188700 Hz that corresponds to the simulated period of 5.3μs, whereas the successives correspond to the harmonics of the signal frequency. They behave similarly in terms of magnitude, even though SiO_2 higher peak coincides with the second harmonics, whereas for the SiC, it is the fundamental frequency. At 0Hz, all these simulations assume the constant output value of 1.5V, as shown in Table 3.4.

To evaluate the filter's effect on the fundamental frequency and the successive harmonics, for each case it has been compared the input, and the output Fourier transform at the most significant frequency values.

	Amplitude (V)
SiO_2	1.5043
SiC	1.5043
No Load	1.5043

Table 3.4: Magnitude of the Fourier Transforms at 0Hz without the load and with the two different membranes.

	$\frac{rms(harmonics_{out})}{rms(harmonis_{in})}$	$\frac{rms(V_{out}(0Hz))}{rms(V_{in}(0Hz))}$
SiO_2	-65.22 dB	-0.004 dB
SiC	-68.25 dB	-0.008 dB
No Load	-65.32 dB	-0.008 dB

Table 3.5: Ratio between the magnitud of the Fourier transform at the harmonics and 0Hz. As desired the DC output remains almost unchanged, whereas the other components are significantly reduced.

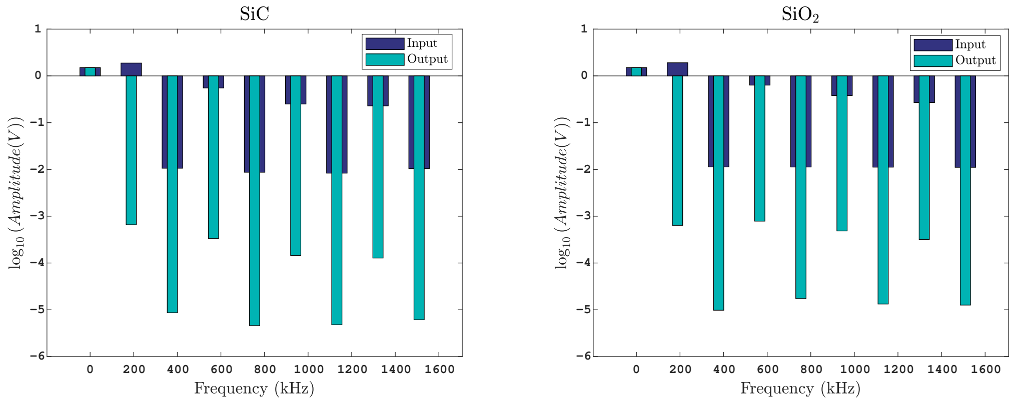

Figure 3.18: Comparison of the magnitude of the Fourier Transform at precise frequency values between the input and the output signals.

In Figure 3.18 it is shown the diminishing of the magnitude of the principal frequency components except for the one at 0Hz, which is almost unchanged. Starting from the Fourier transform of the signal, it is possible to evaluate some parameters such as SNR (signal to noise ratio), SFDR (spurious free dynamic range), and ENOB (effective number of bits), which, altogether, give essential information about how much noise is introduced and in what magnitude the harmonics influence the performance of the converter.

The SNR assumes very high values for the three conditions, also considering that an 8-bit DAC is in use; moreover, the load does not influence enough to induce an evident variation. A noticeable aspect is that the best performance is witnessed for the SiC membrane, probably due to the model itself and also to the fact that the silicon carbide output voltage undergoes much smaller oscillations as observed previously (see Figure 3.16). SFDR assumes greater values and this could have been foreseen since only the highest local maximum is considered instead of the root mean-square of the entire range (see Table 3.6). The ENOB is mainly used to evaluate whether the number of bits in use is too high. Indeed, when the resolution is smaller than the oscillations of the signal, the bits could not be distinguished sharply and some of them could get lost. In a real DAC the effective number of bits is always smaller than the designed value, since there are always disturbances and noises due to many different sources. In this case, since the device under test is not properly a DAC and the input is a square wave, it has been decided to evaluate how the highest income of interference influences the performance, by adding to the least significant bit value, the amplitude of the most prominent peak in the Fourier Transform and then it has been translated into a binary information. The results in Table 3.6 show very high ENOBs with equal values up to the second decimal, this means that, in all these cases, the oscillations around the analog voltage are not high enough to compromise the DAC resolution.

$$\begin{aligned}
&N = 8 \ \textit{(Number of bits)} \\
&\textit{Total uncertainty (TU)} = \frac{1}{2^N} + \frac{\textit{Amplitude of the highest spurious peak}}{\textit{Full range}} \\
&ENOB = \frac{-\log_{10}(TU)}{\log_{10}(2)} \ \textit{(Change of base to obtain a value in bits)}
\end{aligned} \tag{3.1}$$

	SNR (dB)	SFDR (dB)	ENOB (bits)
SiO_2	110.50	65.98	7.98
SiC	112.80	67.27	7.98
No Load	112.05	68.49	7.98

Table 3.6: Table with the parameters calculated on the Fourier transforms for each considered case.

3.3.5 Influence of the Warburg impedance

For the sake of completeness, all the simulations have been performed considering also the Warburg impedance in order to have reliable results. However, since it assumes very small values it has been verified if and how the results are influenced by its presence.

First, it has been performed AC analysis of the impedance with and without Warburg element, which matched perfectly with each other (shown in Figure 3.19), then it has been evaluated its influence in the designed system transient simulation and, even at a high detail level, they are almost indistinguishable as it can be noticed in Figure 3.20. Finally, it has been determined also its influence in the complete system performance (Table 3.7), and it can be safely concluded that the overall impact of the Warburg element is negligible.

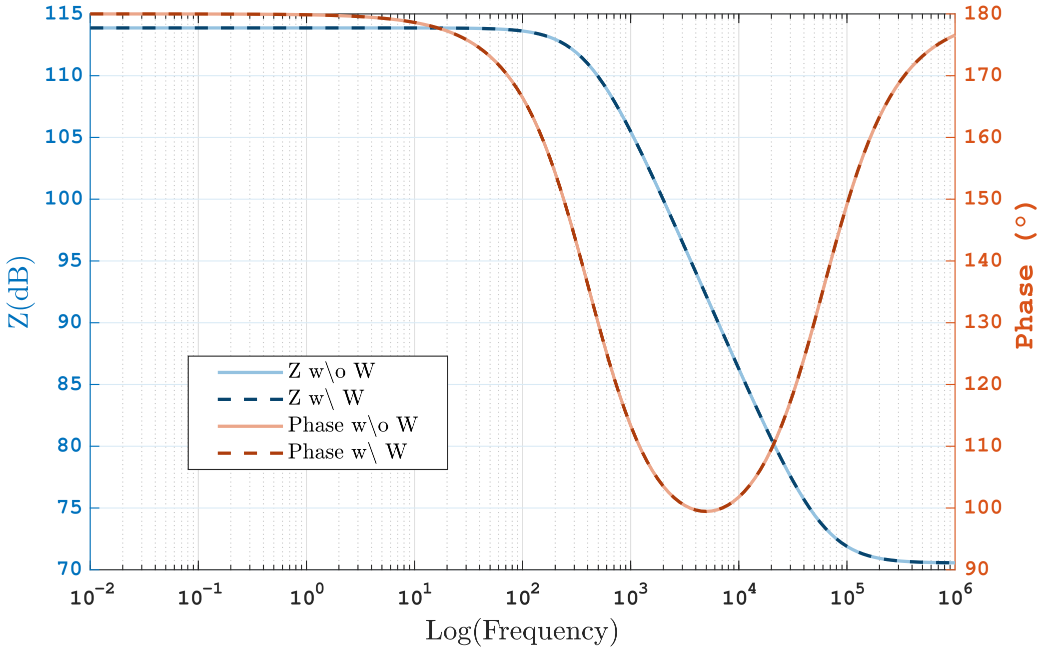

Figure 3.19: Comparison between the AC analysis of the membrane impedance with and without the membrane model.

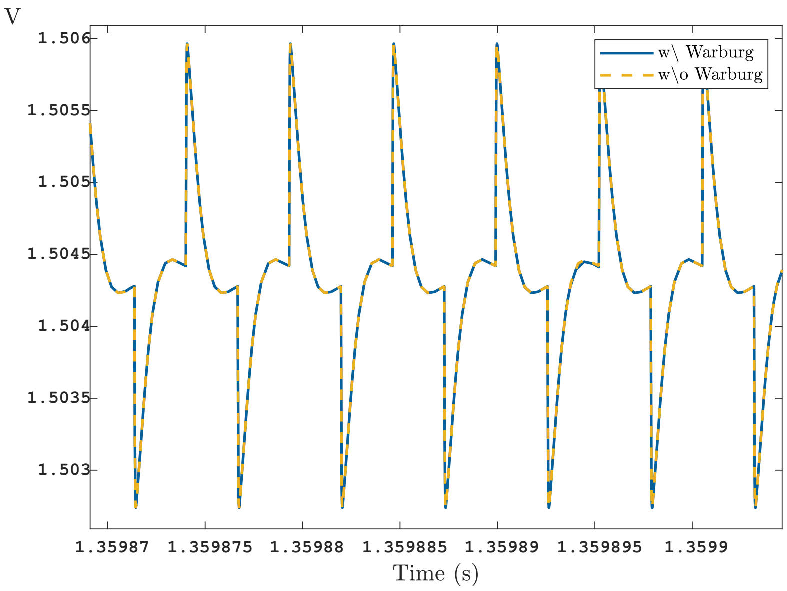

Figure 3.20: Comparison between the time simulations in time with the designed system loaded with the both membrane models with and without the Warburg impedance.

SiC

SNR		**SFDR**		**ENOB**	
w\ Warburg	**w\o Warburg**	**w\ Warburg**	**w\o Warburg**	**w\ Warburg**	**w\o Warburg**
112.80	112.80	67.27	67.32	7.98	7.98

SiO_2

SNR		**SFDR**		**ENOB**	
w\ Warburg	**w\o Warburg**	**w\ Warburg**	**w\o Warburg**	**w\ Warburg**	**w\o Warburg**
110.50	110.34	65.98	66.09	7.98	7.98

Table 3.7: Comparison of the performance parameters between the designed system loaded with the two models with and without the Warburg impedance.

Chapter 4

Firmware and software development

The microcontroller has been programmed through the Code Composer Studio (CCS) platform. A code had already been developed to manage the tension applied to the membrane (with the old system) and included the battery voltage and temperature monitoring. However, it had to be updated for implementing the new functions by introducing new BLE characteristics, the generation of the PWM signal, and the data exchange with the temperature sensor. The modifications, at any rate, are not including the deactivation of the battery level monitoring since it could still be useful; for what concerns the integrated temperature sensor, instead, due to its low resolution (4°C) and even worse accuracy, and also considering the new sensor implementation, it is not going to be kept running. The data of battery voltage are given after receiving a scan request, which means that every time a device scans for advertisement, even without forming a connection, the microcontroller sends a scan response back [99], which contains some information about the device with the last bits reserved for battery voltage data.

4.1 Development setup

The development kit is a printed circuit board containing the microprocessor of interest and the minimal support logic needed to enable the users to prototype applications. In this case, the Development kit that embeds the CC2640R2F microprocessor is used; however, since it includes the microcontroller with a 48-Pin VQFN package, different from the one that will be mounted on the final board, it is then necessary to choose ports with the same role as in the final package. The board already includes the oscillators, the decoupling circuits, and some LEDs and buttons to allow additional testing. The board is fitted with a USB connector and, upon purchase, a USB cable is provided, thus enabling the user to program and supply it through a USB port.

Code Composer Studio is an integrated development environment (IDE) that allows the development and debugging of embedded applications and supports the TI microcontrollers. It was first released in 1999, and in 2015 the supports for SimpleLink CC26xx and CC13xx MCU platforms were added. A software development kit (SDK) is a suite of tools useful for developing and programming the desired platform as they usually include some libraries and basic examples,

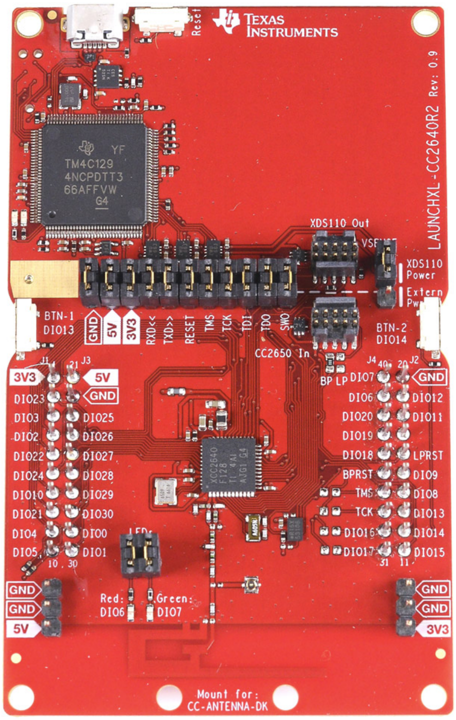

Figure 4.1: LAUNCHXL - CC2640R2 development kit.

promoting simpler and shorter code writing. The CC2640R2F SDK version that is today available is 4.30; however, since the programming has been made on a previously existing code, to maintain continuity, version 3.10 has been used.

4.2 Code structure

In BLE applications, the generic attribute profile (GATT) manages the exchange of data over the connection by organizing them in sections called services that group some characteristics, which, in turn, can include some descriptors. The user can interact with these characteristics, which feature a property (read, write, notify) that determines whether the data contained can be written or read. These are the primary tools needed to manage in order to realize the interaction with the user. Indeed, in this application, 3 characteristics have been used: the first enables the control of the generated voltage, it has a *write* property to allow changing its value; the second characteristic has a *notify* property that has to be activated and gives the temperature information; the third and the last one enables to write how much time must elapse between one temperature measure and the successive, which is a parameter that can be useful to the therapist and for power saving.

4.2.1 BLE management

The pre-existing code provided only the first characteristic, which allowed the insertion of an 8-bit word. It was based on the existing BLE example *simple peripheral*, which is a project that allows the use of 5 characteristics with different properties and sizes. The sample starter project is composed of several codes that manage board features and Bluetooth communication and allow for fluent and easy programming. By organizing it in this way, the user is relieved from in-depth studying all aspects of Bluetooth communication. However, if a particular application is needed, some of these complementary parts should be understood and modified. The code *simple_peripheral_profile.c*, in particular, contains the characteristics' initialization and attribution, so that it has been necessary, firstly, to set it up to include the three desired BLE characteristics with their attributes. The code including the main directives is *simple_peripheral.c* and, by its modification, it is possible to manage the wireless communication, the temporization, and the tasks to bring off. In particular, some of the main properties available for editing are laid out at the top of the code and are defined as constants, whereas some others are set a bit further and have an assigned default value.

When the device sends advertisement packages, it uses a 48-bit address that needs to be decoded by the peer device. It can be public and, thus, constituted by the company ID and company-assigned ID values, or it can be private and include an Identity Resolving Key (IRK) that allows the connection only between two devices that contain this shared information. The latter should be used for privacy preservation. At this point in the device's development, it has been decided to use a public address to make the testing phase smoother. At any rate, it is always possible to change it into a private address in future developments to ensure a safer application. The discoverable mode is set in such a way the peripheral always advertises when supplied, with an advertising interval equal to 2 seconds since it seemed to be the best compromise between energy-saving and ease of connection.

Three main tasks have been created: *simpleperipheral_char1* is called any time a value in the first characteristic is changed and modifies the duty cycle of the PWM signal and, thus, the output voltage. The characteristic is a 16-bit signed number, which can assume an insertable value between -3000 mV and +3000 mV. Based on the output voltage polarity, the analog switch should be driven differently so that IN1 (IOID_8) and IN2 (IOID_9) assume values 1 or 0 depending on whether the written voltage is positive or negative. *simpleperipheral_char2* is called any time the temperature sensor completes a new conversion: it takes the 16-bit temperature data to read from the sensor and sends it via BLE to the read-only characteristic 2. *simpleperipheral_char3* takes place any time a 16-bit word is written at characteristic 3, it changes the clock period and, thus, the time between one temperature measurement and the successive.

4.2.2 PWM signal generation

A PWM signal can be generated from any of the GPIOs. When the desired voltage is inserted as a writing characteristic from a smartphone or any BLE device the board is connected with, the signal's duty cycle is modified proportionally. Since the desired resolution is 8 bit, the signal should have a frequency of about 188 kHz, and this can be set as a constant at the very beginning of *simple_peripheral.c*, with the following lines:

```
//Period and duty in Hz
static uint32_t   pwmPeriod = 187500;
static PWM_Handle pwm1 = NULL;
static PWM_Params params;
```

NULL indicates that the PWM is not active yet. Different PWM signals could be used simultaneously; however, since only one is needed in this application *PWM1* has been configured to be generated at the output of IOID_0. *params* refers to a group of parameters set later on, in the initialization section.

```
PWM_init();

PWM_Params_init (&params);
params.dutyUnits = PWM_DUTY_FRACTION; //The duty cycle is
    expressed as a function of the period
params.dutyValue = 0; //The signal starts with a 0\% duty cycle
params.periodUnits = PWM_PERIOD_HZ; //The period is expressed in
     Hz
params.periodValue = pwmPeriod; //The period is set with the
    value written before

//Opening of the PWM1
pwm1 = PWM_open(Board_PWM1, &params);
if (pwm1 == NULL) {
    // Board_PWM1 did not open
    while (1);
}

PWM_start(pwm1); //The signal is started
```

The parameters indicate the measure units in which the data are inserted and start the PWM with a nil duty cycle. As previously mentioned, the task that manages the modification of the duty cycle is *simpleperipheral_char1* and, every time a new voltage is inserted through characteristic 1, the duty cycle is changed accordingly, as showed in the following lines:

```
int16_t value = ((int16_t)char1val[0] << 8) | char1val[1];
float volt=(float) value;

if (char1val[0] <=0x0F){
    PWM_setDuty(pwm1, (float)((PWM_DUTY_FRACTION_MAX*volt))/3000)
    ;
    PIN_setOutputValue(PinHandle,IOID_8,1);//IN1
    PIN_setOutputValue(PinHandle,IOID_9,0);//IN2
}else{
    PWM_setDuty(pwm1, (float)(-(PWM_DUTY_FRACTION_MAX*volt))
    /3000);
```

```
    PIN_setOutputValue(PinHandle,IOID_8,0);//IN1
    PIN_setOutputValue(PinHandle,IOID_9,1);//IN2
}
```

char1val is the inserted value, which is then converted in a *float* quantity in order to be used for the next calculations. When a voltage is inserted, it is divided by the maximum insertable voltage and multiplied by the 100% duty cycle. If the inserted value is positive or negative, the analog switch should be driven accordingly; therefore the two conditions are divided with an *if function*.

4.2.3 Temperature sensor control

The temperature sensor TMP117 communicates with the microcontroller through the I^2C interface, enabling the mutual data exchange between the master (the microcontroller) and the slave (the sensor). It requires two connection lines; one is used for temporization (SCL) and permits the transmission of data only towards the sensor, whereas the other line (SDA) enables the exchange of data in both directions. In particular, the master can configure the slave from that line and ask it for data, and the information can also flow in the other direction from the slave to the master. The ports in use are the ones preset on the development kit, which have the same properties as IOID_1 and IOID_2 of the final project; nonetheless, any GPIO could be potentially adopted for the scope.

The interface needs firstly to be initialized, by defying the bit rate and opening the I^{2}C feature, as already performed previously for the PWM signal.The bit rate indicates the number of bits per second that the devices can exchange. The TMP117 can work in fast mode with a 400 kHz transfer rate at most and, to reduce the dissipation power and avoid the influence of self-heating, it is recommended to use the highest available communication speed. Then, the TMP117 has been configured sending the configuration data from the master to the slave, through three bytes, the first of which indicates the address of the slave determined by the layout of the sensor's ADD0 Pin, whereas the other ones contain the configuration register settings. In particular, the bit configuration is well explained in TMP117 datasheet as in Figure 4.2. Starting from the upper byte, the first 4 bits are *read* type, and

15	14	13	12	11	10	9	8
HIGH_Alert	LOW_Alert	Data_Ready	EEPROM_Busy	MOD1[(1)]	MOD0[(2)]	CONV2[(2)]	CONV1[(2)]
R-0	R-0	R-0	R-0	R/W-0	R/W-0	R/W-1	R/W-0
7	**6**	**5**	**4**	**3**	**2**	**1**	**0**
CONV0[(2)]	AVG1[(2)]	AVG0[(2)]	T/nA[(2)]	POL[(2)]	DR/Alert[(2)]	Soft_Reset	—
R/W-0	R/W-0	R/W-1	R/W-0	R/W-0	R/W-0	R-0	R-0

Figure 4.2: Configuration registor of the temperature sensor TMP117.

they give information about the exceeding of temperature limits, the termination of conversion of data, or the EEPROM memory state. The following two bits indicate the conversion mode, and, as they are both 1, the One-shot mode is set. With this working mode, a conversion can only be started by the master, and right after it, the device goes on standby, thus allowing energy saving. The last two bits determine the conversion time and, as they are both 0, and, considering 8 averaged conversions, is equal to 125 ms. Averaging successive measurements enables to obtain a more stable temperature reading, neutralizing internal sensor noise. The first bit of the lower byte is still used to set the conversion time, whereas the others are configured so that the temperature value is the result of the average of 8 successive conversions, and the Alert mode is on with the respective PIN active low.

The Alert Pin can trigger an interrupt each time the temperature exceeds some variable limits or each time a new conversion is completed. The latter has been implemented in this application: first a new temperature measurement is started, then, as soon as the conversion is over, an interrupt is triggered, and the temperature data are sent to the connected device through the microcontroller via BLE. To enable this, firstly, every time the measurement time interval is elapsed, the function *startconversion()* takes place: it has no input or output, it just starts a new conversion by configuring the sensor through the SDA. Secondly, when the Alert Pin is activated, the interrupt function reads the value and enables modifying the characteristic, which is notified via BLE. The temperature value is given as input to the *SimplePeripheral_char2* function, which works as follows:

```
 uint8_t char2Data[2]; //Variable containing the measurement
   result

//Conversion of the data to a single 16-bit value
char2Data[0] = (tempData & 0xFF00) >> 8;
char2Data[1] = tempData & 0xFF;

// Update characteristic-2 value so that on connect the
   temperature is still sent to the Central Device
SimpleProfile_SetParameter(SIMPLEPROFILE_CHAR2, 2, char2Data);
```

tempData is the input of the function and contains the temperature data: it is firstly converted from a single 16-bit value to two 8-bit values which can be put as a new value in characteristic 2.

Temporization

The function *startconversion()* takes place each clock cycle. It is defined at 10 minutes by default but it can be changed whenever needed through the third writing characteristic by inserting a 16-bit time interval in seconds.

```
//Variable containing the inserted value of time interval
 uint16_t newperiod = ((uint16_t)char3val[0] << 8) | char3val
   [1];
//Interruption of the clock counting
if (Util_isActive(&clkPeriodic)){
  Util_stopClock(&clkPeriodic);
}
```

```
//Redefinition of the clock period and restarting the clock
Util_rescheduleClock(&clkPeriodic, newperiod*1000);
Util_startClock(&clkPeriodic);
```

char3val is the 2-bit value that has been inserted, and the clock period is changed by defining a new period equal to this quantity. This has been done mainly to minimize power consumption: indeed, when not needed, the device does not measure the temperature, thus spending most of the time in standby such that both power consumption and self-heating are significantly diminished. However, right after an increase in drug release or a change in dosage, a more frequent control may be needed so that the medician or therapist can insert a new time interval in order to verify the changes in time. At this level, it has been decided to avoid using the Alert Pin to overcome precise temperature values since a significant number of variables influence it. Thus, the decision to intervene and how to do it is left to the medician. For example, the interface with which the user approaches could send a message to warn that the temperature is getting off the limits and, consequently, knowing the patient's current state, decide if it is necessary to intervene and how.

Temperature codification

When a new temperature conversion is completed, the Alert Pin triggers the interrupt which reads the value from the 16-bit temperature register of the sensor shown in Figure 4.3.

15	14	13	12	11	10	9	8
T15	T14	T13	T12	T11	T10	T9	T8
R-1	R-0	R-0	R-0	R-0	R-0	R-0	R-0
7	6	5	4	3	2	1	0
T7	T6	T5	T4	T3	T2	T1	T0
R-0	R-0	R-0	R-0	R-0	R-0	R-0	R-0

Figure 4.3: Temperature register of the temperature sensor TMP117

The data are sent to the microcontroller as a 16-bit word assuming only positive values comprised between 0 and $2^{16} = 65536$. From 0 to 32767, the temperature is positive and assumes the maximum value at *0111 1111 1111 1111* (or, in hexadecimal *7FFF*), whereas an output between 32768 and 65536 expresses a negative temperature which is minimal at *1000 0000 0000 0000* (or *8000*). Given that the sensor resolution is $7.8125mC$, the temperature varies in a range between -256°C and a bit less than +256 °C (255.9921 °C). This reading task is fullfilled in few lines, including the require of the converted data from the master to the slave and the subsequent receving of a 16-bit word through the SDA line. When the received value corresponds to a negative temperature, the binary number needs to be converted into a 2's complement value, inverting its bits and then adding 1.

```
//Identification of the sign by evaluating the first bit
if (temperature & 0x8000) {
   //Inversion of all the bits composing the binary value
       temperature ^= 0xFFFF;
   //Adding of the unity for completing of conversion in 2's
   complement
       temperature  = temperature + 1;
}
```

The resulting value is a 16-bit binary number, with a resolution of 7.8125 m°C. Before the user receives them it is needed to go through the conversion in Celsius degrees and this has been performed in the successive step of the communication, through a Graphical User Interface.

4.3 Grafical user interface

An interface has been developed with the MATLAB tool App Designer to enable the user to interact with the device. This software allows easy development of a Graphical User Interface (GUI) through some interactive components such as buttons and switches.

By pushing the *'CONNECT'* button, the computer searches for the device *'nDS2'*, which, when supplied, is always advertising. If the device is not nearby, the status changes in *'DEVICE NOT FOUND'* and it is possible to try again to start a communication. Once connected, the interaction with the device for voltage management is enabled as well as the automatic update of the temperature value detected. When inserting a new voltage value, the most convenient measure unit has to be chosen; then, a value comprised between +3 V and -3 V should be inserted; if these limits are exceeded, an error message informs the user, inviting him to remain in the correct range and the applied tension maintains the previous value. However, since the voltage can assume only discrete values with a resolution of about 11.7 mV, although the user can insert any value with a 1 mV resolution, it is always rounded to the nearest possible output value.

The temperature value is expressed in Celsius degrees, and, thanks to the gauge, it is possible to evaluate at a glance whether the measured temperature is within typical values and decide if the increase (or decrease) of temperature requires a modification in the therapy. Whereas the skin temperature can vary consistently, the core body temperature should remain in a very narrow range between 36°C and 38°C [100]. However, it is essential to understand the circadian rhythm and other internal and external variability sources, as even age, sex, and time of the day, to have a clear idea of what a specific temperature means [101].

The time interval between one temperature conversion and the successive can be inserted, and the choice of the unit of measurement is left to the user. This is mainly useful for energy-saving reasons so that when it is not needed, the sensor can be left on standby, whereas it can work at higher rates when the variations in time need to be evaluated. Also in this case, when the bounds are overgone, an error message alerts the user.

To ensure control overtime of the therapy, each time a new voltage is inserted, the date, the time, and the updated value are recorded in a text file that is always available for consultation when needed.

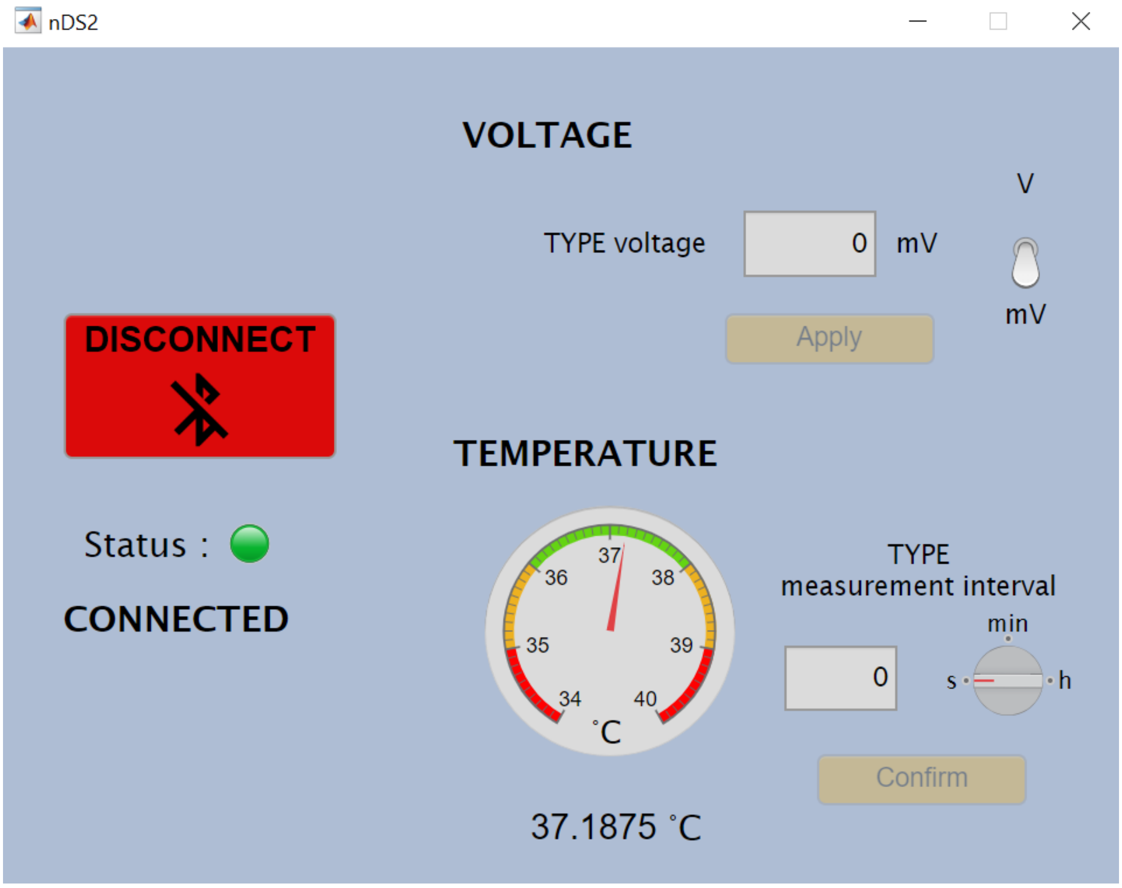

Figure 4.4: Graphic User Interface. The button on the left enables to start or interrupt the connection and the status light, along with the indication immediately below, informs the user of the device connection state. On the top right, there is the field where the desired voltage value to apply can be inserted, the unit measure can be chosen conveniently. The temperature data are displayed both in terms of number and color through the gauge on the bottom right part. The time interval between two successive measurements can be chosen appropriately through the insert data field right beside it.

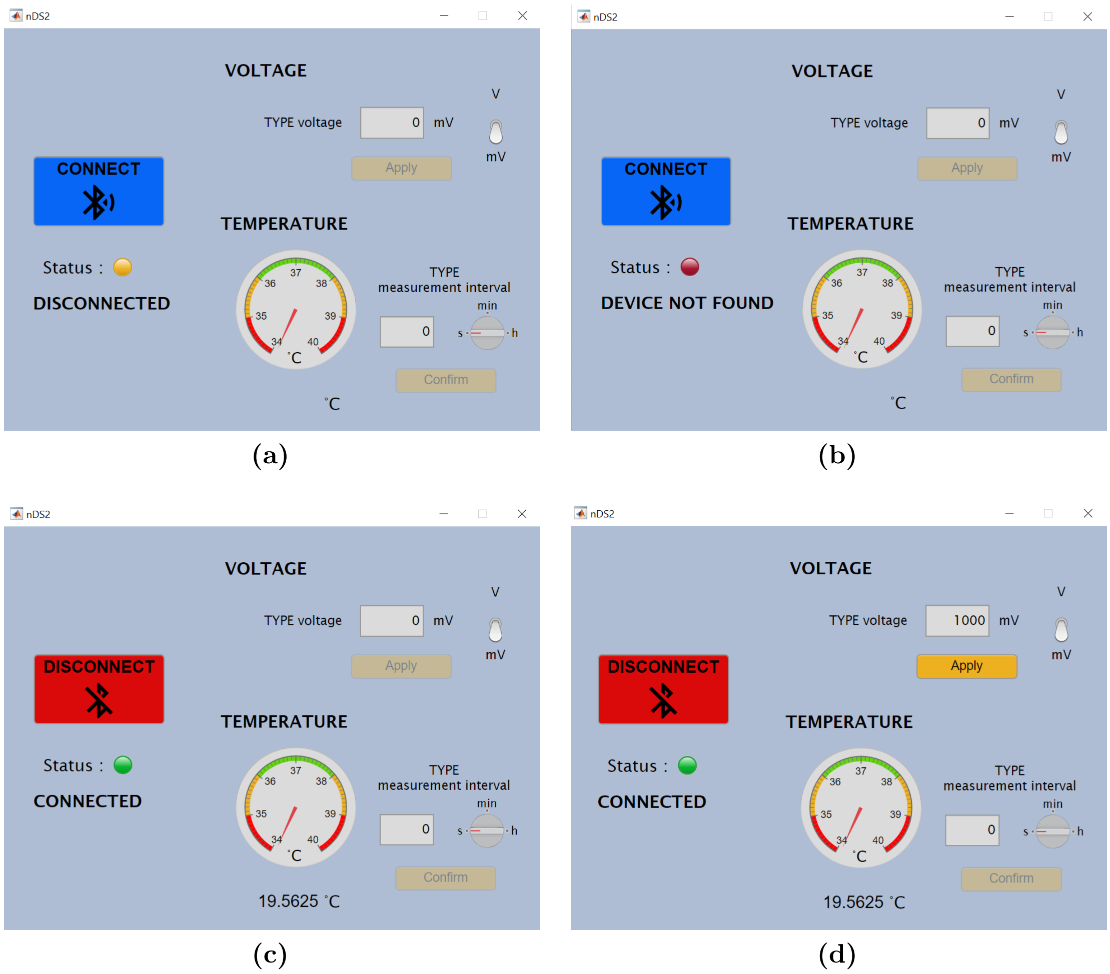

Figure 4.5: These four screenshots show the usage of the interface. a) represents the interface before connecting, pressing the blue button, the interface starts searching for the device. b) shows what the interface looks like when the device has not been found. This can happen because of distance, lacking the power supply, or if the device is engaged in another connection. c) and d) show the display when the connection has been successful, and the two devices are exchanging data. The microcontroller starts to send regularly temperature data to the interface, which, in turn, can send the desired voltage value to apply to the membrane. When the tension data is an acceptable value, the button *"Apply"* becomes available, and the command can be sent.

Chapter 5

Experimental validation

Some experimental tests have been performed by using active and axial passive components mounted on a breadboard. First, the voltage has been generated with the new system and verified, then it has been applied directly to the membrane and, finally, the temperature sensor has been tested.

5.1 Generation of the analog potential

The PWM signal has been generated directly from the microcontroller GPIO DIO_0 and is given as input to the designed Sallen-Key filter. The circuit, including

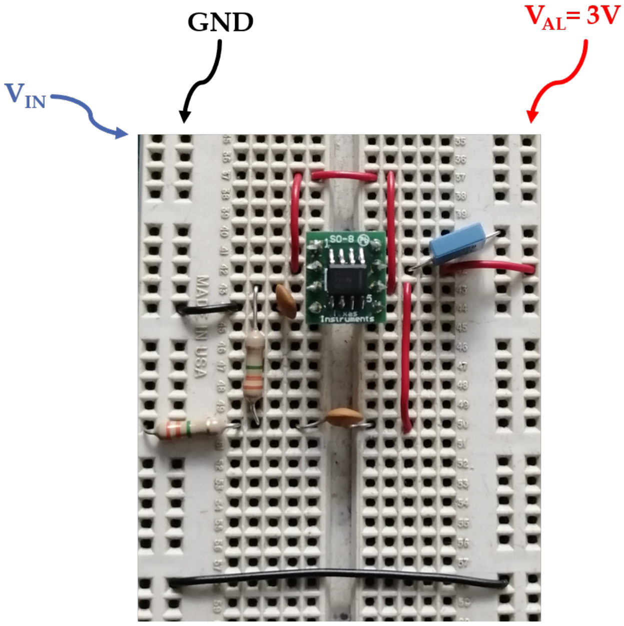

Figure 5.1: Sallen-Key circuit to test of the output analog voltage.

the microcontroller board, has been powered by the generation of a monopolar voltage of 3V from the stabilized power supply, so that the digital output signal from the PWM circuit could actually assume values of 0V or 3V. Using an oscilloscope, both the input and output signals could be measured. First, it has been evaluated

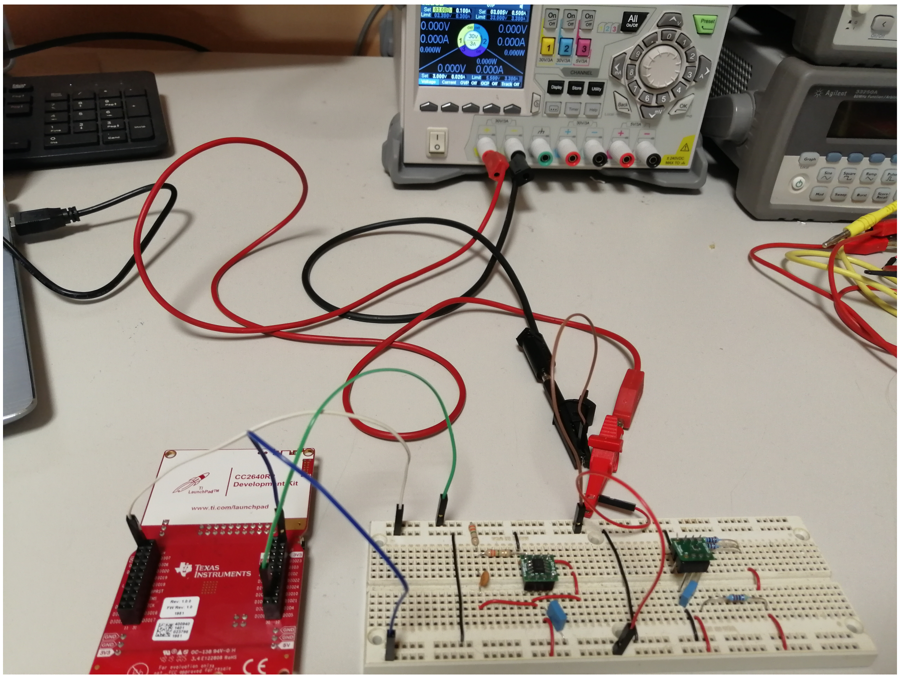

Figure 5.2: Set up of the circuit supplied from the stabilized generator. The launchpad is connected to the board to supply itself and also to provide the input square signal.

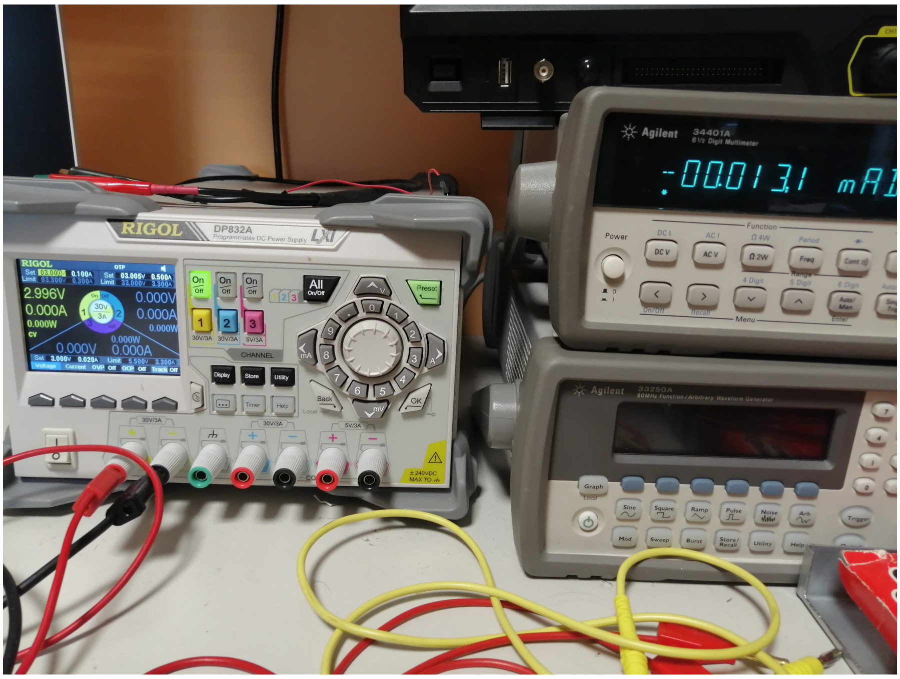

Figure 5.3: Absorbed current at 3V supply voltage from the circuit for the PWM filtration.

how much this part of the final system consumes in terms of power, putting a multimeter in series with the circuit when supplied and excluding the launchpad which could introduce some uncertanties as it is composed also of components which will not be part of the final device. The current absorbed by the circuit at rest is 13.1 μA (see Figure 5.3).

5.1.1 Results

The input digital signal is, as expected, a square wave comprised between 0V and 3V and its duty cycle can be changed by inserting the desired analog output voltage through the interface. The amplitude, in fact, takes 3 divisions, each of which corresponds to a 1 V amplitude as indicated in the lower-left part of the display, whereas each vertical division corresponds to 8 μs, thus, each smaller tick is about 1.6 μs. Observing with care, it can be noticed that in each of the three cases shown in Figures 5.4, 5.5 and 5.6, the period corresponds to a length a bit longer than 3 ticks and, thus, $\simeq 5.3 \mu s$. When the signal goes through the low-pass filter, comes out as a continous analog signal, which assumes, for each duty cycle, the respective fraction of the full-scale. In Figures 5.4, 5.5 and 5.6, the continous voltages are shown, each of them assume a coherent value for the input signal rapresented on the left.

In order to trace the consistency of the circuit output behavior, the resulting analog voltage for various inputs has been taken into account, considering the entire working range. This enabled the evaluation of the converter's transfer curve and further considerations about the DNL. The experimental transfer curve in Figure 5.7 reveals good linearity and matches the theoretical one excellently. The equations of the two lines are reported on the graphs and are:

$$\begin{aligned} \textit{Theoretical: } V_{out}(mV) &= 11.765mV \cdot x(code) \\ \textit{Experimental: } V_{out}(mV) &= 11.766mV \cdot x(code) + 0.7417mV \end{aligned}$$

The two equation do not differ much from each other, and this can also be quantified in terms of *Gain Error* and *Offset Error*:

$$\text{Gain Error} = 0.011\% \qquad\qquad \text{Offset Error} = 0.7417mV \tag{5.1}$$

In Figure 5.1 are reported some values for the differential non-linearity in different points of the range. Although at some steps it gets considerable, it is always much smaller than the least significant bit, thus granting the keeping of monotonicity throughout the range without losing any bit.

Graphs and tables present the output voltage variations as a function of the number of bits and the interpolation of the experimental points of the transfer curve has been performed through the least-square method. However, as it has been previously explained, the value to insert in the interface numeric field can have a precision higher than the designed one, whose resolution instead is $\simeq 11.7mV$. As the latter is not an integer value, the minimum leap required to obtain an output voltage variation is not constant over the range. To overcome this problem, the interface has been programmed to set an output voltage as close as possible to the inserted value. For easier usage of the device, a table that reports the output for each group of values as shown in Table 5.2 could be provided.

Figure 5.4: DC = 16.7 %

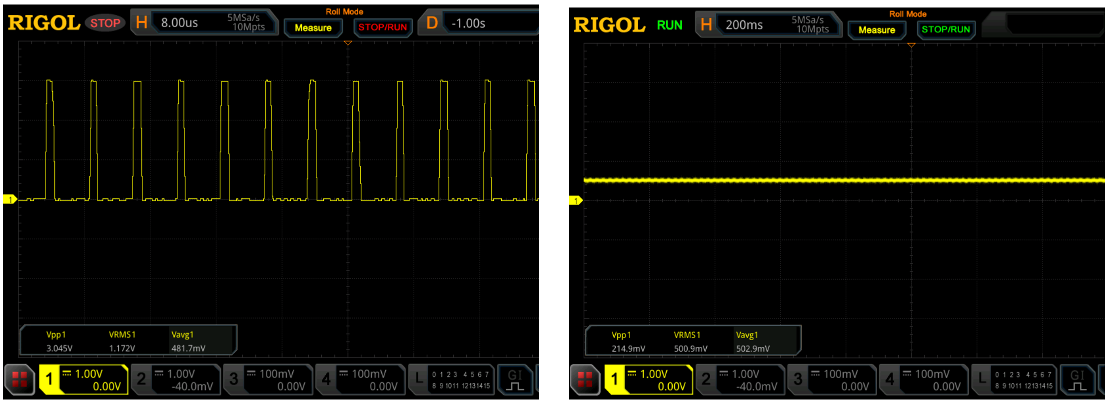

(a) Input signal (b) Output signal

Figure 5.5: DC = 33.3 %

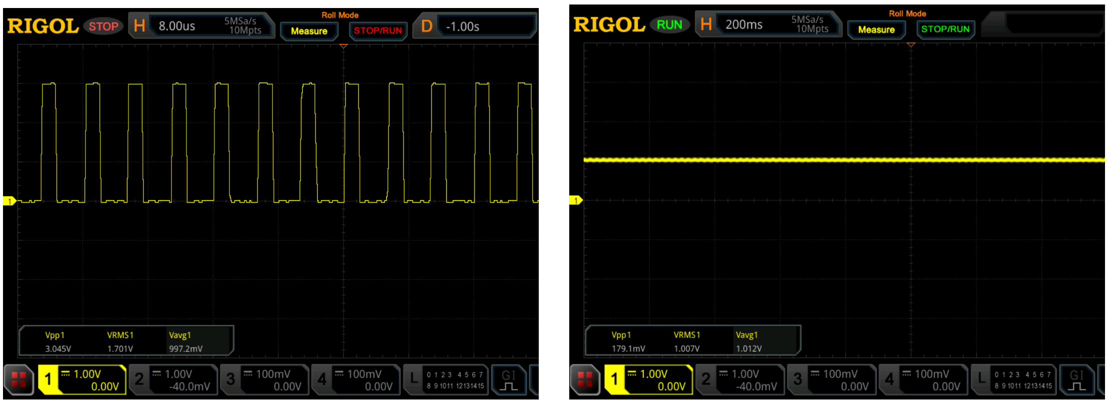

(a) Input signal (b) Output signal

Figure 5.6: DC = 50 %

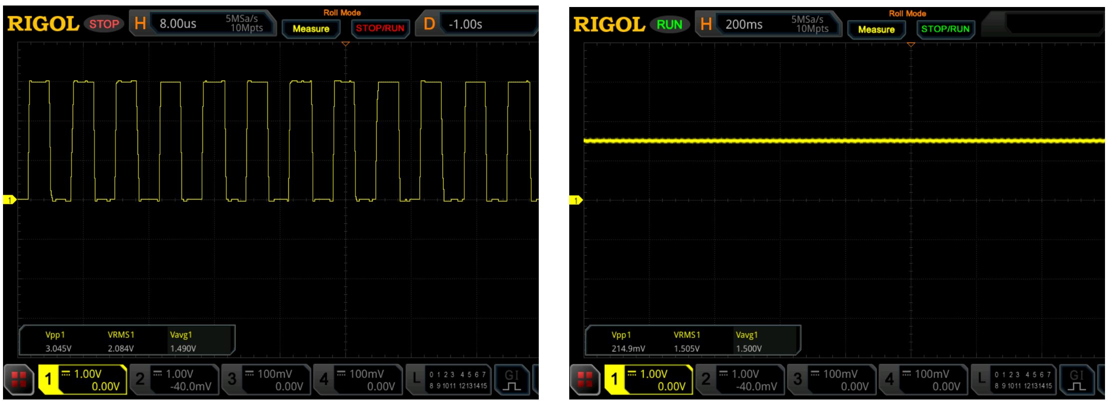

(a) Input signal (b) Output signal

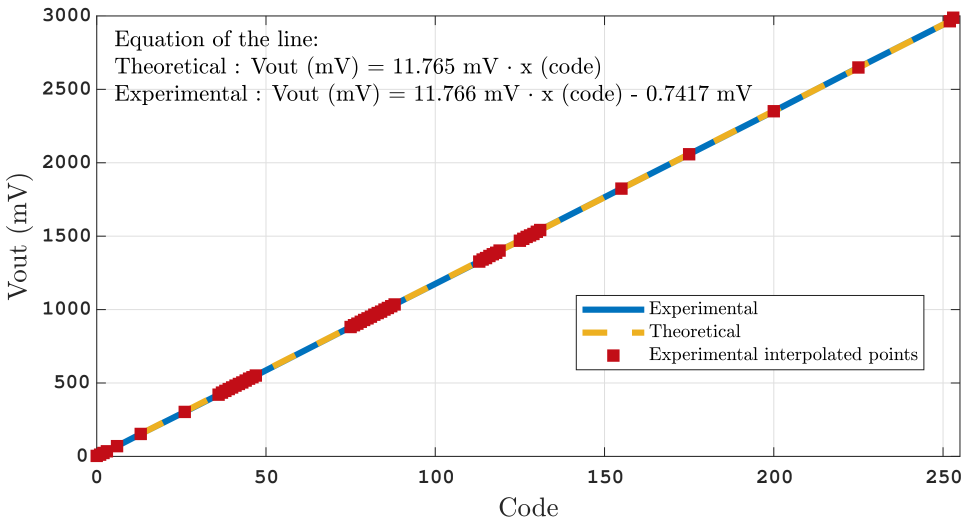

Figure 5.7: Experimental transfer line of the converter.

Code	Vout (mV)	(Vout(i)-Vout(i-1)) mV	DNL (mV)	DNL (LSB)
40	469.7	-	-	-
41	482.2	12.5	0.735	0.063
42	493.4	11.2	-0.565	-0.048
43	503.8	10.4	-1.365	-0.116
44	516.6	12.8	1.035	0.088
45	529.5	12.9	1.135	0.097
46	539.2	9.7	-2.065	-0.176
82	965.2	-	-	-
83	976.3	11.1	-0.665	-0.057
84	986.2	9.9	-1.865	-0.159
85	1000	13.8	2.035	0.173
86	1011	11	-0.765	-0.065
87	1023	12	0.235	0.02
88	1035	12	0.235	0.02
125	1469	-	-	-
126	1482	13	1.235	0.105
127	1495	13	1.235	0.105
128	1505	10	-1.765	-0.15
129	1515	10	-1.765	-0.15
130	1530	15	3.235	0.275
131	1542	12	0.235	-0.02

Table 5.1: Differential non-linearity values obtained experimentally for different regions of the working range. They always assume negligible values, thus preserving from the loss of monotonicity, linearity, or bits.

Inserted value (mV)	Vout (mV)
0-6	0
7-18	11.76
19-30	23.53
31-42	35.29
. . .	
466 - 477	470.59
478 - 489	482.35
490 - 500	494.12
501 - 512	505.88
. . .	
972 - 983	976.47
984 - 994	988.24
995 - 1006	1000
1007 - 1018	1011.76
. . .	
1466 - 1477	1470.59
1478 - 1489	1482.35
1490 - 1500	1494.12
1501 - 1512	1505.88
. . .	
2960 - 2971	2964.71
2972 - 2983	2976.47
2984 - 2994	2988.24
2995 - 3000	3000

Table 5.2: Correspondence between the range of inserted value and the output the user should expect to measure. Depending on the inserted voltage, the output will always be the closest discrete obtainable voltage.

5.2 Electrostatic gating of the membrane

Once the output voltage has been proven to be reliable and easily controllable from the interface, it has been proceeded with the testing of the system directly on the membrane to evaluate whether the dosing control could take place. Therefore, the designed device has been tested on a nanochannel membrane coated with SiC produced by the Houston Methodist Research Institute with the same methodology explained by Di Trani et al. (2020) [13]. The membrane microchannels are organized in a hexagonal pattern and, each of them is connected to thousands of grouped nanochannels, producing a structure of about $6mm \times 6mm \times 411\mu m$. A buried polysilicon electrode runs through the entire surface, and the SiC coating provides biocompatibility.

First, the membrane has been placed in the measuring tool and it has been connected to the designed device through a wire welded to the electrodes. Then, after verifying that everything could work fine, voltage gate values from -3V to +3V with 1V steps have been applied through the dedicated interface.

These tests have been performed by using a custom-made fixture (see Figure 5.9) designed by the research group itself that allows holding the membrane between two reservoirs which can be filled with 2mL of solution free to flow through the channels. The membrane is placed in between two o-rings and the conical reservoirs have Ag/AgCl electrodes inside that work as reference for the externally applied voltage [14].

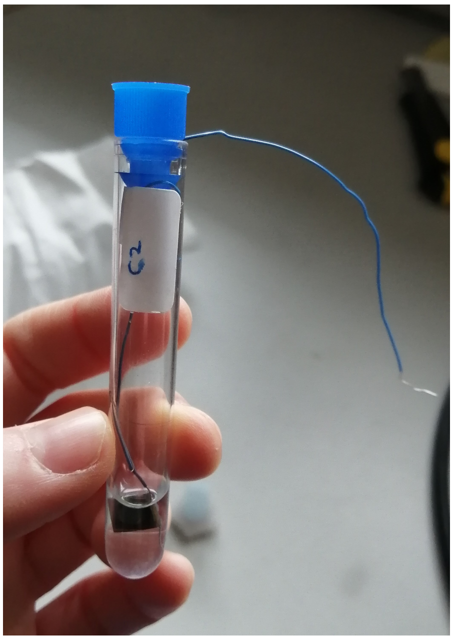

Figure 5.8: Nanochannel membrane used for tests. The squared silicon chip, inside the test tube, is the membrane and the wire that comes out is directly connected to its electrodes, thus allowing for the application of the voltage from the outside. The membrane is suspended in isopropyl alcohol which, due to its low surface tension, creates a first path to the solution through channels and avoids possible channel ruptures.

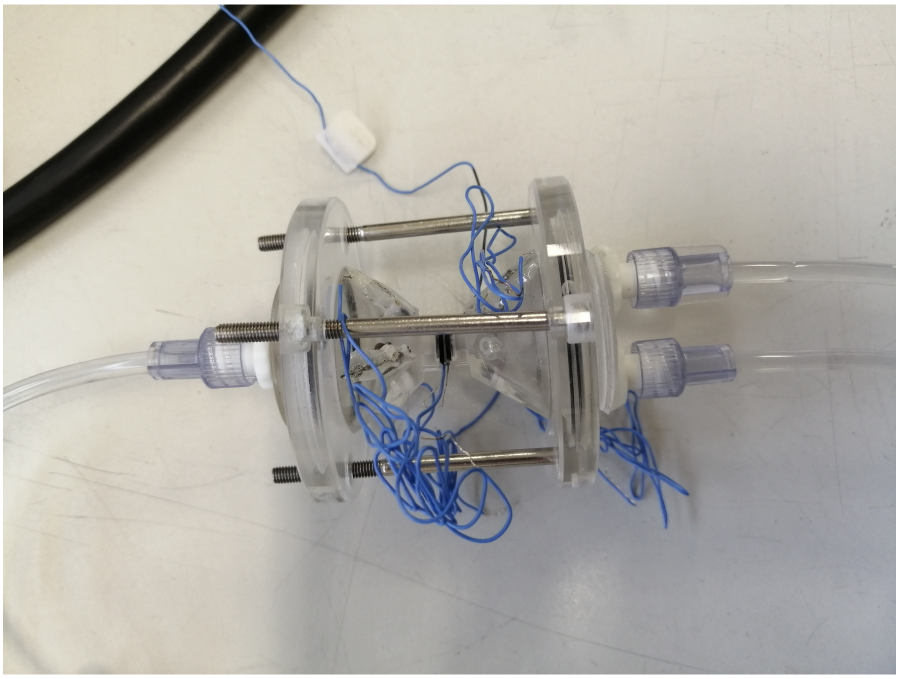

Figure 5.9: Fixture for carrying out the elecrochemical measurements on the membrane. It is composed of two PMMA reservoirs containing Ag/AgCl electrodes with in the middle the membrane holder. The wires coming out from the systems are connected either to the reference electrodes or to the membrane and are available for voltage application.

For these tests, a KCl solution with a concentration of $10^{-4}M$ has been used to fill the reservoirs. A potentiostat (Ivium-n-Stat by Ivium Technologies) has allowed both the application of a transmembrane voltage, which acts as the ion strength of the eventual drug, and the measurement of the transmembrane current. The latter represents the rate of the flowing drugs and changes as a function of the ionic strength; even though in this application ions are used instead of drug molecules, a modulation should be noticed anyway. Therefore, in order to prove the system's functioning, different voltages have been applied between the membrane and the reference electrodes with the designed circuit, aiming at the obtainment of a current intensity modulation measured by the potentiostat. The transmembrane voltage

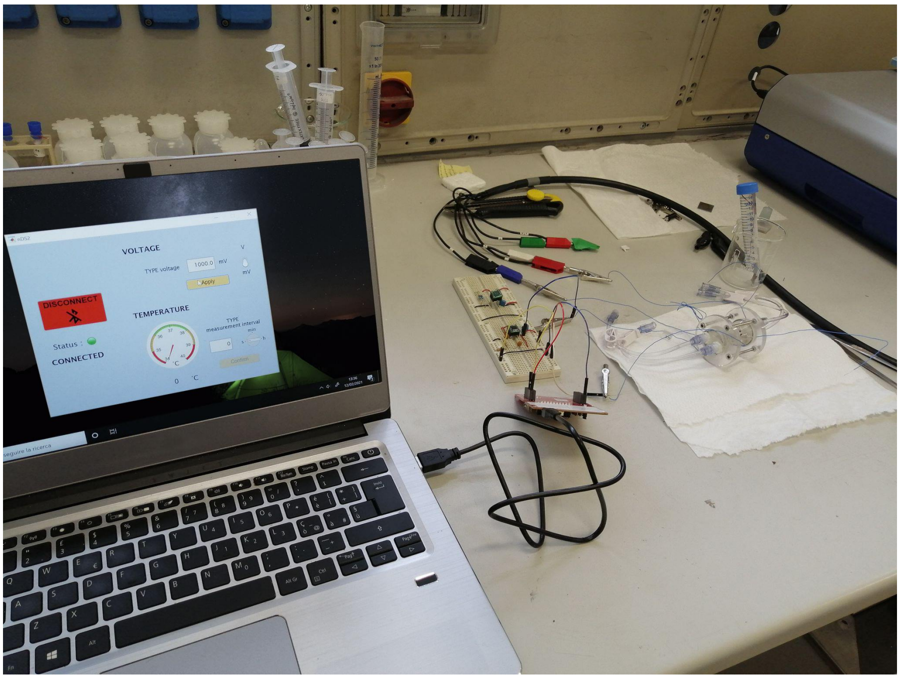

Figure 5.10: The picture shows the experimental set-up. The interface has been used for the voltage modification, the microcontroller and the breadboard are supplied through the PC and the output potential is applied to the membrane thanks to the proper connection wires.

has been applied between -1V and +1V with 0.25V steps, each lasting 30 seconds, during which the current is expected to remain constant. The gate voltage, instead, has been applied through the designed circuit with a magnitude variable between -3V and +3V with 1V steps. To make up for the absence of the analog switch, the terminals have been inverted manually to apply also negative potentials. Through the interface, different voltage values have been inserted and, for each of them, three measurements have been performed to ensure the repeatability of the results.

5.2.1 Results

As expected, for each value of applied gate potential, the resulting current as a function of time is a step wave consisting of 9 steps, each corresponding to a precise value of transmembrane voltage and lasting 30 seconds (as shown in Figure 5.11).

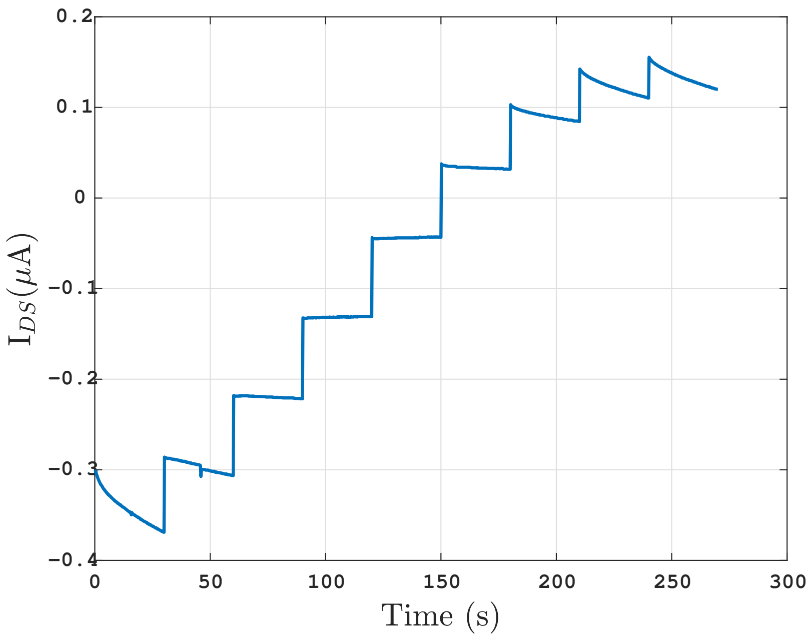

Figure 5.11: Behavior of I_{DS} as a function of time when V_{GS}=0V. The steps corresponds to the different values of transmembrane voltage applied, each lasting 30s.

To trace the final I_{DS}-V_{DS} (transmembrane current as a function of transmembrane voltage) graph, the last value for each step has been considered and, of the 3 successive measurements performed for each V_{GS}, the average value has been calculated. In Figure 5.12, the measurement results are shown and prove a successful modulation. Data have been normalized subtracting the I_{DS} magnitude at V_{DS}=0V to point out the modifications in current related only to the modulating voltage applied (V_{GS}). The current changes with the ionic strength coherently, with the two sides of the graph quite specular with respect to the y-axis. The membrane has a particular behavior at 0V, representing the zero-order release independent from the concentration due to the surface-charges interaction. As soon as a gate voltage is applied, the layer of ions interacting with the channel surface changes, thus leading to a modification in the membrane permeability. More specifically, when a negative voltage is applied, the number of positive ions that adhere to the surface increases, producing a shrink of the channel space free of ions. The same happens for a positive applied voltage, but a higher modification can be noticed in this case. This can be associated with the fact that a SiC membrane presents a negative surface charge at physiological pH, which already produces the attachment of positive ions, limiting the possibility of more interactions. Conversely, with a positive voltage, the measured modification is higher, as the membrane's polarity is inverted.

The change in current may be quantified with respect to the release at 0V, comparing, for instance, the release at V_{DS}=1V (range extreme) for V_{GS}=+3V and V_{GS}=-3V.
The results below confirm a different current behavior at different applied voltages.

$$\frac{I_{DS} \text{ @ } V_{GS}{=}{+}3V}{I_{DS} \text{ @ } V_{GS}{=}0V} = 0.6627 \qquad \frac{I_{DS} \text{ @ } V_{GS}{=}{-}3V}{I_{DS} \text{ @ } V_{GS}{=}0V} = 0.3088 \tag{5.2}$$

At -3V the current decreases of $\frac{1}{3}$, whereas at +3V there is a higher modification of $\frac{2}{3}$.

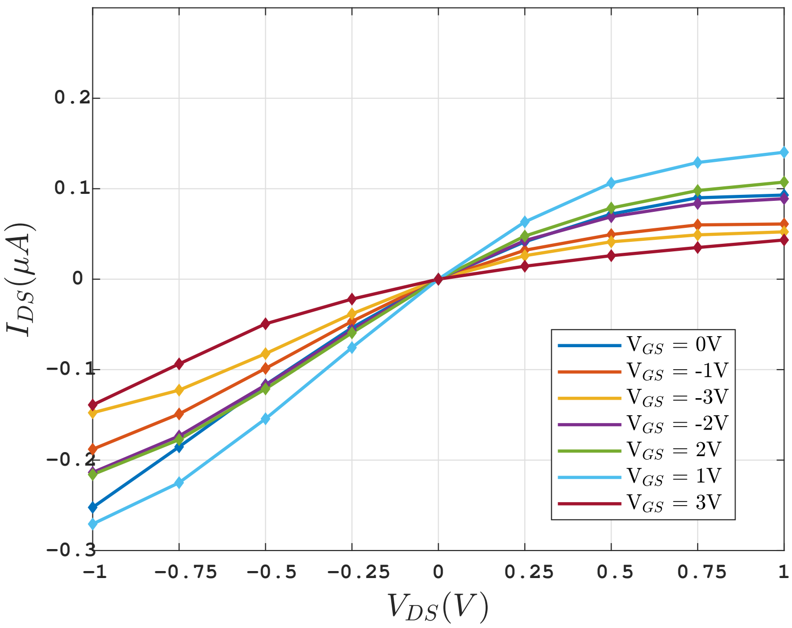

Figure 5.12: Current-Voltage curves for the membrane when different gate voltages are applied with the designed system. The graph show an actual dependency of the transmembrane current on the gate voltage applied.

The results obtained by using the designed system prove the device's effectiveness and show the same magnitude of those performed with the application of the voltages with the potentiostat; however, the response, although coherent, slightly deviates from the reference behavior as shown in Figure 5.13. The reason lies in the fact that the measures have been performed on different days and the membrane condition may vary depending on the nanochannel state and the setting up of the tests. Moreover, the channels are likely to undergo a closing or silicon carbide oxidation.

Although these aspects concerning the membrane, the designed system produced an effective release modulation as different gate voltages entail different ionic behaviors.

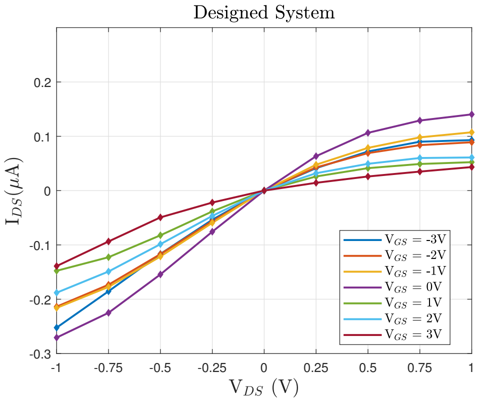

(a)

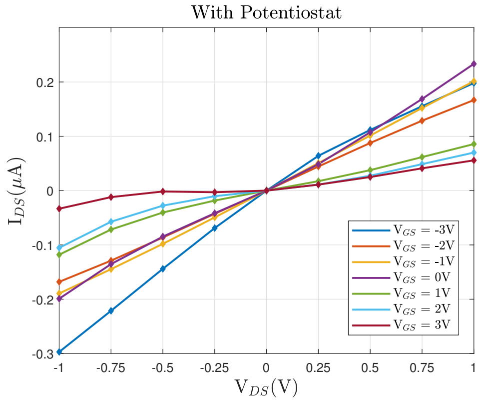

(b)

Figure 5.13: Comparison between the measures performed with the application of gate voltage through the designed system (a) and with the potentiostat (b). The results shows the possibility of obtaining a good modulation with the developed system. The differences in the behaviors are related to the membrane and are not associated with the designed circuit.

5.3 Temperature sensor control

The temperature sensor chosen for this application is the TMP117 by Texas Instruments, of which it has been largely discussed before. However, at this experimental phase, it has been not possible to test it directly, as it is available only in very small packages, which are not practically usable, unless through the printing of a circuit board, but this, unfortunately, has not yet been possible.

In order to test the written firmware and evaluate if, when the sensor will be effectively mounted on the final board, will be drivable efficiently, it has been looked for an assimilable device, as close as possible to the TMP117. Looking among all the possible sensors proposed by Texas Instruments that could be tested with ease and close enough to the reference, the sensor TMP112 has been chosen. It has a temperature measurement range between $-40°C$ and $125°C$ and a variable accuracy along the range: it is equal to $0{,}5°C$ from $0°C$ and $65°C$, whereas it is $1°C$ in a wider range between $-40°C$ and $125°C$. It is not performant as the other since it has lower accuracy and misses some features, such as the averaging of successive measurements for more stable results and an alert pin that could also work as a trigger at the completion of each conversion. However, it was the most effective compromise between dimensions and similarity to the desired device, which enabled the testing of the I^2C communication and the BLE data exchange with few code modifications.

The component has been soldered on an adapter and then mounted on the breadbord along with pull-up resistors and the by-pass capacitors which are of the same value as in the case of the TMP117 sensor. The alert pin has not been used in this case as it is not useful for our purpose, whereas PIN1 and PIN2 of the device that corresponds, respectively, to the SCL and SDA lines, are connected to IOID_4 and IOID_5 of the microcontroller to be driven and enable the communication.

First, as in the case of the other circuit, the current consumption has been

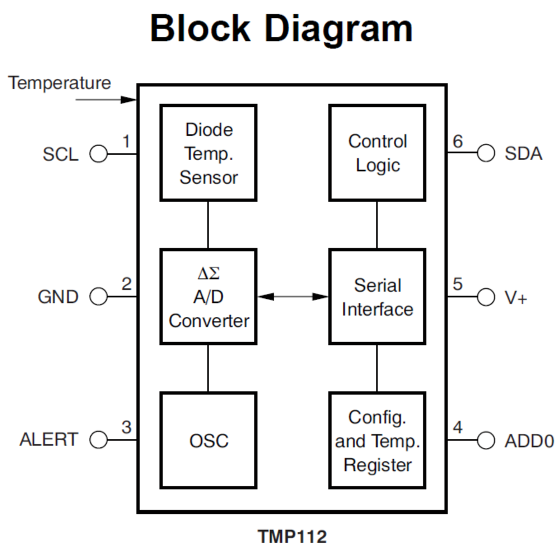

Figure 5.14: Block diagram of the TMP112 temperature sensor by Texas Instruments

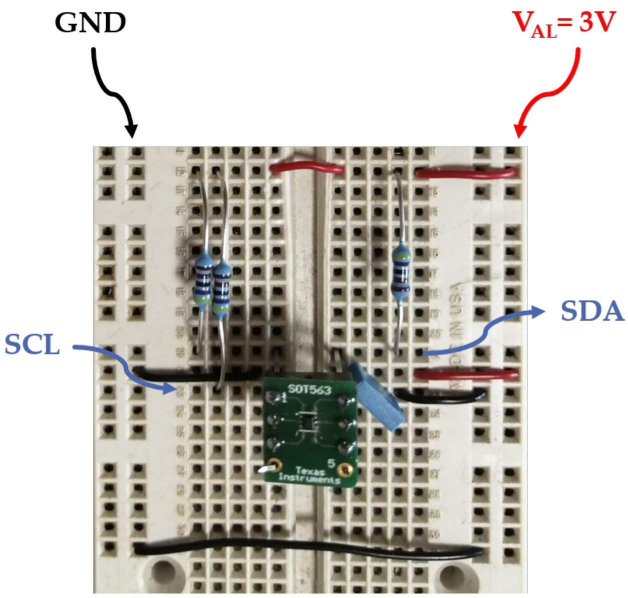

Figure 5.15: Temperature sensor TMP112 along with its pull-up resistors and bypass capacitor.

evaluated. This has been performed with a 3V supply and no connections to the board. Since the used sensor is more consuming, it is presumable that the measured current is higher than the one that will be obtained with the TMP117. In this case, putting the multimiter in series with the circuit, a current equal to 6.5 μA has been measured.

To evaluate if the temperature measurement is accurate, the value displayed on the interface has been compared with the temperature estimated by a thermal imager framing the sensor itself. A thermographic (or infrared) camera creates an image using infrared radiation, therefore wavelengths from about 1 μm to about 14 μm and it is based on the principle according to which the higher is the object

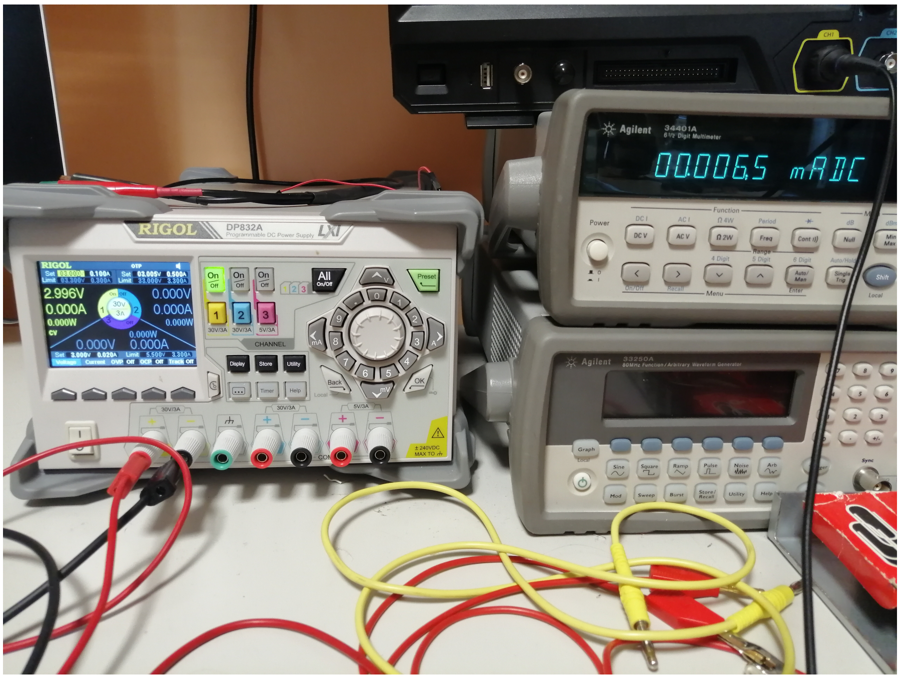

Figure 5.16: Absorbed current at 3V supply voltage by the circuit for the temperature sensor drive.

temperature, the more is the infrared radiation emitted as black-body radiation. The thermal imager used is the Fluke Ti10 Infrared Camera which works in a temperature range between $-20°C$ and 250°C and has an accuracy of ±2°C. It is evident that this device is less performant than the sensor under test, however, it can provide a good reference to ensure if the sensor, the software, and the conversion method from the binary data to the ones in Celsius degrees work finely.

5.3.1 Results

At room temperature, the value detected from the sensor has been compared to a measurement with a common home thermometer. Indeed, the use of the thermographic camera gets unhandy when the temperature of the subject of interest is not distinguishable from the surrounding environment. The room temperature at the moment of the measurement was $20°C$ and this has been confirmed from both the sensor and the thermometer as represented in Figure 5.17.

It was now necessary to make sure that the sensor had a good behavior also at different heat ranges and also that, when exposed to temperature variations, it was able to sense them and return the correct measurements. To bring the sensor to high temperatures mostly alone, avoiding the homogeneity with the surroundings, a jet of hot air has been used and some measurements have been stored during its cooling (see Figure 5.18).

The overall behavior of the system for temperature sensing has shown proper functioning and an effective display of data with a settable update frequency. Further tests may be carried out in a more rigorous way in the future, possibly with the temperature sensor chosen for the final application. For example, within a controlled environment such as an environmental chamber, it would be possible to more accurately assess its behavior. However, at this level, it can be safely affirmed the system has been correctly set.

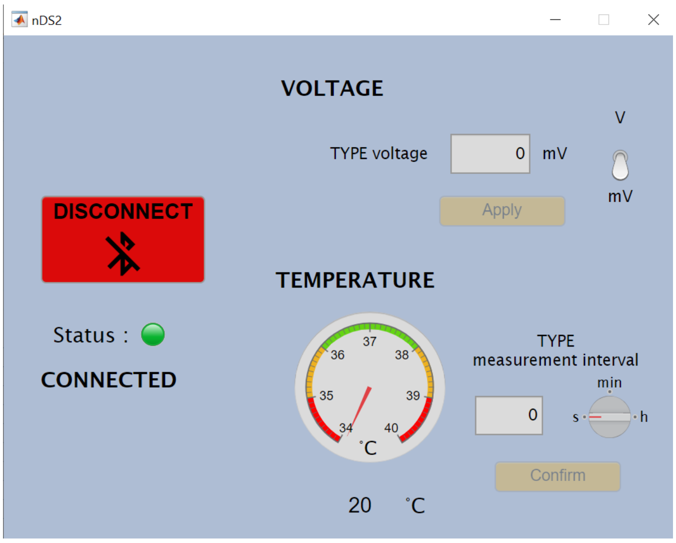

(a) Sensor measurement

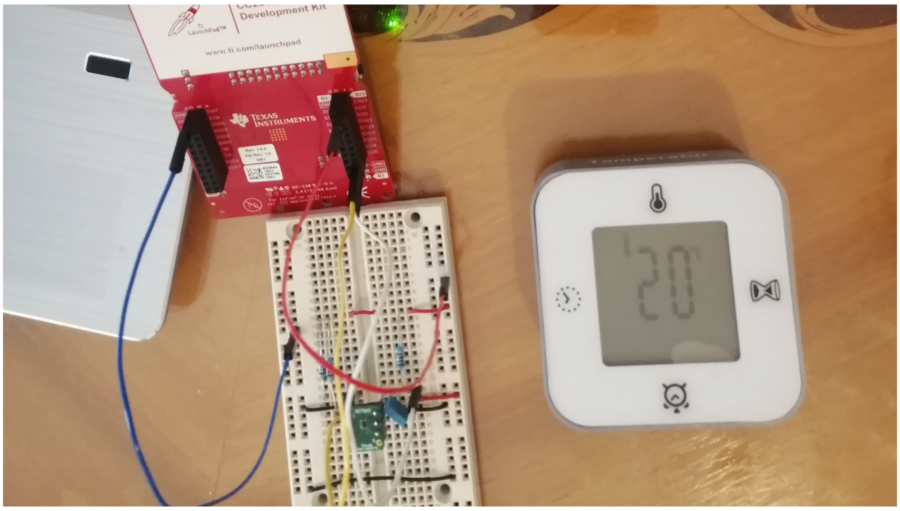

(b) Thermometer measurement

Figure 5.17: Comparison between the room temperature measurements perfromed with a common home thermometer and the sensor. They both measure 20°C, despite the low resolution of the thermometer.

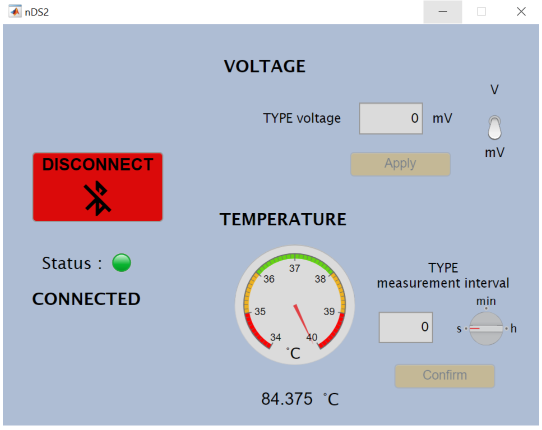

(a) Sensor measurement

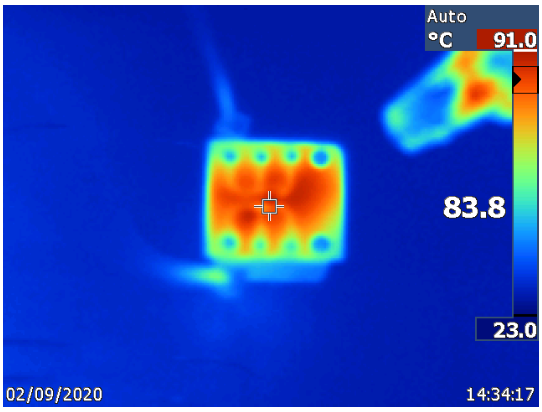

(b) Infrared camera measurement

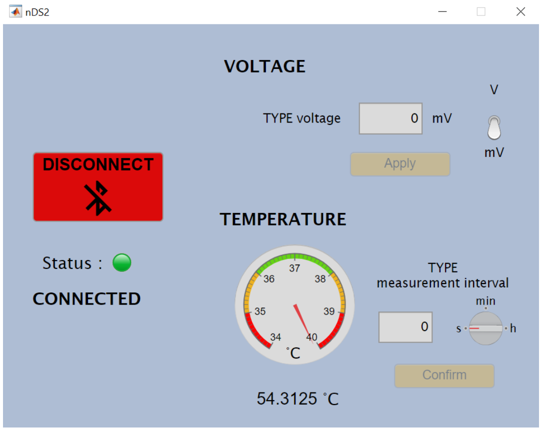

(c) Sensor measurement

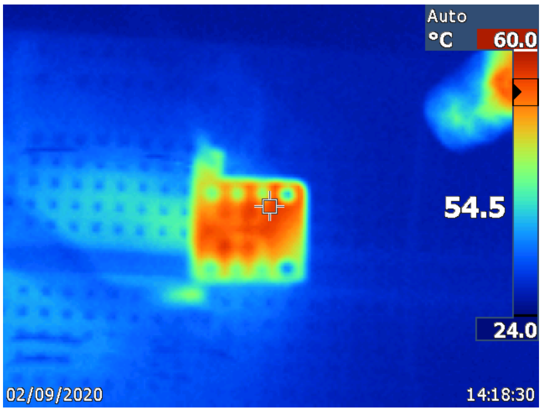

(d) Infrared camera measurement

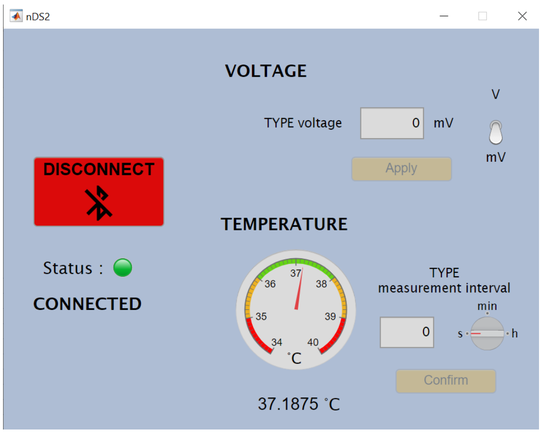

(e) Sensor measurement

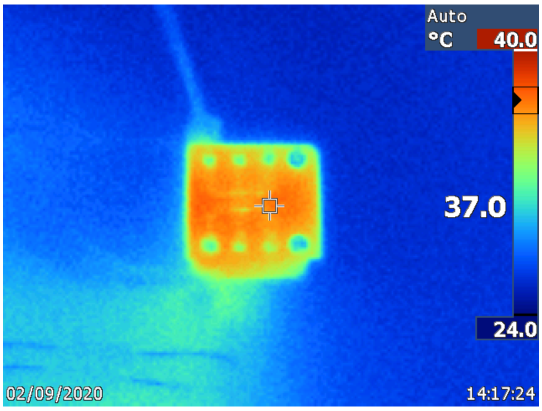

(f) Infrared camera measurement

Figure 5.18: Comparison between the temperatures measured by the sensor and the infrared camera at different heating levels.

Conclusions

A device for remote control of an implantable drug delivery system based on a nanochannel membrane has been designed in this thesis. Starting from a validated device, developed by the Houston Methodist Research Institute and Politecnico di Torino and presented in a paper by Di Trani et al. (2020) [15], the present thesis aim was to overcome this device's limits concerning the resolution of the drug release control and the lack of any feedback from the body core. The designed board, based on a Bluetooth Low Energy microcontroller, has enabled the remote control of the voltage to apply and the temperature monitoring of the implantation region, thus making the medician aware of the patient's health state and able to intervene accordingly. Remote communication has been implemented through Bluetooth Low Energy that is a promising low-power wireless technology already used in many research fields. Finally, a dedicated interface has enabled the user to communicate with the device easily.

First, the system has been designed to implement a PWM-based DAC which made use of the digital signal generated from an output port of the embedded microcontroller and a low-pass filter. Then, its performance has been evaluated through some numerical simulations, which have been performed both in time and frequency. By using data previously measured characterizing the membrane, it has been possible to include its circuit model, too. The converter showed great linearity very close to the theoretical expected result and, with a SiC-coated nanofluidic membrane as load, a SNR (signal-to-noise ratio) $\simeq 112dB$ has been evaluated along with an ENOB (effective number of bits) equal to 7.98, almost coinciding with the 8-bit designed resolution. A comparison between the membrane in-use (SiC-coated) and the reference one (SiO_2-coated) has not revealed any significant difference. The device has then been tested experimentally, demonstrating to work properly in all its parts. The voltage control has proven to be satisfying and accurate, with good linearity in the entire range and a DNL always much smaller than 1 LSB. Therefore, this voltage has been applied to the membrane and, through electrochemical measurements, it has been possible to evaluate whether a modulation of the transmembrane ionic current could be obtained. The measures showed a current noticeable variation with respect to the reference trend (when no voltage is applied), up to $\simeq 66\%$, demonstrating the possibility of modifying the release through the applied potential. A temperature sensor, chosen based on its size and characteristics, has been included in the board and, after setting it up in terms of both hardware and firmware, some experimental tests have been conducted as well, revealing a good behavior in different regions of its operating range and providing the temperature data coherently through the graphical user interface.

The board has been designed in the appropriate software for printed circuits and can now be sent to the PCB assembler to be printed, thus allowing for further testing and verifying the actual functioning of the final device overall. The temperature sensor tested, although very similar, is not the one that will be mounted on the final board. Therefore, further tests on the actual device should be brought off, also with more rigorous methodologies, such as using an environmental chamber. At the present configuration, the temperature is a reference for the medician to make decisions about the release rate modulation. At any rate, the same information could be used in the future to implement a close-feedback-loop that triggers the drug release in response to a change in the local state. For what concerns the small potentials applications to the membrane, as in this thesis 1V voltage steps have been applied, some more trials on a more sensitive membrane than the one used in this thesis work could allow verifying what would happen with a finer modulation.

Although many steps still need to be undertaken to develop the final device, the designed system has proven to enable a more accurate and precise voltage control with respect to the previous board with a much less bulky circuit. Moreover, the tests conducted on the membrane demonstrated the possibility of controlling the dosage finely since the smaller voltage steps entail a wider choice of release rates. Finally, the inclusion of the temperature sensor on the board allows reliable monitoring after implantation, giving additional useful information to the clinician.

Bibliography

[1] *The top 10 causes of death*. https://www.who.int/news-room/fact-sheets/detail/the-top-10-causes-of-death.

[2] Wullianallur Raghupathi and Viju Raghupathi. "An empirical study of chronic diseases in the United States: a visual analytics approach to public health". In: *International journal of environmental research and public health* 15.3 (2018), p. 431.

[3] Mark Lemstra et al. "Primary nonadherence to chronic disease medications: a meta-analysis". In: *Patient preference and adherence* 12 (2018), p. 721.

[4] Fernanda P Pons-Faudoa et al. "Advanced implantable drug delivery technologies: transforming the clinical landscape of therapeutics for chronic diseases". In: *Biomedical microdevices* 21.2 (2019), p. 47.

[5] Dariush Farhud and Zahra Aryan. "Circadian rhythm, lifestyle and health: a narrative review". In: *Iranian journal of public health* 47.8 (2018), p. 1068.

[6] Karim Fifel and Aleksandar Videnovic. "Chronotherapies for Parkinson's disease". In: *Progress in neurobiology* 174 (2019), pp. 16–27.

[7] Gagandeep Kaur et al. "Timing is important in medication administration: a timely review of chronotherapy research". In: *International journal of clinical pharmacy* 35.3 (2013), pp. 344–358.

[8] Alexandria M Palaferri Schieber and Janelle S Ayres. "Thermoregulation as a disease tolerance defense strategy". In: *Pathogens and disease* 74.9 (2016).

[9] Ankur Bhardwaj et al. "Stimuli-sensitive Systems-an emerging delivery system for drugs". In: *Artificial cells, nanomedicine, and biotechnology* 43.5 (2015), pp. 299–310.

[10] Ruslan Dorfman et al. "Application of personalized medicine to chronic disease: a feasibility assessment". In: *Clinical and translational medicine* 2.1 (2013), pp. 1–11.

[11] Giacomo Bruno et al. "Unexpected behaviors in molecular transport through size-controlled nanochannels down to the ultra-nanoscale". In: *Nature Communications* 9 (Apr. 2018). DOI: 10.1038/s41467-018-04133-8.

[12] Alessandro Grattoni et al. "Analysis of a nanochanneled membrane structure through convective gas flow". In: *Journal of Micromechanics and Microengineering* 19.11 (2009), p. 115018.

[13] Nicola Di Trani et al. "Silicon Nanofluidic Membrane for Electrostatic Control of Drugs and Analytes Elution". In: *Pharmaceutics* 12.7 (2020), p. 679.

[14] Nicola Di Trani et al. “Remotely controlled nanofluidic implantable platform for tunable drug delivery”. In: *Lab on a Chip* 19.13 (2019), pp. 2192–2204.

[15] Nicola Di Trani et al. “Electrostatically gated nanofluidic membrane for ultra-low power controlled drug delivery”. In: *Lab on a Chip* 20.9 (2020), pp. 1562–1576.

[16] Ray N Lawson and MS Chughtai. “Breast cancer and body temperature”. In: *Canadian medical association journal* 88.2 (1963), p. 68.

[17] Matthew J Kluger. “Body temperature changes during inflammation: their mediation and nutritional significance”. In: *Proceedings of the Nutrition Society* 48.3 (1989), pp. 337–345.

[18] Perry J Blackshear. “Implantable drug-delivery systems”. In: *Scientific American* 241.6 (1979), pp. 66–73.

[19] Tom N Lea-Henry et al. “Clinical pharmacokinetics in kidney disease: Fundamental principles”. In: *Clinical journal of the American society of nephrology* 13.7 (2018), pp. 1085–1095.

[20] Leslie R Martin et al. “The challenge of patient adherence”. In: *Therapeutics and clinical risk management* 1.3 (2005), p. 189.

[21] Sarah A Stewart et al. “Implantable polymeric drug delivery devices: Classification, manufacture, materials, and clinical applications”. In: *Polymers* 10.12 (2018), p. 1379.

[22] Wan-Wan Yang and Erik Pierstorff. “Reservoir-based polymer drug delivery systems”. In: *Journal of laboratory automation* 17.1 (2012), pp. 50–58.

[23] Simon Herrlich et al. “Osmotic micropumps for drug delivery”. In: *Advanced drug delivery reviews* 64.14 (2012), pp. 1617–1627.

[24] Lothar W Kleiner, Jeremy C Wright, and Yunbing Wang. “Evolution of implantable and insertable drug delivery systems”. In: *Journal of controlled release* 181 (2014), pp. 1–10.

[25] *SynchroMed II Drug Infusion Pump*. https://www.medtronic.com/us-en/healthcare-professionals/products/neurological/intrathecal-baclofen-therapy-systems/synchromed-ii.html.

[26] Nan-Chyuan Tsai and Chung-Yang Sue. “Review of MEMS-based drug delivery and dosing systems”. In: *Sensors and Actuators A: Physical* 134.2 (2007), pp. 555–564.

[27] Brian P Timko et al. “Near-infrared–actuated devices for remotely controlled drug delivery”. In: *Proceedings of the National Academy of Sciences* 111.4 (2014), pp. 1349–1354.

[28] Marco Farina et al. “Remote magnetic switch off microgate for nanofluidic drug delivery implants”. In: *Biomedical Microdevices* 19.2 (2017), p. 42.

[29] Katherine W Ferrara. “Driving delivery vehicles with ultrasound”. In: *Advanced drug delivery reviews* 60.10 (2008), pp. 1097–1102.

[30] D. K. Freeman and S. J. Byrnes. "Optimal Frequency for Wireless Power Transmission Into the Body: Efficiency Versus Received Power". In: *IEEE Transactions on Antennas and Propagation* 67.6 (2019), pp. 4073–4083. DOI: 10.1109/TAP.2019.2905672.

[31] Ada SY Poon, Stephen O'Driscoll, and Teresa H Meng. "Optimal frequency for wireless power transmission into dispersive tissue". In: *IEEE Transactions on Antennas and Propagation* 58.5 (2010), pp. 1739–1750.

[32] Ahsan Noor Khan et al. "Radio frequency controlled wireless drug delivery devices". In: *Applied Physics Reviews* 6.4 (2019), p. 041301.

[33] *Bluetooth*. https://www.bluetooth.com/.

[34] Kang-Ming Chang, Shin-Hong Liu, and Xuan-Han Wu. "A wireless sEMG recording system and its application to muscle fatigue detection". In: *Sensors* 12.1 (2012), pp. 489–499.

[35] Ganjar Alfian et al. "A Personalized Healthcare Monitoring System for Diabetic Patients by Utilizing BLE-Based Sensors and Real-Time Data Processing". In: *Sensors (Basel, Switzerland)* 18 (2018).

[36] Carles Gomez, Joaquim Oller, and Josep Paradells. "Overview and evaluation of bluetooth low energy: An emerging low-power wireless technology". In: *Sensors* 12.9 (2012), pp. 11734–11753.

[37] Zhe-Min Lin et al. "Bluetooth Low Energy (BLE) based blood pressure monitoring system". In: *2014 International Conference on Intelligent Green Building and Smart Grid (IGBSG)*. IEEE. 2014, pp. 1–4.

[38] Mai Ali, Lutfi Albasha, and Hasan Al-Nashash. "A Bluetooth low energy implantable glucose monitoring system". In: *2011 8th European Radar Conference*. IEEE. 2011, pp. 377–380.

[39] Farzad Forouzandeh et al. "A nanoliter resolution implantable micropump for murine inner ear drug delivery". In: *Journal of Controlled Release* 298 (2019), pp. 27–37.

[40] Wouter Sparreboom, Albert van den Berg, and Jan CT Eijkel. "Principles and applications of nanofluidic transport". In: *Nature nanotechnology* 4.11 (2009), pp. 713–720.

[41] Daniel Fine et al. "A robust nanofluidic membrane with tunable zero-order release for implantable dose specific drug delivery". In: *Lab on a Chip* 10.22 (2010), pp. 3074–3083.

[42] Maarten Janssen et al. "Drugs and Polymers for Delivery Systems in OA Joints: Clinical Needs and Opportunities". In: *Polymers* 6 (Mar. 2014), pp. 799–819. DOI: 10.3390/polym6030799.

[43] Alessandro Grattoni et al. "Gated and near-surface diffusion of charged fullerenes in nanochannels". In: *ACS nano* 5.12 (2011), pp. 9382–9391.

[44] Frank Martin et al. "Tailoring width of microfabricated nanochannels to solute size can be used to control diffusion kinetics". In: *Journal of Controlled Release* 102.1 (2005), pp. 123–133.

[45] Jeffrey Toth. "Biocompatibility of Polyaryletheretherketone Polymers". In: Dec. 2012, pp. 81–92. ISBN: 9781437744637. DOI: 10.1016/B978-1-4377-4463-7.10007-7.

[46] GTAKNIMK Petersen. "Bulk micromachining of silicon". In: *Proc. IEEE* 86.8 (1998), pp. 1536–1551.

[47] James M Bustillo, Roger T Howe, and Richard S Muller. "Surface micromachining for microelectromechanical systems". In: *Proceedings of the IEEE* 86.8 (1998), pp. 1552–1574.

[48] *NANOPORTAL TECHNOLOGY*. http://www.nanoprecisionmedical.com/technology/nanoportal-technology.

[49] *NANOPOR*. https://www.delpor.com/technologies/nanopor/.

[50] Sungho Kim et al. "Electrically gated nanoporous membranes for smart molecular flow control". In: *Nanoscale* 10.44 (2018), pp. 20740–20747.

[51] Christos Kostaras et al. "Flow through polydisperse pores in an anodic alumina membrane: A new method to measure the mean pore diameter". In: *Journal of Applied Physics* 124 (Nov. 2018), p. 204307. DOI: 10.1063/1.5050341.

[52] Stuart F Cogan et al. "Plasma-enhanced chemical vapor deposited silicon carbide as an implantable dielectric coating". In: *Journal of Biomedical Materials Research Part A: An Official Journal of The Society for Biomaterials, The Japanese Society for Biomaterials, and The Australian Society for Biomaterials and the Korean Society for Biomaterials* 67.3 (2003), pp. 856–867.

[53] Alexandra Oliveros, Anthony Guiseppi-Elie, and Stephen E Saddow. "Silicon carbide: a versatile material for biosensor applications". In: *Biomedical microdevices* 15.2 (2013), pp. 353–368.

[54] Mauro Ferrari et al. "Silicon nanotechnology for biofiltration and immunoisolated cell xenografts". In: *MRS Online Proceedings Library* 414.1 (1995), pp. 101–106.

[55] Gjermund Kittilsland, Göran Stemme, and Bengt Nordén. "A sub-micron particle filter in silicon". In: *Sensors and Actuators A: Physical* 23.1-3 (1990), pp. 904–907.

[56] Fabio Baldessari. "Electrokinetics in nanochannels: Part I. Electric double layer overlap and channel-to-well equilibrium". In: *Journal of colloid and interface science* 325.2 (2008), pp. 526–538.

[57] Ryuji Hatsuki, Fuchigami Yujiro, and Takatoki Yamamoto. "Direct measurement of electric double layer in a nanochannel by electrical impedance spectroscopy". In: *Microfluidics and nanofluidics* 14.6 (2013), pp. 983–988.

[58] Rohit Karnik et al. "Electrostatic control of ions and molecules in nanofluidic transistors". In: *Nano letters* 5.5 (2005), pp. 943–948.

[59] Qianqian Zhang et al. "Highly efficient gating of electrically actuated nanochannels for pulsatile drug delivery stemming from a reversible wettability switch". In: *Advanced Materials* 30.4 (2018), p. 1703323.

[60] Alexander B Artyukhin et al. “Controlled electrostatic gating of carbon nanotube FET devices”. In: *Nano letters* 6.9 (2006), pp. 2080–2085.

[61] Sven Behrens and David Grier. “The Charge of Glass and Silica Surfaces”. In: *J. Chem. Phys.* 115 (May 2001).

[62] Alessandro Grattoni et al. “Device for rapid and agile measurement of diffusivity in micro-and nanochannels”. In: *Analytical chemistry* 83.8 (2011), pp. 3096–3103.

[63] Reto B Schoch, Harald Van Lintel, and Philippe Renaud. “Effect of the surface charge on ion transport through nanoslits”. In: *Physics of Fluids* 17.10 (2005), p. 100604.

[64] Reto B Schoch, Jongyoon Han, and Philippe Renaud. “Transport phenomena in nanofluidics”. In: *Reviews of modern physics* 80.3 (2008), p. 839.

[65] David C Grahame. “The electrical double layer and the theory of electrocapillarity.” In: *Chemical reviews* 41.3 (1947), pp. 441–501.

[66] Yannis Tsividis and John Milios. “A detailed look at electrical equivalents of uniform electrochemical diffusion using nonuniform resistance–capacitance ladders”. In: *Journal of Electroanalytical Chemistry* 707 (2013), pp. 156–165.

[67] G Barbero and I Lelidis. “Analysis of Warburg’s impedance and its equivalent electric circuits”. In: *Physical Chemistry Chemical Physics* 19.36 (2017), pp. 24934–24944.

[68] Juraj Valsa and Jiri Vlach. “RC models of a constant phase element”. In: *International Journal of Circuit Theory and Applications* 41.1 (2013), pp. 59–67.

[69] *The Data Conversion Handbook,2005*. https://www.analog.com/en/education/education-library/data-conversion-handbook.html.

[70] E Balestrieri and S Rapuano. “DAC consistent terminology: static parameter definitions”. In: *Measurement* 40.5 (2007), pp. 500–508.

[71] *Data converters specifications*. http://ims.unipv.it/Courses/Data_Converters2.pdf.

[72] E. Balestrieri and S. Rapuano. “Defining DAC performance in the frequency domain”. In: *Measurement* 40.5 (2007), pp. 463–472.

[73] *Designing high-performance PWM DACs for field transmitters*. https://www.ti.com/lit/an/slyt795/slyt795.pdf.

[74] Walt Kester. “A Brief History of Data Conversion: A Tale of Nozzles, Relays, Tubes, Transistors, and CMOS”. In: *IEEE Solid-State Circuits Magazine* 7 (June 2015), pp. 16–37. DOI: 10.1109/MSSC.2015.2442371.

[75] Dominik Przyborowski and Marek Idzik. “A 10-bit low-power small-area high-swing CMOS DAC”. In: *Nuclear Science, IEEE Transactions on* 57 (Mar. 2010), pp. 292–299. DOI: 10.1109/TNS.2009.2038054.

[76] Huang Qinjin and Fengqi YU. “A 10-bit 0.41-mW 3-MSps R-I DAC with full-swing output voltage”. In: *IEICE Electronics Express* 15 (May 2018). DOI: 10.1587/elex.15.20180377.

[77] Mamun Bin Ibne Reaz and Md Torikul Islam Badal. “Design of a Low-Power 10-Bit DAC in 130 nm CMOS Technology”. In: Apr. 2019, pp. 762–766. DOI: 10.1109/JEEIT.2019.8717383.

[78] *Digital-to-analog converters to differentiate your design*. https://www.ti.com/data-converters/dac-circuit/overview.html.

[79] *Digital-to-Analog Converters (DACs)*. https://www.maximintegrated.com/en/products/analog/data-converters/digital-to-analog-converters.html.

[80] Eric Gaalaas. “Class D audio amplifiers: What, why, and how”. In: *Analog Dialogue* 40.6 (2006), pp. 1–7.

[81] M. A. Teplechuk, A. Gribben, and C. Amadi. “True Filterless Class-D Audio Amplifier”. In: *IEEE Journal of Solid-State Circuits* 46.12 (2011), pp. 2784–2793. DOI: 10.1109/JSSC.2011.2162913.

[82] Hyoung-Sik Kim et al. “Low cost implementation of filterless class D audio amplifier with constant switching frequency”. In: *IEEE Transactions on Consumer Electronics* 52.4 (2006), pp. 1442–1446.

[83] Tong Ge et al. “A Direct Battery Hookup Filterless Pulsewidth Modulation Class D Amplifier With> 100 dB PSRR for 100 Hz to 1 kHz, 0.005% THD+ N and 16 μV Noise”. In: *IEEE Transactions on Power Electronics* 35.1 (2019), pp. 789–799.

[84] Marco Berkhout. “Balancing Efficiency, EMI, and Application Cost in Class-D Audio Amplifiers”. In: *Low-Power Analog Techniques, Sensors for Mobile Devices, and Energy Efficient Amplifiers*. Springer, 2019, pp. 315–337.

[85] *Reducing the output filter of a Class-D amplifier*. https://www.ti.com/lit/an/slyt198/slyt198.pdf.

[86] *Using PWM Output as a Digital-to-Analog Converter on a TMS320F280x*. https://www.ti.com/lit/an/spraa88a/spraa88a.pdf.

[87] Muhammad Rashid. *Microelectronic circuits: Analysis & design*. Nelson Education, 2010.

[88] Hercules Dimopoulos. *Analog Electronic Filters: Theory, Design and Synthesis*. Jan. 2012. ISBN: 978-9400721890.

[89] *CC2541*. https://www.ti.com/product/CC2541.

[90] *CC2640R2F*. https://www.ti.com/product/CC2640R2F.

[91] *CC13x0, CC26x0 SimpleLink™ Wireless MCU Technical Reference Manual*. https://www.ti.com/lit/ug/swcu117i/swcu117i.pdf?ts=1610786740961.

[92] *LM3670*. https://www.ti.com/product/LM3670.

[93] Bruce Carter and Ron Mancini. “Chapter 16 - Active Filter Design Techniques”. eng. In: *Op Amps for Everyone*. Fifth Edition. Elsevier Inc, 2018, pp. 199–258. ISBN: 0128116471.

[94] Hank Zumbahlen. "CHAPTER 8 - Analog Filters". In: *Linear Circuit Design Handbook*. Ed. by Hank Zumbahlen. Burlington: Newnes, 2008, pp. 581–679. ISBN: 978-0-7506-8703-4. DOI: https://doi.org/10.1016/B978-0-7506-8703-4.00008-0. URL: http://www.sciencedirect.com/science/article/pii/B9780750687034000080.

[95] *TMP117*. https://www.ti.com/product/TMP117.

[96] *MAX31875*. https://www.maximintegrated.com/en/products/interface/sensor-interface/MAX31875.html.

[97] *Screaming Circuits. PCB fabrication*. https://www.screamingcircuits.com/resource-center/services/pcb-fabrication.

[98] Z. Wen et al. "An activated carbon with high capacitance from carbonization of a resorcinol–formaldehyde resin". In: *Electrochemistry Communications - ELECTROCHEM COMMUN* 11 (Mar. 2009), pp. 715–718. DOI: 10.1016/j.elecom.2009.01.015.

[99] *Bluetooth Low Energy Scanning and Advertising*. https://dev.ti.com/tirex/explore/node?node=AKvX4BPHvI6W3ea9a0OTxA__pTTHBmu__LATEST.

[100] James S Hutchison et al. "Hypothermia therapy after traumatic brain injury in children". In: *New England Journal of Medicine* 358.23 (2008), pp. 2447–2456.

[101] Greg Kelly. "Body temperature variability (Part 1): A review of the history of body temperature and its variability due to site selection, biological rhythms, fitness, and aging". In: *Alternative medicine review : a journal of clinical therapeutic* 11 (Jan. 2007), pp. 278–93.

[102] Luis Abelardo Villarruel Mendoza et al. "Recent advances in micro-electro-mechanical devices for controlled drug release applications". In: *Frontiers in Bioengineering and Biotechnology* 8 (2020), p. 827.

[103] Richard V Milani, Robert M Bober, and Carl J Lavie. "The role of technology in chronic disease care". In: *Progress in cardiovascular diseases* 58.6 (2016), pp. 579–583.

[104] Sungho Kim et al. "Electrically gated nanoporous membranes for smart molecular flow control". In: *Nanoscale* 10.44 (2018), pp. 20740–20747.

[105] Christos Kostaras et al. "Flow through polydisperse pores in an anodic alumina membrane: A new method to measure the mean pore diameter". In: *Journal of Applied Physics* 124.20 (2018), p. 204307.

[106] Matsuhiko Nishizawa, Vinod P Menon, and Charles R Martin. "Metal nanotubule membranes with electrochemically switchable ion-transport selectivity". In: *Science* 268.5211 (1995), pp. 700–702.